Status Report:

Uncertainty Quantification of Environmentally Assisted Stress Corrosion Cracking in Used Fuel Canisters

Fuel Cycle Research & Development

Prepared for:
U.S. Department of Energy
Spent Fuel and Waste Science & Technology
C. J. O'Brien, C. Alexander, C. R. Bryan,
E. Schindelholz & R. Dingreville
Sandia National Laboratories
March 28, 2019
M3SF-19N010201047
SAND2019-3600 R

Sandia National Laboratories is a multimission laboratory managed and operated by National Technology and Engineering Solutions of Sandia, LLC., a wholly owned subsidiary of Honeywell International, Inc., for the U.S. Department of Energy's National Nuclear Security Administration under contract DE-NA-0003525.

Sandia National Laboratories

Summary

This study was initiated to quantify and characterize the uncertainty associated with the degradation mechanisms impacting normal dry storage operations for used nuclear fuel (UNF) and normal conditions of transport in support of the Spent Fuel and Waste Science & Technology Campaign (SFWST) and its effectiveness to rank the data needs and parameters of interest. This report describes the technical basis and guidance resulting from the development of software to perform uncertainty quantification (UQ) by developing and describing a holistic model that integrates the various processes controlling Atmospheric Stress Corrosion Cracking (ASCC) in the specific context of Interim Spent Fuel Storage Installations (ISFSIs). These processes include the daily and annual cycles of temperature and humidity associated with the environment, the deposition of chloride-containing aerosol particles, pit formation, pit-to-crack transition, and crack propagation.

Scope: The near-term objectives of the SFWST Campaign's Storage and Transportation (S&T) task within the United States (US) Department of Energy's Office of Nuclear Energy (DOE-NE) are to use a science-based approach to develop the technical bases to support the continued safe and secure storage of UNF, develop technical bases for retrieval of UNF after extended storage, and develop the technical bases for the transport of high burnup fuel after extended periods of dry storage. Prior efforts by SFWST and other organizations (e.g., Nuclear Regulatory Commission [NRC], Nuclear Waste Technical Review Board [NWTRB]) and other countries (including Hungary, Korea, Germany, Japan, Spain and the United Kingdom [UK]) have identified and ranked data needs and modeling needs (also termed "gaps") to complete the technical bases for extended storage. Technical needs were ranked on both their likelihood and the consequence (impact) on licensability and thus safety. Given the large scope, and the large number of high and medium priority data and modeling needs identified for the development of the desired technical bases for the extended storage and transportation of UNF, UQ tools and methodologies are required to provide an informed guidance on the most influential/critical research with the highest payoff (in this case, exemplified by a significantly greater understanding to improve initial or renewal licensing).

Application of UQ methodology to SFWSTC R&D objectives: The application of UQ methodology for its application to degradation mechanisms identified within the SFWST is divided into five tasks originally identified in preliminary report Ref. 1:

1. Identify performance characteristics for specific degradation mechanisms (atmospheric stress corrosion cracking (ASCC) of welded canisters).
2. Link the degradation mechanisms to the regulatory requirements in a mathematical framework: understand performance requirements in a mathematical formulation.

3. Analyze the composition of available data (experimental and numerical): identifying the uncertainties associated with the degradation mechanisms (in this case ASCC) and associated cross-cutting needs.

4. Identify performance characteristics with insufficient data: rank phenomena/input parameters based on performance requirements.

5. Perform preliminary decision making analysis.

Tasks 1–3 address the objective of *developing a methodology to quantify and characterize the uncertainty associated with the degradation mechanisms*. Tasks 4 and 5 deal with the second objective of *demonstrating the effectiveness of this approach to rank the data needs and parameters of interest*. This interim report primarily addresses tasks 1–4. This conceptual UQ methodology supporting analysis of storage and transport of used nuclear fuel provides:

- A way to formally describe that analysis,
- A clear path from formal description to computational implementation to written documentation.

Illustration of the methodology to ASCC: The application of UQ in this study has been demonstrated on a specific degradation mechanism, namely, environmentally- (chloride-) induced stress corrosion cracking (SCC) of welded canisters. This example represents a gap in knowledge, data and models for a phenomenon ranked "very high" for both likelihood and consequence. Although the state of knowledge regarding atmospheric corrosion in general is mature enough to identify the conditions necessary for corrosion (environment, residual stress and material susceptibility), it is not clear if these conditions exist now (or in the future) at specific storage locations. The thermal profile cross-cutting need, whose closure is necessary to provide inputs to SCC analyses was selected to illustrate the necessity of incorporating cross-cutting needs to understand the uncertainty in the inputs they provide to the model. The remaining cross-cutting needs are not considered in this pilot study.

Identification of performance requirements applicable to atmospheric stress corrosion cracking of welded canisters (Task 1): The regulatory requirements for site-specific and general licenses for storage and transportation of UNF pertaining to ASCC are described in Title 10 of the Code of Federal Regulations (10 CFR) Part 72 "Licensing Requirements for the Independent Storage of Spent Nuclear Fuel, High-Level Radioactive Waste, and Reactor-Related Greater than Class C Waste" (10CFR 72.3, 10CFR 72.166, 10CFR 72.236). Additional regulatory guidance can be found and extracted from a series of Spent Fuel Storage and Transportation Interim Staff Guidance (ISG), U.S. Nuclear Regulatory Commission Regulation (NUREG), NUREG/CRs, and industry standards documents (NUREG-1536, ANSI N14.5-1997). In the context of the pilot study, this work focuses on the confinement function.

The above mentioned regulatory requirements (regulatory verbiage) were converted into the quantifiable performance of no through-wall SCC penetration. This metric permits meaningful uncertainty and sensitivity analyses of the ASCC model.

Development of a numerical model for ASCC with inclusion of uncertainty (Task 2): This step corresponds to the selection, development and running of a numerical model representing the degradation mechanism of interest, in this case ASCC. An ASCC model for welded canisters similar to those stored in near-shore and inland environments was constructed leveraging existing corrosion models into a newly developed, integrated, self-contained, software to implement the component models and perform data analysis. The ASCC model describes relevant physical phenomena that collectively describe SCC of welded canisters in marine and inland environments. The analytical output of the study is a probabilistic evaluation of the likelihood (and time in storage) of welded canisters to develop through-wall cracks for a storage system and thermal load similar to systems currently housed at ISFSIs, subsequently identifying areas for more focused attention. The ASCC model evaluates the environmental conditions on the surface of the storage canister as a function of surface location and time, and determines when the environmental conditions at a given location support localized corrosion. Pit initiation and growth lead to SCC crack initiation and growth which are tracked at selected locations until a crack forms or 100 years of storage have occurred. Probability distribution functions describing the various parameters characterizing relevant physical phenomena and corrosive conditions that collectively describe SCC of welded canisters have been extracted from literature data review including both field data, laboratory test data, and numerical analyses. Ambient temperature, relative humidity, pit growth rate, crack growth rate, weld residual stresses and weld location are the physical and geometrical parameters that were considered uncertain.

Probability of the time in storage before the first through-wall crack occurs (Task 3): In order to quantify and rank the importance of the variance of each uncertain input on the variance of the output of interest (probability of through-wall crack occurring during storage), sensitivities analyses were conducted. Using the newly developed probabilistic model, existing ISFSI sites were modeled to predict time to crack penetration of the canister. These results illustrate the capability of the model, but also demonstrate the importance of reducing the uncertainty in certain parameters that result in behaviors not representative of the limited experimental studies that have been conducted. The current regulatory framework supports at least the first 80 years of dry cask storage (including the initial licensing and maximum renewal). It is important to note that 10 CFR 72 does not define confinement as complete isolation; rather it defines site dose limits, so through-wall cracks do not necessarily mean failure to meet the regulations. However, the crack growth (and the size of the crack) are factors in the leak rate and subsequent calculation of dose.

The input parameters having the biggest impact on the time in storage before the first through wall crack occurs were identified as being:

1. Critical Stress Intensity factor for crack formation (K_{th})
2. Atmospheric Salt Concentration (s)
3. Radial weld location
4. Parameterization of chloride particle size distribution $\left(k_\gamma, \theta_\gamma\right)$

with the listed parameters contributing 74% of the variance. These four inputs are identified as areas of interest for additional research to reduce model uncertainty. The sensitivity analysis is dependent on the range of the parameters considered and the initial heat load, which was taken to be the reference case (24 kW).

As an illustration, this model was exercised to predict the life performance of both horizontal and vertical canisters at operating ISFSIs exposed to chloride-containing aerosol particles in both coastal and inland environments. Performance metrics such as time to crack initiation and time to through-wall crack penetration were used to illustrate the capabilities of the present atmospheric model. In addition, a global sensitivity analysis was conducted to identify the processes and input parameters to the model that had greatest impact on these performance metrics. Finally, the analysis was used as a means to identify data gaps and data needs for model parameterization and validation and future improvements to this framework.

> **It is important to note that there is considerable uncertainty associated with the parameters used to calibrate the SCC model, and the implementation in this study was intended to be inclusive. Because of this uncertainty, the quantitative results herein cannot be considered as representative of actual site performance and should not be construed as such. Rather, quantitive results here should provide guidance regarding future research to generate data to make better choices for parameter distributions as an essential part of improving pit and crack initiation and growth predictions along with motivations for necessary experimental measurements and characterization of specific inputs when doable.**

Recommendations (Task 4): The recommendations for future development of uncertainty quantification methodologies to provide guidance on which data, once obtained, will have the greatest impact on meeting the SFWST S&T R&D objectives include:

- Comparison of multiple degradation mechanisms and identification of performance characteristics with insufficient data
    - Perform uncertainty quantification analysis to quantify and characterize the uncertainty associated with several selected degradation mechanisms impacting normal dry storage operations and normal conditions of transport.
    - Degradation mechanisms to consider include: atmospheric stress corrosion cracking (SSC: welded canisters, ranked 2 in SFWSTC gap prioritization report), hydride reorientation and delayed hydride cracking (SSC: cladding, ranked 4).
    - Cross cutting needs considered include: thermal profiles (ranked 1), stress profile (ranked 1) (note the link between the stress intensity factor and residual stress) and drying issues (ranked 3).
    - Ranking the degradation mechanisms and quantifying how much the data uncertainty affects this ranking.
    - Ranking the joint input space common to all degradation mechanisms.
    - Ranking disjoint input spaces specific to each degradation mechanism.
- Improvement of uncertainty characterization and sampling strategies:
    - Inclusion of the appropriate separation of aleatory and epistemic uncertainty. Separation of the uncertainties will enable distinguishing between the likelihood of failure (i.e., aleatory uncertainty) and the confidence of failure (i.e., epistemic uncertainty).

  - Importance sampling or other reliability methods need to be considered.

- Improvement of the atmospheric chloride induced stress corrosion cracking model of welded used fuel storage canisters in marine locations:
  - Inclusion of pre-existing manufacturing defects should be considered.
  - Improvement of the functional form representing the weld residual profile through the thickness of the canister wall.
  - Modification of the pit initiation and pit growth model and their dependence on the aqueous environment.
  - Inclusion of chloride dependence of the crack growth rate equation.
  - Integration of alternative conceptual model such as intergranular SCC of sensitized stainless steel using a model based on percolation theory.
  - Integration of a crack coalescence model.
  - Expansion of material properties beyond 304 stainless steel.

Contents

List of Figures

List of Tables

Acronyms & Symbols

Acronyms

ASCC	Atmospheric Stress-corrosion Cracking
CDF	Cumulative Distribution Function
CFD	Computational Fluid Dynamics
DD	Deposition Density
DHD	Deep Hold Drilling
DOE	U.S. Department of Energy
EPA	U.S. Environmental Protection Agency
CASTNET	Clean Air Status and Trends Network
GSA	Global Sensitivity Analysis
HAZ	Heat-Affected Zone
ISFSI	Interim Spent Fuel Storage Installation
ICHD	Incremental Center Hole Drilling
LHC	Latin Hypercube
MC	Monte Carlo
NE	Nuclear Energy
NRC	U.S. Nuclear Regulatory Commission
NWTRB	Nuclear Waste Technical Review Board
PSD	Particle Size Distribution
PWR	Pressurized Water Reactor
RH	Relative Humidity
S&T	Storage & Transportation
SARP	Safety Analysis Review for Packaging
SCC	Stress-corrosion Cracking
SNL	Sandia National Laboratories
SFWST	Spent Fuel and Waste Science & Technology
UNF	Used Nuclear Fuel
UQ	Uncertainty Quantification
UK	United Kingdom
WC	Weld Centerline
WRS	Weld Residual Stress

Symbols

Constants & mathematical symbols:

$F\,[\mathrm{C/mol}]$ – Faraday constant
$\mathrm{R}\,[\mathrm{J/mol/K}]$ – ideal gas constant
$\mathscr{C}$ – Constant value
$\mathscr{N}$ – normal distribution
N, M, Q – CDF of normal distribution
$\ln\mathscr{N}$ – lognormal distribution
R – CDF of lognormal distribution
$\mathscr{U}$ – uniform distribution
p – a random number where $(0 \leq p \leq 1)$
$F^{-1}(p)$ – Probit function of p with distribution F
$\mathbb{E}$ – expectation value

Environment model:

$T_{\mathrm{max}}\,[^{\circ}\mathrm{C}]$ – maximum temperature
$T_{\mathrm{min}}\,[^{\circ}\mathrm{C}]$ – minimum temperature
$T_{\mathrm{ref}}\,[^{\circ}\mathrm{C}]$ – maximum reference temperature
$(T_{\mathrm{dew}})_{\mathrm{max}}\,[^{\circ}\mathrm{C}]$ – maximum dewpoint
$(T_{\mathrm{dew}})_{\mathrm{max}}\,[^{\circ}\mathrm{C}]$ – minimum dewpoint
a_1 – maximum temperature temperature-scale
b_1 – maximum temperature temperature-shift
c_1 – maximum temperature time-scale
d_1 – maximum temperature time-shift
a_2 – maximum temperature standard deviation temperature-scale
b_2 – maximum temperature standard deviation temperature-shift
c_2 – maximum temperature standard deviation time-scale
d_2 – maximum temperature standard deviation time-shift
μ_1 – minimum temperature shift
σ_1 – minimum temperature standard deviation
μ_2 – maximum dew-point shift
σ_2 – maximum dew-point standard deviation
μ_3 – minimum dew-point shift from max dew-point
σ_3 – minimum dew-point standard deviation

Canister model:

Weld #1 Radial Loc. – radial Location of Weld #1
Weld #2 Radial Loc. – radial Location of Weld #2
$t\,[\mathrm{m}]$ – canister wall thickness

Deposition Model Parameters:

$T_{\mathrm{env}}\,[^\circ\mathrm{C}]$ – environmental ambient temperature
$\Delta t\,[\mathrm{s}]$ – timestep for deposition model (not weather model)
$u_d\,[\mathrm{m/s}]$ – deposition velocity of particles onto the cansiter wall
Re – Reynold’s number
$\tau_w\,[\mathrm{MPa}]$ – shear stress at the canister wall
C_f – coefficient of friction at canister/pipe wall
$u^\star\,[\mathrm{m/s}]$ – friction velocity
$d_{\mathrm{min}}\,[\mu\mathrm{m}]$ – minimum aerosol particle size
$d_{\mathrm{max}}\,[\mu\mathrm{m}]$ – maximum aerosol particle size
$D\,[\mathrm{m}]$ – diameter of the pipe/canister
$D_{\mathrm{B}}\,[\mathrm{m}^2/\mathrm{s}]$ – coefficient of Brownian diffusion
$\varepsilon_p\,[\mathrm{m}^2/\mathrm{s}]$ – coefficient of turbulent particle diffusion
i – surface orientation factor for deposition
$V_t\,[\mathrm{m/s}]$ – turbophoresis velocity
$d\,[\mu\mathrm{m}]$ – particle diameter
c – particle number density
$C_{\%\mathrm{mass}}$ – particle mass density ratio
$C\,[\mathrm{kg/m}^3]$ – particle mass density
$C_\infty\,[\mathrm{kg/m}^2]$ – particle concentration far from the wall density
N_{bins} – number of bins for aerosol particle size histogram
$\rho_{\mathrm{salt}}\,[\mathrm{kg/m}^3]$ – density of atmospheric salt particle
$j\,[\mathrm{kg/m}^2/\mathrm{s}]$ – particle-flux
$s\,[\mu\mathrm{g/m}^3]$ – atmospheric concentration of chloride-containing particles
c_γ – magnitude scaling factor for particle size gamma distribution
k_γ – shape parameter for particle size gamma distribution
$\theta_\gamma\,[\mu\mathrm{m}]$ – scale parameter for particle size gamma distribution
$U_\infty\,[\mathrm{m/s}]$ – wind speed far from the pipe/canister wall
$u_s\,[\mathrm{m/s}]$ – gravitational sedimentation velocity
$\rho\,[\mathrm{kg/m}^3]$ – density of dry air
$\mathrm{DD}\,[\mathrm{g/m}^2/\mathrm{yr}]$ – areal deposition density chloride on canister surface
$m_t\,[\mathrm{kg/m}^2]$ – areal deposition density chloride on canister surface at time t

Maximum pit depth model:

WRS – acronym for Weld Residual Stress
σ_{WRS} [MPa] – weld residual stress
E_{rp} [V_{SCE}] – repassivation potential
$(E_{\mathrm{rp}})_{\mathrm{ref}}$ [A/m^2] – reference repassivation current
$(E_{\mathrm{rp}})_{\mathrm{ref}}$ [V$_{\mathrm{SCE}}$] – reference repassivation potential
b [V/decade] – Tafel slope
WL [m] – Thickness of electrolyte (salt brine) layer
E_{L} [V] – corrosion potential
κ [Ω/m] – conductivity of brine solution
R$_{\mathrm{th}}$ [%] – minimum relative humidity required to cause pit growth
Galvele [A/m] – pit stability product
i [A/m^2] – equilibrium cathode current density
r_{a} [μm] – pit depth (radius of anode)
r_{eq} [μm] – equilibrium pit depth (radius of anode)
i_c [A/m^2] – cathodic polarization
i_p [A/m^2] – passive current density
t_{brine} [μm] – thickness of brine layer

Repassivation potential model:

T_{ref} [°C] – reference temperature for free energy calculations
a^{bulk} – thermodynamic activity in bulk solution
$\Delta g^{\neq}$ (T_{ref}) [kJ/mol] – free energy of adsorption/dissolution
$\Delta h^{\neq}$ [kJ/mol] – enthalpy of adsorption/dissolution
$\theta_{I,j}$ & $\theta_{A,j}$ – adsorption isotherm for species j
n – reaction order parameter
ζ – electrochemical charge transfer coefficient
ΔG_{ads} [kJ/mol] – free energy of adsorption

Crack initiation & growth model parameters:

σ_Y [MPa] – yield stress
K [MPa/$\sqrt{\mathrm{m}}$] – stress intensity factor for mode I fracture
K_{th} [MPa/$\sqrt{\mathrm{m}}$] – threshold stress intensity factor for mode I fracture
Y – geometry factor used in stress intensity factor
T_{cg} [°C] – reference temperature for crack growth
α – crack growth rate at T_{cg}
β – stress intensity exponent

$\alpha - \beta$ correlation	– empirical correlation coefficient between α and β
$\dot{x}_{80^\circ\mathrm{C}}$ [m/s]	– crack growth rate at 80°C
Q_r [J]	– activation energy for crack growth

this page is intentionally left blank

1 Introduction

Atmospheric stress corrosion cracking (ASCC) is a critically important consideration when estimating the lifetime of engineered structures operating in corrosive environments. For example, chloride-induced ASCC of welded zones is a well-documented mode of attack for austenitic stainless steels (including 304SS and 316SS) in marine environments [23]. For atmospheric stress corrosion cracking to occur, three conditions need to be met simultaneously: (i) a susceptible material, e.g., 301, 304, and 316 steels, although –L grade steels have less susceptibility; (ii) tensile stresses, either due to exerted loading or as residual stresses as observed in welds and heat affected zones; and (iii) a corrosive environment including: the chemical environment on the metal surface of an engineered structure, surface temperature and relative humidity; all of which are influenced by the geographic location and the engineering system considered.

The majority of the current approaches for modeling atmospheric stress corrosion cracking are based on continuum models [3, 13, 24–26] integrating together the three conditions listed above with various degrees of description and accuracy. The combined complexities of both the environment and the degradation processes occurring during atmospheric stress corrosion cracking present significant modeling challenges. These include: (i) the development and integration of submodels describing each process in a computationally efficient manner with the appropriate level of accuracy; (ii) gaps in the experimental characterization of corrosion processes, particularly extrapolating from laboratory settings to field settings; (iii) the subsequent validation of each submodel for the intended use of the overall atmospheric stress corrosion cracking model; and (iv) the improvement of the reliability and predictability of such integrated models to assess the structural integrity of components subjected to atmospheric stress corrosion cracking. In order to overcome some of these challenges and to accurately predict the performance of susceptible components, any comprehensive computational model aiming at simulating the processes involved in ASCC must consider and integrate several modeling components in the design of such framework.

First, recognizing that a precondition for atmospheric stress corrosion cracking is the presence of corrosive species and moisture to initiate surface localized pitting (e.g., from dust and aerosols), an atmospheric stress corrosion cracking modeling framework needs to have the ability to describe such an environment. Thus, an environmental submodel needs to account for the geographic location and the associated representation of its environment in terms of dust and aerosol sources, composition and concentration of the salts, and temperature and humidity variations, to name a few. The geographic location naturally impacts the composition and form of the corrosive species, with coastal sites containing higher amounts of chloride-bearing sea-salts [27], while inland sites are generally more impacted by local soil and geology; containing higher levels of silicate, aluminosilicate, carbonate materials, ammonium, sulfate, and nitrates. Road salts and power plant emissions are another significant source of salts but are not expected to be significant beyond several hundred meters from the source [17]. The effect of features such as vegetation, pavement, and buildings has sometimes been considered, for example using Computational Fluid Dynamics (CFD) techniques for modeling the deposition of salts [13], but are typically ignored altogether when modeling the evolution of the environment in an atmospheric stress corrosion cracking model. For instance, a detailed model [3] exists for the generation and deposition of salts but is limited in applicability as factors such as coastal geography and regional climate cycles need to be carefully included in the parameterization. In addition to salt sources, conditions for the deposition of salts onto surfaces of susceptible materials are also important factors to consider in the development of the environmental model. Indeed, deposition conditions are strongly influenced by the geometry and orientation of the structure considered with respect to airflow [6, 10–12, 28–31], but also by turbulence and local conditions near the surface of the attacked material [13]. For example, the analytical deposition model of Piskunov [10] yields a deposition velocity that is directly proportional to the local environment in terms of friction velocity near the surface, which is closely related to the turbulent kinetic energy and deposition conditions.

Second, an ASCC model for passive metals needs to capture the process of localized pitting corrosion ranging from pit initiation by attacking the passive oxide film formed on the surface of the susceptible metal, to the formation of metastable pits, to the transition to stable pits and their subsequent growth, to the eventual stoppage of pit growth through the process of repassivation. It is agreed that corrosion pits propagate as a result of the development and maintenance of an elevated local acidity. As far as the nucleation of pits is concerned, different mechanisms for the initiation of pitting corrosion have been proposed. Various models have been proposed to account for physical phenomena such as, cracking and slow healing of the passive film [32], the development of critical acidity levels in microscopic flaws [33], defect transport in passive films [34, 35], chloride adsorption or incorporation into localized areas of passive film [36], local thinning of the oxide under chloride “islands” [37] or, local acidification related to local adsorption of chloride [38].

Modeling of initiation and growth of pits is typically handled in two different ways [39]: stochastically or deterministically. Stochastic models [40–43] typically describe the likelihood of pit initiation in the form of a probability distribution function (PDF) at a given location under given environmental conditions. These models describe pit growth as a function of time using stochastic fits to experimental data showing how pit size populations evolve through time. These formulations are dependent on experimental parameterization and must be extrapolated to any time or environment not covered by the calibrating experiments. It is however particularly difficult to parameterize the time dependent evolution of such models since, without experimental characterization of the time dependence of growth parameters, these models will predict growth even after a pit repassivates [44]. On the other hand, deterministic models for pit growth are more complex and rely less on time-dependent experimental data. Instead, they rely on fundamental electrochemical physical quantities [39, 45–48]. These models propose a deterministic damage evolution function that uses short-term data to parameterize long-term behaviors [46]. Electrochemical limitations within the description of such models are considered including for example how the geometry of the pit can affect the propagation rate [45] or to emphasize the transport and speciation occurring in the brine layer [25, 45]. Conversely, another class of deterministic models predicts the equilibrium maximum pit depth [49, 50].These models have the advantage of not relying on establishing time-dependent parameters often difficult to parameterize but rather depend on simpler, time-independent, equilibrium electrochemical calculations for the maximum pit size that can form on the surface. However, these models are limited by their assumption to predicting the maximum possible pit size, and do not account for potential kinetic limitations on pit growth.

Third, modeling of the transition from pit-growth to the crack-growth regime is generally handled through two widely used conditions [43]: (i) when the calculated stress corrosion crack growth rate, which increases with depth, exceeds the corrosion pit growth rate, which decreases with depth [51]; or (ii) when the pit depth increases to the point that the equivalent surface crack would have a stress intensity factor (K) that exceeds the threshold stress intensity factor (K_{th}) for crack growth. Typically, atmospheric-induced crack propagation is assumed to obey linear elastic fracture mechanics and behave as a Mode I crack (opening direction parallel to the tensile stress) while assuming the stress intensity factor of a semi-elliptical crack [39, 43, 48]. It has been noted that the pit-to-crack transition is statistical in nature [48], with cracks most often, but not necessarily, nucleating from the bottom of corrosion pits when it is the zone of high stresses [52, 53]. Additional complexities emerge from the fact that the pit-to-crack transition may be dependent on other microstructural features such as grain size or crystallographic texture [54].

Finally, an atmospheric stress corrosion cracking model needs to integrate a crack growth submodel calculating the crack extension in length and in depth as a function of time. Various models are continuously proposed to consider, among many factors, temperature (thermally activated processes), stress intensity factor (crack tip geometry), mechanical loads (exerted or residual), materials properties (e.g., yield strength or degree of sensitization), and environmental factors [26, 55–58]. A critical component of a cracking submodel is the representation of the exerted or residual stresses that must be included for accurate predictions of subcritical crack growth. Such a corollary is especially important in the case of weld residual stresses (WRS). Local tensile residual stresses imparted by the welding process are a primary factor in stress corrosion cracking. Thus, there is a significant body of work to predict and model WRS distribution in welded components [55, 57, 59]. However, this work employs the WRS profile measured in a canister mock-up specifically conducted for the SFWST program [22].

As the review above indicates, while there are many existing approaches for modeling each of the individual processes involved in atmospheric stress corrosion cracking, there are relatively few existing holistic approaches that integrate pit initiation, pit growth, along with the pit-to-crack transition and subsequent crack growth while considering the complexity of the environments in terms of salt concentrations, salt deposition conditions and residual stresses. Examples include pitting and stress corrosion cracking models developed for application to steam turbine blades [47, 48], although these do not explicitly address salt deposition and therefore limit their applicability to atmospheric stress corrosion cracking. One of the rare examples for an integrated model applicable to ASCC is a modeling framework for atmospheric Zn corrosion in a coastal environment, outlined by Cole et al. [3]. This model includes experimentally parameterized models for atmospheric salt concentrations [3], salt deposition [13], pitting, and crack propagation. An expanded methodology was more recently proposed including a detailed model of corrosion under salt-water droplets with porous oxide layers [25]. The importance of integrated atmospheric models results from the assumed importance of factors like time of wetness [25], a condition for minimum relative humidity (RH) [60], and minimum electrolyte layer thickness or volume [6] may be more important to SCC than previously realized.

In light of the above design requirements for developing a comprehensive ASCC model, this interim report describes a holistic model which integrates the various processes controlling atmospheric stress corrosion cracking. As illustrated in Fig. 1.1 and in Sections 3.2–3.7, this framework integrates a suite of submodels to represent the atmospheric conditions including the daily and annual cycles of temperature and humidity associated with the environment, the deposition of chloride-containing aerosol particles on the surface of a corrodible component [10], pit formation model [50] for the maximum pit depth that can be supported for given humidity and temperature conditions, along with a given amount of salt deposited, pit-to-crack transition [51], and crack propagation driven by residual tensile stresses.

This model improves on the preliminary model developed and exercised in Dingreville et al. [1] to predict the life performance of a UNF canisters sites at ISFSIs that are exposed to chloride-containing aerosol particles in both coastal and inland environments. The susceptible material was taken to be 304 and 316 stainless steels, from which the canisters are typically manufactured. The corrosive agent is taken to be chloride ions supplied by deposition of salt aerosol particles present in the atmosphere. The stress field needed for stress corrosion cracking to occur is the measured residual stress present in the welds of a mock-up canister [22]. Performance metrics such as time to pit formation, time to crack initiation, and time to through-wall crack propagation are used to quantify the service life of these canisters. In addition, a global sensitivity analysis [61–63] was conducted in Chap. 5 to identify the processes and model input parameters that had greatest impact on these performance metrics. In turn, such analysis was used as a means to identify data gaps and data needs for model parameterization, validation, and future improvements to this framework.

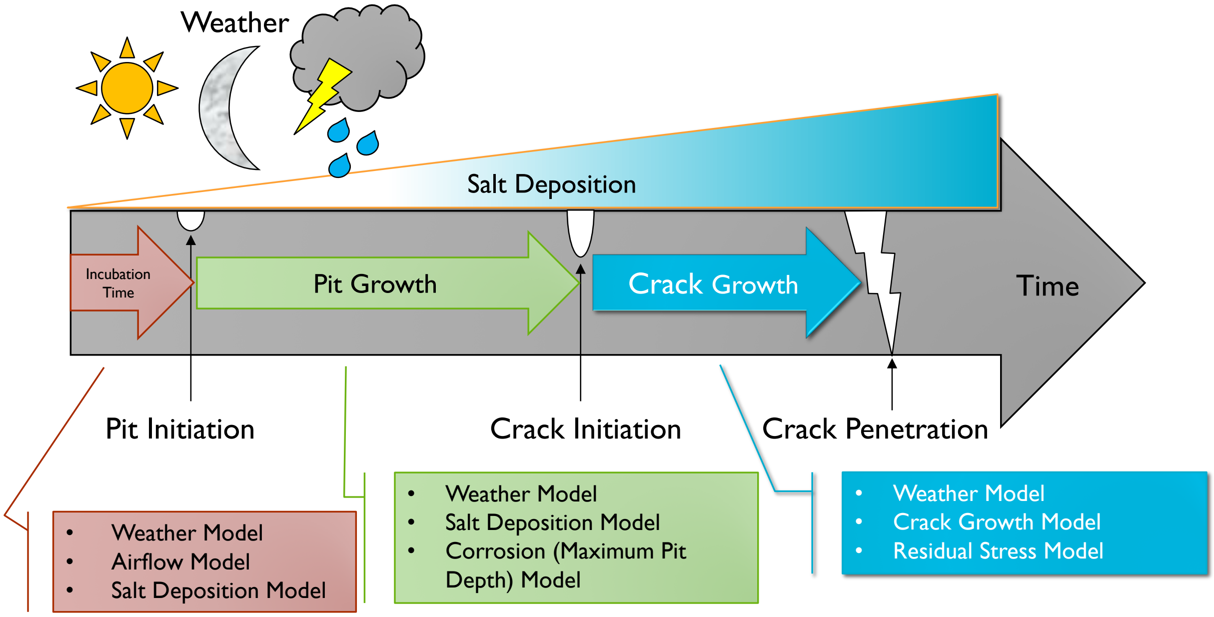

Figure 1.1: Schematic illustrating the submodels

2 Study Description

2.1 Scope

The near-term objectives of the SFWST Campaign's Storage and Transportation (S&T) task within the United States (US) Department of Energy's Office of Nuclear Energy (DOE-NE) are to use a science-based approach to develop the technical bases to support the continued safe and secure storage of UNF, develop technical bases for retrieval of UNF after extended storage, and develop the technical bases for the transport of high burnup fuel after extended periods of dry storage. Prior efforts by SFWST and other organizations (e.g., Nuclear Regulatory Commission [NRC], Nuclear Waste Technical Review Board [NWTRB]) and other countries (including Hungary, Korea, Germany, Japan, Spain and the United Kingdom [UK]) have identified and ranked data needs and modeling needs (also termed "gaps") to complete the technical bases for extended storage. Technical needs were ranked on both their likelihood and the consequence (impact) on licensability and thus safety. Given the large scope, and the large number of high and medium priority data and modeling needs identified for the development of the desired technical bases for the extended storage and transportation of UNF, UQ tools and methodologies are required to provide an informed guidance on the most influential/critical research with the highest payoff (in this case, exemplified by a significantly greater understanding to improve initial or renewal licensing).

2.2 Summary of Changes from Preliminary Report

- Reformulated model from implementation in proprietary GoldSim software to a self-contained portable implementation written in FORTRAN 95.
- Replaced pit initiation model with that of Chen and Kelly [50].
- Replaced NRC modeled WRS data with experimental measurements from Enos and Bryan [22].
- Replaced crack growth parameterization with updated values from Bryan and Enos [21].
- Added chloride particle deposition model that uses particle size distribution, atmospheric concentration, and analytical approximation of fluid dynamics deposition model (including the effects of turbophoresis, gravitational settling, Brownian diffusion, and turbulent diffusion) to predict amount deposited on surface as a function of orientation, air velocity, and temperature [10].
- Addition of code verification unit-tests for quality assurance.

2.3 Task Definitions

This interim report covers a range of topics including:

1. V & V of ASCC capability
2. Global sensitivity analysis
3. Demonstration of model predicting ASCC at an ISFSI
4. A discussion of the technical basis for evaluating the risk of ASCC at sites with active or proposed ISFSIs
5. Preliminary evaluation of risk and uses for the modeling capability's output to that could result in cost savings by predicting canister lifetime to generate inspection schedules at existing ISFSIs while helping to site new ISFSIs.

2.4 Sources of Uncertainty & Data Gaps

Before acknowledging the assumptions that are made in construction of the model, a survey of the current state of knowledge and experimental data is needed to quantify uncertainty in model parameters. The following discussion will identify sources of uncertainty in the environment, the physical mechanisms of SCC, material properties, the manufacture and finishing of the canister, and uncertainty introduced by the numerical model itself.

2.4.1 Uncertainties in the Environment

SCC is driven by a combination of susceptible material, tensile stress, and the presence of corrosive conditions provided by the environment. Ultimately, the variability of the weather and in the supply of corrosive species are important factors, as are variability in the fuel assembly heat load and transfer rate of that heat to the environment.

> **Assumption 1** *SCC can only occur if the deposited corrosive salt is deliquescent. Due to the shelter provided by the concrete overpack, atmospheric humidity is the only supply of moisture to the canister surface. It is therefore assumed that other moisture infiltration such as dripping water for example is disregarded.*

2.4.1.1 Chloride present in the atmosphere

The challenge of determining aerosol chloride concentrations at specific ISFSIs is largely due to a lack of data. The primary source of chloride-containing salt is airborne sea-salt, so proximity to the ocean or brackish water is a dominant factor influencing particle size and concentration [14, 16]. Estimates of atmospheric chloride concentrations are available throughout the U.S. via the EPA's Clean Air Status and Trends Network (CASTNET) of aerosol detectors [64]. However, the CASTNET sites do not overlap with any ISFSIs. Additional complications result from airborne chloride chemically reacting with other ions present in the atmosphere. A chief concern is the replacement of Cl^- with SO_4^{2-} or NO_3^- in sea-salt particulates [27]. Not only is chloride replacement a concern, but those species may also result in corrosion of steel.

The presence of structures [13], including the concrete overpack and canister storage buildings may be important factors. Although little data is available, in a coastal environment, it does not appear that the presence of structures substantially reduces the airborne salt concentration, but the particle size distribution may be reduced [14]. The lack of chloride reduction due to structures contrasts strongly with the conclusions reached by Cole and Paterson [13]. It may be that the actual aerosol chloride concentration and deposition rate is highly site-specific. One aspect of salt deposition that is well supported is that the deposition of salt is a strong function of distance from the ocean. Figure 2.1 uses data from around the world in various climates and terrains. This plot shows the difficulty in establishing a simple model for the chloride deposited at any given site given the wide range of measurements obtained at any site at a fixed distance from the shore.

> **Assumption 2** *Due to the lack of site-specific data, interpolation of CASTNET detector data will be used to provide estimates of the concentration of atmospheric chloride at ISFSIs.*

> **Assumption 3** *Due to the extreme site-specificity of factors such as buildings, foliage, geographic features, and canister overpack, the ambient salt concentration and particle size distribution within the overpack will be assumed identical to the measured values or estimates made outside of the overpack.*

Additionally, the local environment at an ISFSI has significant implications for the supply of atmospheric chloride-containing salts including the nearby application of road salt [17] and proximity to cooling towers [65, 66]. Measurements of salt particle size from cooling towers at the Chalk Point fossil generating plant [66], drawing from brackish waters of the Chesapeake Bay, indicate that nearly the entire mass of salt deposition consists of particles between $300\,\mu$m and $500\,\mu$m in diameter. However, particle size measurements at Crystal River, FL [67], and Indian Point, NY [68] indicate much smaller particles with the most likely being between $20\,\mu$m and $200\,\mu$m. The only airborne salt concentration data available from cooling towers is from two 600 MW fossil units with two natural-draft cooling towers and up to multiple smaller mechanical draft helpers. This data is used to represent an extreme value of salt load as the cooling water is drawn from the ocean. The measurements found a maximum of $18.82\,\mu\text{g/m}^3$ chloride within 0.22 km of the tower (this assumes NaCl is the only source of chloride). Similar measurements for nuclear plants or those drawing from fresh water sources are unavailable. The challenge of accounting for the salt generated by cooling towers is due to the specific direction and distance of an ISFSI from a cooling tower relative to the prevailing winds. This work uses the particle size data from Chalk Point, Indian Point, and Crystal River, to establish bounds to the uncertainty of the particle size. Atmospheric concentration data from Crystal River is used to set an upper bound on the salt source term from cooling towers.

Another potential source of chloride is salt applied to roads for deicing purposes during winter months. A predictive model calibrated with data from I-55 near Lemont, IL, predicts that deposition is undetectable at more than 2.5 km from the interstate highway [17]. This represents an extreme scenario: a wide high-traffic (121,400 vehicles/day) road in a cold climate. As ISFSIs are typically located at active or decommissioned nuclear generating stations, the presence of any road

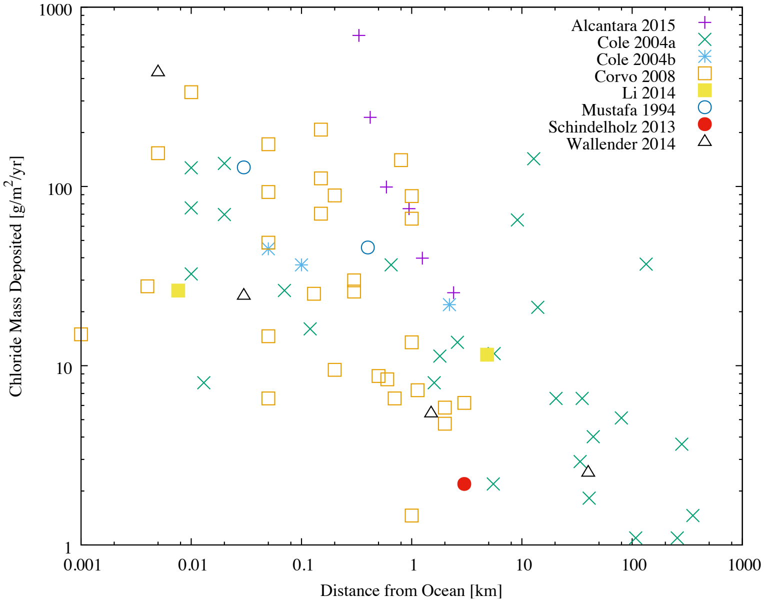

Figure 2.1: Samples of annual chloride deposition onto salt candles and plates at sites around the world as a function of distance from the ocean. References: Alcantara 2015 [2]; Cole 2004a [3]; Cole 2004b [4]; Corvo 2008 [5]; Li 2014 [6]; Mustafa 1994 [7]; Schindelholz 2013 [8]; Wallender 2014 [9].

approaching the traffic density and size of I-55 is unlikely to pass so close to an ISFSI. Near to the ISFSI, much lower traffic roads will be present. Traffic volume has a substantial influence on the amount of salt deposited. The I-55 study does not discuss the effect on long-range atmospheric aerosol concentration. However, for completeness, the source will be considered as an upper-bound to generate conservative predictions for the time to crack penetration.

> **Assumption 4** *The model considers that the chloride ion is the only corrosive species. ANSI standard sea-salt is assumed for calculations of deliquescence, concentration, and pH, regardless of the salt source.*

> **Assumption 5** *The model considers that the chloride ions result from one or more sources: (i) environmental (background) sea-salt (ii) cooling towers, and (iii) deicing (road) salt.*

> **Assumption 6** *Deposition of salt from cooling towers is highly uncertain due to lack of data and not accounting for the amount of time that the plume falls on the ISFSI. The time of expoure is ultimately governed by local weather conditions and the relative locations of the tower, ISFSI, and direction of the prevailing winds. The uncertainty is particularly large for the source concentration term as only a single upper-bound value is currently available.*

> **Assumption 7** *Deposition of salt from nearby roads is highly uncertain due to lack of data and extreme site specificity. The source in this work is taken to be an upper-bound case assuming a large interstate highway in close proximity of an ISFSI.*

2.4.1.2 Deposition of Aerosol Salt Particles

The rate and areal density of particle deposition can be influenced by a number of factors such as air-flow velocity, salt concentration, salt particle size distribution, surface orientation, and surface roughness.

> **Assumption 8** *The deposition of salt particles is an irreversible process. Salt erosion is disregarded. This approximation produces conservative (i.e., larger) estimated salt loadings than might otherwise be expected.*

2.4.2 Uncertainties in Canister Surface Temperature

2.4.2.1 Heat Transfer to the Environment

Heat transfer, and ultimately the surface temperature of the canisters is affected by a number of parameters in the fluid modeling of the canisters. A constant ambient temperature was assumed during modeling rather than one determined by the weather. Uncertainty exists in the amount of heat that is conducted through the cask-to-pad interface. Effects of solar radiation were accounted for using the procedure specified in 10CRF part 71.71. The effect on heat transfer by wind flowing around the overpack or increase in internal convection velocity from wind is not considered. Colleagues at PNNL performed detailed heat transfer calculations using CFD models to calculate the surface temperature and airflow velocity across the canister surface [69, 70]. The temperature values from these studies were used directly and any uncertainty present in the calculations carried through to the present model.

> **Assumption 9** *The variations in environmental temperature are accounted for in the surface temperature model via offsets to a fixed temperature. Uncertainties in solar heating of the overpack, convection cooling, emissivity, and seasonal temperature variation are ignored. Canister surface temperatures are changed by the ambient temperature such that the new surface temperature is determined by shifting the calculated surface temperature value by the difference between the ambient and the calculation's reference temperature.*

2.4.2.2 Heat Generation from Fuel Assemblies

The fluid flow models describing airflow between canister and overpack rely on accurate models of the canister surface temperature. Canister surface temperature is effected by a number of factors, all of which are uncertain, including: the total decay heat, axial temperature profile, assembly axial position, and the presence of non-uniform fuel assembly burn-up or position within the canister. The heat generation, and surface temperature of the canister, is of critical importance for long-term storage. The high temperatures initially present prevent the deliquescence of salt and thus the formation of an environment enabling ASCC to occur. As salt may deposit at all temperatures, it will build up while the canister surface is warm enough to prevent deliquescence, but significant amounts can build over time such that, when the canister is cooler, it may enable ASCC to initiate readily. The location and total heat generated by the decaying fuel is modeled using the ORIGEN-ARP code [71].

Assumption 10 *The uncertainty in decay heat and axial temperature variation of the fuel are accounted for while the non-uniform distribution of fuel loaded within the canister is ignored.*

Assumption 11 *The canister surface temperature is taken to be constant throughout the thickness of the canister wall.*

2.4.3 Uncertainties in Physical Phenomena Associated with ASCC

The mechanisms observed for atmospheric corrosion are similar to those observed in bulk aqueous solutions —namely general and localized corrosion of various forms, including pitting, crevice corrosion, and stress corrosion cracking. Atmospheric corrosion processes are profoundly impacted by the morphology and physical configuration of the corroding surfaces as well as their position relative to any potential sources of moisture or solid contamination. Morphology is determined by surface roughness (scratches) and presence of contaminants (such as chloride-bearing salt particles).

Assumption 12 *This study assumes that corrosion of the canister occurs by the mechanism of ASCC alone.*

2.4.3.1 Pitting and Crack Initiation

Several different mechanisms for the initiation of pitting corrosion have been proposed. It is agreed that corrosion pits propagate as a result of the development and maintenance of an elevated local acidity. As far as the nucleation of pits is concerned, authors have variously emphasized, among other phenomena, inhomogeneity in the metal, cracking and slow healing of the passive film [32], development of critical acidity levels in microscopic flaws [33], defect transport in passive films [35], and chloride adsorption or incorporation into localized areas of passive film [36], local thinning of the oxide under chloride “islands” [37] or local acidification related to local adsorption of chloride [38]. The state of knowledge of the relevant electrochemical parameters is very limited, particularly at elevated temperatures where corrosion may occur in UNF canisters. Even in the electrochemical modeling literature, no models exist for high temperature electrochemical corrosion-related quantities such as the corrosion potential, repassivation potential, or cathodic conductivity. Recently, experimental data has been gathered by Alexander and Schindelholz [18] (funded by the SFWST program), that is used to bound electrochemical parameters such as the Tafel slope (b) and the repassivation current (i_{rp}) at room-temperature. However, no data is available at the present time for elevated temperatures which are particularly relevant to the phenomena of ASCC in UNF canisters.

Due to the lack of knowledge of the mechanism of pit initiation, this work makes the conservative assumption that pit nucleation is not the limiting factor in pit formation; rather, hemispherical pits nucleate instantaneously and their maximum depth is modeled in a way that is consistent with the model proposed by Chen et al. [49, 50]. Hemispherical pits have been observed to form in simulated marine environments on 316 stainless steel [72]. For this work, it is herein assumed that the pit depth is only calculated when the surface RH is greater than a given threshold value as has been observed experimentally [60].

Assumption 13 *The initiation of pitting corrosion is instantaneous once salt is present on the surface and a critical value of RH is attained. Uncertainty in the critical RH needed to initiate pit formation is accounted for in the model. This assumption is conservative since incubation time is disregarded.*

Assumption 14 *Only hemispherical pits are present on the canister surface. This assumption is made to be consistent with the maximum pit depth model employed. Even though actual pits are rarely hemispherical, this assumption is reasonable since pit geometry irregularity has been recognized to only play a secondary role in pit initiation and pit growth.*

2.4.3.2 Crack Propagation

The SCC growth rates in stainless steels have been measured in a variety of environments and are strongly temperature dependent. The range of values for crack propagation has been considered in a wide range of conditions in both immersed environments and humid ones by Bryan and Enos [21]. Deliquescence of marine salts, dusts, or other atmospheric deposits at elevated temperatures may lead to faster crack propagation rates than under natural exposure conditions, but sufficient data exist to estimate crack growth rates over the range of temperatures expected during the extended storage period. Based on data summarized by Bryan and Enos [21] and plotted in Fig. 3.16, propagation rates of up to $56.5\,\mathrm{mm/yr}$ could be reached at 80°C, while a lower bound at 22°C is expected to be $0.174\,\mathrm{mm/yr}$.

Assumption 15 *Uncertainty in the crack propagation rate implicitly accounts for variations in the material properties. Uncertainty associated with crack growth incorporates either implicitly or explicitly key factors including material property factors such as the stress intensity factor, degree of sensitization, and yield stress, and environmental factors such as temperature, chloride concentration, and pH. However factors such as crack profile or non-linearity in the constitutive behavior of the weld materials are not considered.*

2.4.3.3 Weld Residual Stress (WRS)

The WRS present in a canister depends strongly on the geometry and technique used to construct the weld. Variation of material properties and the effects of solidification rate, largely influenced by the rate of weld material deposition, also play a role in increasing the uncertainty of weld residual stresses. Many of these factors are considered in the prediction of weld residual stresses performed by Kusnick et al. [73] at the NRC. However, experimental data from a full-size storage canister have been obtained for the SFWST program by Enos et al. [74]. It is the experimental results that are used in this work to supply the WRS profiles. Material property, including microstructure, variations play a key role in determining the magnitude, and to some extent, the spatial variation of the WRS fields. Weld position and welding sequence play a very important role in the development (magnitude, spatial sequence, tension, or compression) of the WRS fields [55, 57, 59]. In general, a more rapid weld torch speed results in lower weld residual stress fields since the heated region is smaller. For manual field welds used in pressurized water reactor (PWR) fabrication of welds, torch speeds are in the range of 1 to 3 mm/sec and the power inputs (amperage, voltage) are in the range of 200 – 250 A and 10 – 15 V.

> **Assumption 16** *In this study, the above sources of uncertainty are implicitly taken into account by assuming variability in the WRS profile throughout the wall thickness. Due to the uncertainty in the welding process and the location of pit initiation that occurs somewhere between the weld-centerline (WC) and the outer edge of the heat affected zone (HAZ), the WRS profile actually used is somewhere between the two extreme measured profiles. The WRS profile is also assumed to not change with time.*

2.4.3.4 Crevice Corrosion

As with other factors that promote the development of the corrosive low-pH, high-chloride environment, the presence of crevices and crevice corrosion promote the initiation of SCC. There are many potential crevice locations in storage systems, with perhaps the most important being the contact between the canister and the rail in horizontal storage systems. This process may be critical for corrosion and SCC of UNF storage canisters; however, as of today insufficient data are available with direct application to the problem studied in this work.

> **Assumption 17** *Crevice corrosion is not considered to be operating during SCC processes. The depth of a pit is governed solely by the electrochemical maximum pit depth model.*

2.4.3.5 Radiolysis

Another factor that can affect corrosion (including ASCC) is the presence of gamma radiation from the encased fuel leading to the formation of radicals and molecules after radiolysis of the water (and brine) on the surface of the waste canister. Some of the species are highly oxidizing and their reactions in pure water are numerous. In brine solutions, the reactions (and sheer number of species) is complex, including radials and molecules of chloride species. Farmer et al. [75] reviews work performed on gamma irradiation of austenitic stainless steels (such as 304) in water and salt solutions, generally finding that the irradiation increased intergranular SCC even at low chloride concentrations.

> **Assumption 18** *Any effect of radiolysis on the composition of the brine is not considered, nor does radiolysis have any impact on the ASCC model.*

2.4.4 Uncertainties Associated with Material Properties

SCC may lead to either partial or through-wall cracks depending on the residual stress profiles in the fabrication and closure welds. According to Ref. 76, information on the fabrication processes and welding parameters and the resultant residual stress is necessary to determine the consequences of ASCC of the stainless steel canisters.

2.4.4.1 Degree of Sensitization

ASCC occurs in heat-affected zones (HAZ) near welds not only because the weld residual stresses are high in those regions, but also because the steel has become sensitized (localized Cr-depleted zone in the materials). Sensitization lowers the corrosion potential of the steel, resulting in increased localized corrosion (pitting). Because the metal corrodes more readily, it is easier to establish and maintain the high chloride content and low pH necessary at the anodic region, in both the pit and in the SCC. Sensitization has many effects on localized corrosion. Increasing degrees of sensitization correspond to shorter incubation times prior to pitting and crack initiation, formation of more pits and cracks, and more rapid pit and crack growth. Nakayama and Sakakibara [77] estimate that the SCC initiation lifetime can decrease by more than an order of magnitude as the degree of sensitization increases from 0 to 20%, and crack growth rates can increase by a factor of 5, for ASCC conditions. The following inputs to the thermal profile are therefore affected, require estimation, and are sources of uncertainty: On UNF storage canisters, the degree of sensitization varies with the distance from the weld (see for example [77]) and through the cross-sectional thickness of the metal. Variability in the weld geometry, welding process (heat input during welding, etc.) affect the HAZ and sensitization of the materials.

Assumption 19 *It is assumed that the above mentioned effects of sensitization are included implicitly in the corrosion rate data. In the context of this study, no specific effort is dedicated to explicitly model and account for sensitization in a decoupled manner.*

2.4.4.2 Degree of Cold Working

Cold working affects corrosion resistance of stainless steels [78] by reducing the corrosion resistance of the metal (martensite formation), which helps maintain aggressive solution chemistries in local pits, and by increasing the dissolution rate due to an increase in the strain energy (dilatation of the lattice). Uncertainties associated with cold work are inherent to the stainless steels used for welded canisters since available laboratory and field corrosion data summarized in the literature are based on samples with different treatments (including both solution-annealed, which should have no cold-working, and as-received).

Assumption 20 *In the context of this model, and in an effort to limit the parameter input space, cold working is not considered in this study.*

2.4.4.3 Iron Contamination

Contamination of the stainless steel surface with less corrosion-resistant forms of iron (e.g., tool steel, or iron from rails), has been shown to increase the likelihood of SCC due to the readiness of iron particles to corrode and intensify the stability of corrosive solutions in pits and in SCC. While this may seem a minor effect, it has been suggested that instances of SCC at temperatures below 60°C are in many cases due to iron contamination on the stainless steel surface [79].

Assumption 21 *In this pilot study, the potential effects of iron contamination are not considered due to a lack of information.*

2.4.4.4 Surface Finish

Rough surface finishes ($> 1\,\mu$m) can promote initiation of corrosion, apparently by trapping water and chloride ions on the surface [79]. Also, surface grinding can also produce large local variations in stress, which may contribute by increasing strain energy and the dissolution rate of the metal. All storage canisters have rougher surfaces than $1\,\mu$m.

> **Assumption 22** *The potential effects of variable surface finishes are not considered in this study due to lack of quantitative information understanding of their effects on factors such as the critical stress intensity factor* (K_{th}).

2.4.5 Uncertainties in the Manufacturing and Assembly Processes of Canisters

Uncertainties exist in the manufacturing and assembly of the cask, canister and (after removal from the reactor and subsequent pool storage) the fuel assemblies. Some uncertainty considerations include:

- The assumed straightness of fuel assembly and basket cells
- The assumed concentricity of the fuel assembly relative to the basket cell, and the basket relative with canister during assembly process
- The estimated gap size:
  - Gap between basket and inner canister wall dominates thermal resistance in radial conduction path [80, 81].
  - Conduction heat transfer between the basket and the canister wall was neglected [82].
  - Gap between basket and the canister wall is assumed to be nominally 13 mm [83].
  - The emissivity (considering view factor and finished condition) of the inside and outside surfaces of the fuel rods/assemblies and fuel basket are estimated to be 0.8, while the canister and cask are both estimated to be 0.9 [80, 81].
- The estimated pressure applied at the joint contacts
- The estimated gap size:
  - Using separated laboratory components to determine contact resistance [81].
  - Large uncertainties exist in the contact resistance between the heater rod and the flange, as well as the contact heat transfer area

Some cask vendors have provided design documents with geometries that have allowed more precise models to be generated. Modeling of other vendor/cask designs will rely on generic design geometry. Specifically, storage casks are licensed using a generic Safety Analysis Review for Packaging (SARP). Later, minor changes in dimensions and geometry are approved separately and SARPs are not always readily or publicly available. This adds to the uncertainty in the ability to model thermal profile for example. Examples include changing a ventilation pathway, adding screening on ventilation ducts, and adding a flange to the base pedestal.

Assumption 23 *For the purpose of the demonstration of this study, most of the uncertainties associated with manufacturing and assembling processes of canisters have been ignored as they represent a second-order effect.*

Assumption 24 *Locations of the two longitudinal welds along the length of the canister are assumed to be independently and randomly located with respect to one another since their location is not recorded when canisters are placed into the overpack.*

Assumption 25 *Circumferential welds are assumed to be present at the ends and the longitudinal midpoint of the canister. Longitudinal (seam) weld locations are treated as uncertain because their orientation is not reported.*

Assumption 26 *Canisters are assumed to be fabricated from standard 304SS. Uncertainties in the material properties are implicitly included in the uncertainties in crack growth, WRS, and electrochemical parameters.*

2.4.6 Uncertainties Associated with Numerical Methods

Uncertainties exist in the implementation and design of numerical methods and models used to represent all the sub models associated with SCC. For example, since canister and overpack designs are typically complex, thermal models are often simplified and introduce uncertainties. Areas of uncertainty in numerical models include:

1. Choice of spatial and temporal resolution.
2. Absence of detailed geometry of the canisters and estimation of effective materials properties in the analysis (structural for WRS for example, thermal for the thermal profile).
3. Selection of methodology for solving physical mechanisms of interest (empirical model or CFD) for thermal profile, for example).
4. Lack of validation against actual cask and canister measurements.

Assumption 27 *In the context of demonstrating the methodology, uncertainties associated with the numerical methods and models chosen to represent various physical mechanism are not considered in this analysis.*

The report continues with a discussion of the model construction and parameterization in Chap. 3.

3 Model Description & Parameterization

3.1 Integrated Model Structure

Each of the following subsections describes the submodel used for each physical component of the SCC model, including the weather, aerosol deposition, crack initiation, and crack growth components. The environmental SCC code described in this manuscript is implemented in modular FORTRAN95 and utilizes no external libraries, which ensures portability. Additional databases are employed to store information such as brine layer properties (thickness and conductivity) as a function of temperature and RH, residual stresses in the weld, and physical properties of air and water. Storing this data in databases obviates the need for functional implementations, and permits the data to be replaced with data sources for alternative corrosion chemistries or with more detailed data, should it become available.

The program is outlined in Algorithm 1.

```
Read site data;
Read simulation parameters;
Read tabulated data (pH, weather, steam tables, etc.);
for storage site do
    Read site parameters;
    for epistemic sample size do
        Sample epistemic parameters;
        for aleatory sample size do
            Sample aleatory parameters;
            Calculate equivalent current density $i_{\mathrm{eq}}$;
            Calculate maximum voltage drop $\Delta E_{\mathrm{max}}$;
            for time do
                Calcluate weather data for timestep;
            Create canister;
            Initiate cracks using Chen & Kelly algorithm;
            for pit do
                Grow cracks;
            Write pit data;
            Write weather data;
        Post-process;
```

Algorithm 1: Outline of main SCC program

3.2 Canister Submodel

Assumptions applied: 9, 10, 20, 22, 23, 24, 25, 26

3.2.1 Description

The geometry captured by the model is that of a cylindrical canister consisting of four welds illustrated in Fig. 3.1. The segment consists of two plates bent and seam welded (joined along their longitudinal direction) to form open-ended cylinders at welds #1 and #2. The cylinders are then joined to each other with circumferential weld #4. The segment shown can be considered to be joined by circumferential weld #3 to the neighboring segment so that weld #3 is present on both ends of the canister segment.

3.2.2 Parameterization

3.2.2.1 Canister Surface Temperature

Surface temperature is modeled by sophisticated models describing the transport of heat generated from radioactive decay via conduction and convection to the walls of the steel canister. In both models, the decay heat is modeled using the ORIGEN-ARP code [71]. From the canister surface, heat is transferred via radiative, natural convection of ambient air, and conduction through support structures within the concrete overpack. Averaged effects of insolation and average environmental temperature are considered, but is assumed to occur in still air due to the uncertainty induced from variable weather conditions. Airflow about the canister is assumed to be turbulent.

For the horizontal canister a model was constructed with a design basis heat load up to 24 kW [69]. The fuel loading contains 24 CE 14×14 assemblies using data from the generic inland site. A map of the temperature on the surface of the canister is provided up to 92 years in Fig. 3.2. Atmospheric temperature is assumed to be a constant 15.555°C.

For the vertical canister, a model is assumed to have an initial heat load of 30.17 kW [70]. Atmospheric temperature is assumed to be a constant 15.555°C. The decay heat is generated by assuming a generic low-burnup fuel housed in 32 WE 17×17 bundles. A map of the temperature over 75 years is provided in Fig. 3.3.

The availability of only two models with different initial conditions makes a true comparison between horizontal and vertical canisters impossible. However, this report will illustrate results for both orientations at each generic ISFSI to allow for a true comparison. The model can be executed with different initial heat loads based on the decay profiles calculated for the horizontal and vertical canisters. It should also be noted that, even though only decay heats of 24 kW and 30.17 kW are initially considered here, in general, that is toward the upper end of the initial decay heat range for canisters currently in service. The oldest canisters were generally loaded with initial decay heats well below this value. As such, additional heat loads will be considered in the future studies.

3.3 Environment Model

Assumptions applied: 1.

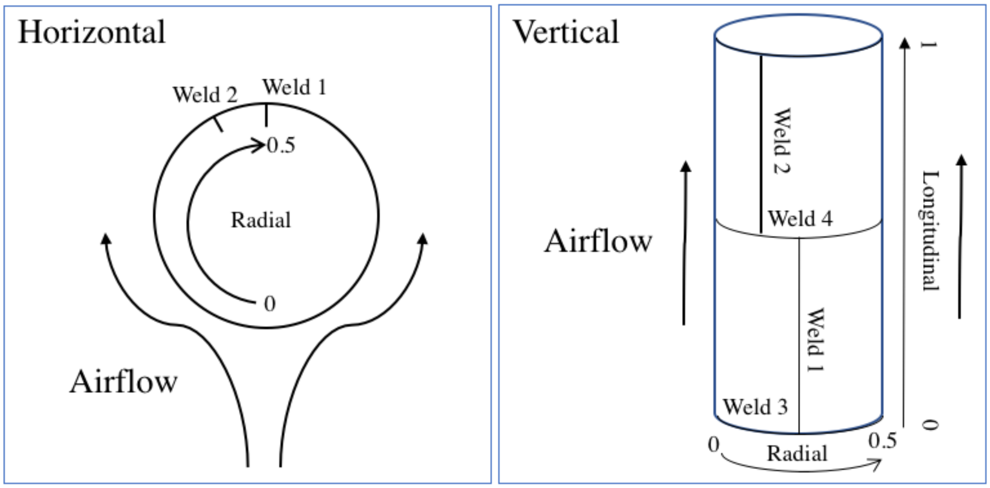

Figure 3.1: Illustration of the geometry of the canisters including the coordinate system, and location of the welds.

The ASCC model contains a description of the atmospheric conditions, including temperatures and dewpoints, that vary daily and over the course of the year. The weather model is parameterized to include stochastic variations that occur in the observed weather data.

3.3.1 Description

The environment sub-model is responsible for supplying the variable weather conditions at a site. The weather is represented as a normal distribution that varies sinusoidally over the course of a year where the timestep (day) is represented by index t. Discretization in time uses two values per day, such that $t = 0.5$ day.

The temperature and dewpoint data is fit to the weather data by defining T_{ref} (mean maximum reference temperature). T_{ref} is calculated using the parameters a_1, b_1, c_1, and d_1 in the equation:

$$T_{\text{ref}} = b_1 + a_1 \sin\left(2\pi\left(\frac{t}{365}\right)c_1 + d_1\right). \tag{3.1}$$

Variability in the weather is described as a reference standard deviation σ_{ref} from the T_{ref} using a representation of the standard deviation parameterized with a_2, b_2, c_2, and d_2 according to

$$\sigma_{\text{ref}} = b_2 + a_2 \sin\left(2\pi\left(\frac{t}{365}\right)c_2 + d_2\right). \tag{3.2}$$

A random number p $(0 \leq p \leq 1)$ is used to calculate the daily maximum temperature sampled from the cumulative distribution function N of the normal distribution $\mathcal{N}(T_{\text{ref}}, \sigma_{\text{ref}})$, where

$$T_{\max} = N^{-1}(p). \tag{3.3}$$

The minimum daily temperature is calculated with respect to the daily maximum with the difference given by the cumulative distribution function Q of the normal distribution $\mathcal{N}(\mu_1, \sigma_1)$, such that

$$T_{\min} = \min\left(T_{\max}, T_{\max} - Q^{-1}(p)\right). \tag{3.4}$$

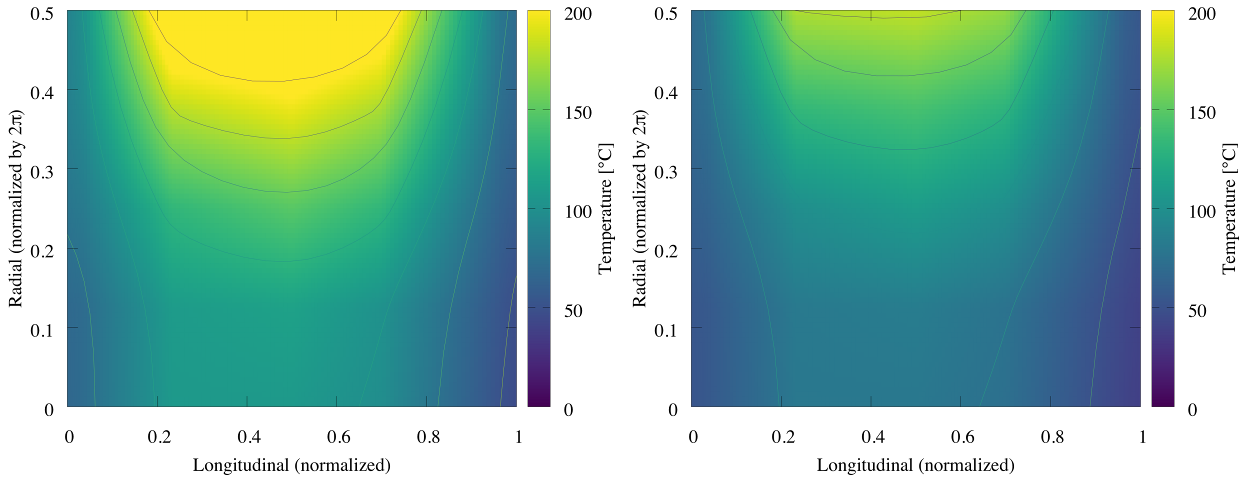

(a) 0 years (24 kW) (b) 7 years (15 kW)

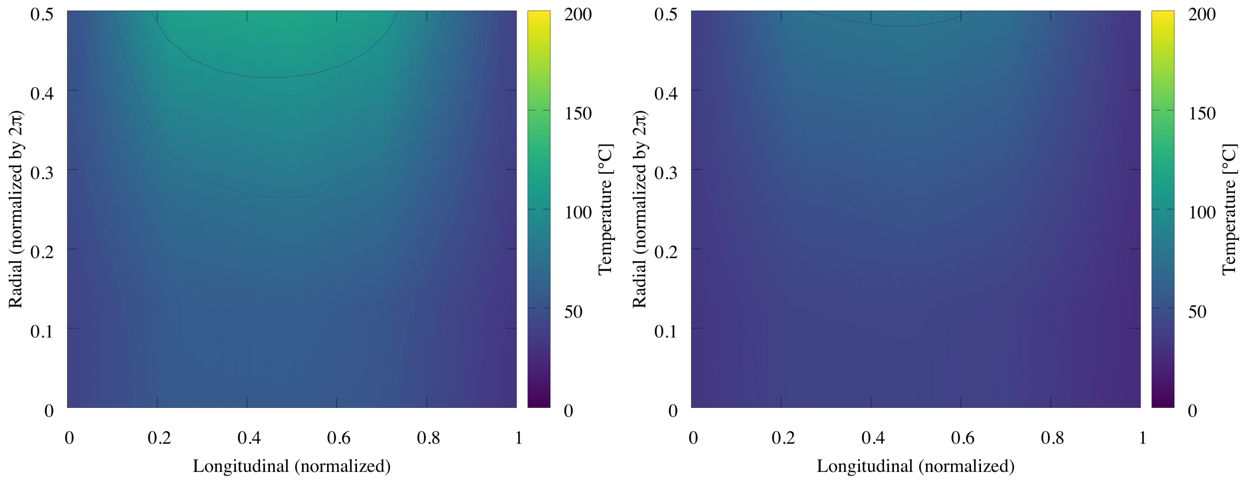

(c) 27 years (8 kW) (d) 92 years (4 kW)

Figure 3.2: Horizontal canister surface temperature distribution for various elapsed times (heat loads) assuming an ambient temperature of 15.555°C. Contour lines are present at 25°C increments. Note, the elapsed time is measured from the initial heat load of (24 kW)

.

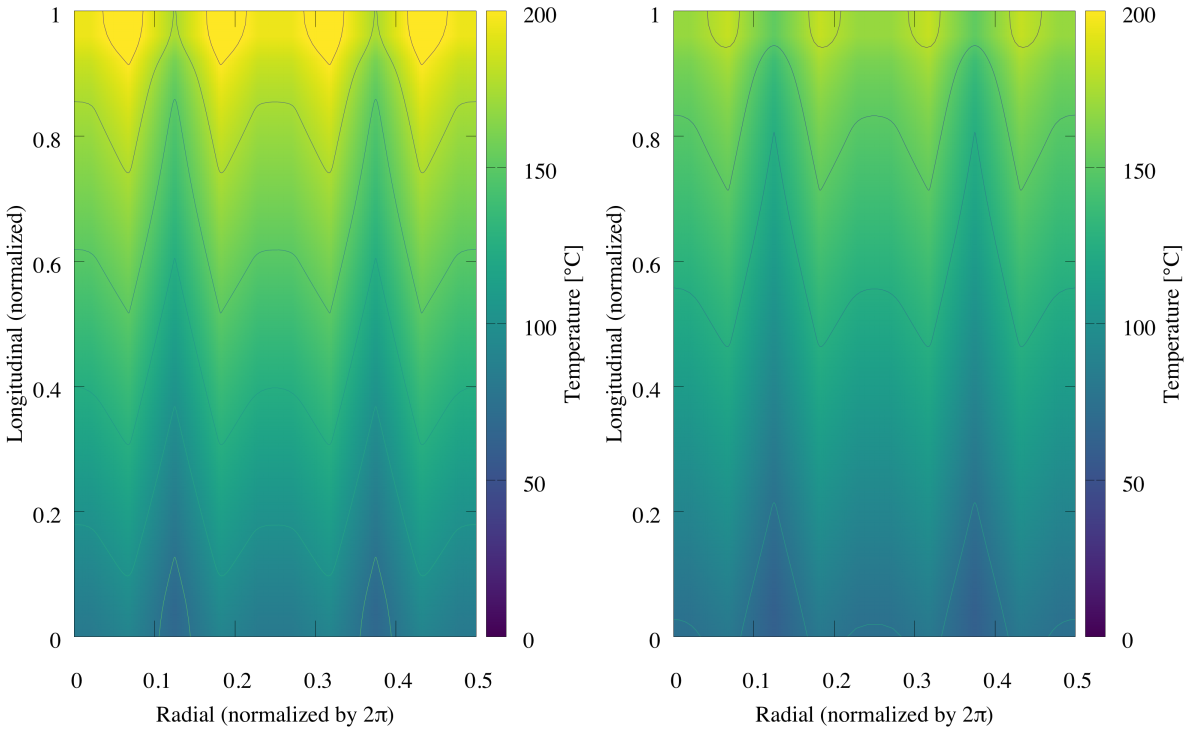

(a) 0 years (30.17 kW) (b) 10 years (24.46 kW)

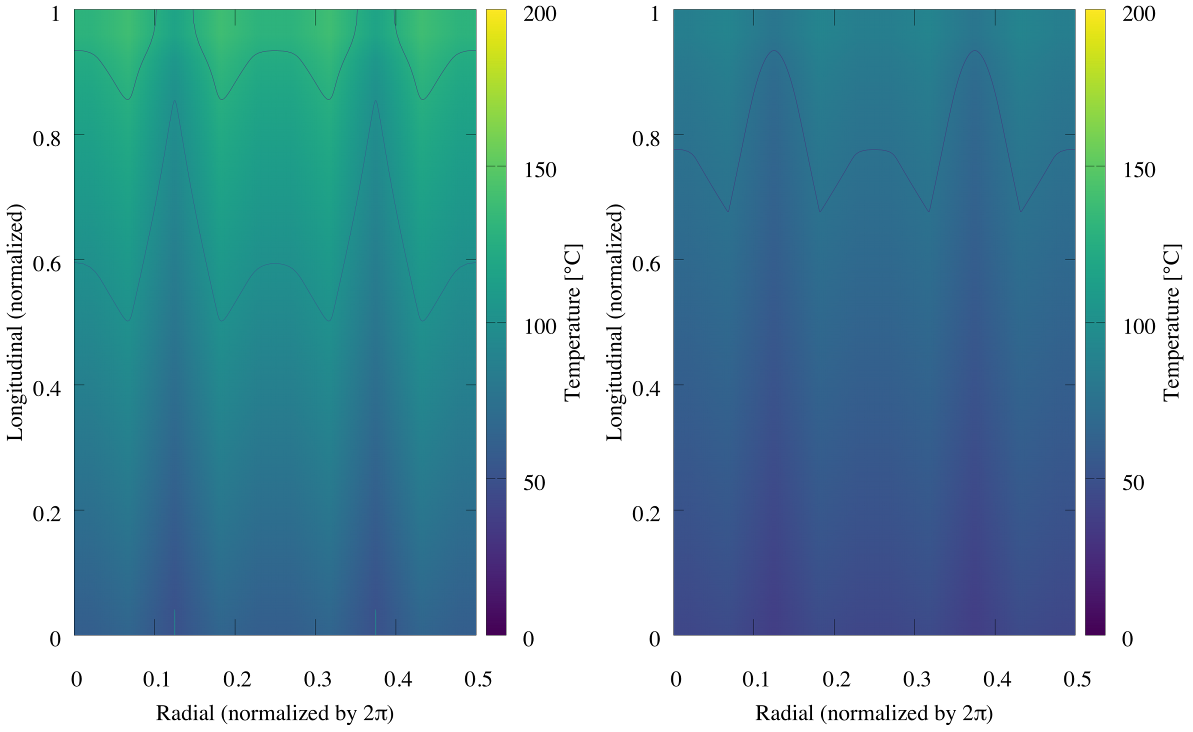

(c) 30 years (16.4 kW) (d) 75 years (8.28 kW)

Figure 3.3: Vertical canister surface temperature distribution for various elapsed times (heat loads) assuming an ambient temperature of 15.555°C. Contour lines are present at 25°C increments.

The dew-point corresponding to the maximum daily temperature is sampled from the cumulative distribution function M of the normal distribution $\mathscr{N}(\mu_2, \sigma_2)$, where

$$(T_{\text{dew}})_{\text{max}} = \min\left(T_{\text{max}}, T_{\text{max}} - M^{-1}(p)\right). \tag{3.5}$$

Similarly, the minimum daily dew-point is sampled from the cumulative distribution R function of the lognormal distribution $\ln\mathscr{N}(\mu_3, \sigma_3)$, where

$$(T_{\text{dew}})_{\text{min}} = \min\left(T_{\text{min}}, (T_{\text{dew}})_{\text{max}} - R^{-1}(p)\right). \tag{3.6}$$

3.3.2 Parameterization

The model is parameterized using NOAA (National Oceanic and Atmospheric Administration) weather data from 2012 to capture the daily variations in temperature and dew points, and the variability of those quantities over the course of a year. The nearest weather station to each ISFSI is used to fit the weather data.

3.4 Salt Deposition Model

Assumptions applied: 1, 2, 3, 4, 5, 6, 7, 8, 10, 11.

In the environments of concern to this model, the corrosive agent is assumed to be chloride salt aerosols that originate from: the ocean, deicing (road) salts, and cooling towers at operating nuclear plants. The model is general enough to account for other ions such as fluorine or sulfur complexes if the pitting corrosion and deposition models are parameterized with the appropriate data. Regardless of the source or corrosive agent, determining the amount of salt deposited on the surface of the canister is of critical importance as it controls the thickness of the brine layer formed by salt deliquescence, which in turn, is a very influential parameter in the corrosion model. The salt deposition model consists of two parts: the deposition velocity, and the deposition flux submodel. The deposition velocity model calculates the velocity of a particle towards the surface as a function of its diameter. With that information, a deposition flux (fowling) submodel is then used to calculate the amount of salt deposited on the surface of the susceptible material.

3.4.1 Deposition Velocity Model

Deposition conditions are strongly influenced by the geometry and orientation of the canister considered with respect to airflow [6, 10–12, 28–31], but also by turbulence and local conditions near the surface of the attacked material [13].

The deposition velocity model employed is the Piskunov [10] version of the isothermal deposition velocity model for particulate deposition in a fully developed turbulent flow proposed by Zhao and Wu [30]. The advantage of using the Piskunov version is that it contains analytical approximations to the integrals described by Zhao and Wu which was validated for particles with a diameter from 10^{-2} to 10^{2} μm. A comparison of the deposition velocity model versus relevant experimental results are presented in Fig. 3.4. While being much more computationally efficient, Piskunov demonstrated that the analytical approximations to the integrals do not result in significant differences from the numerically integrated solution. The model includes terms to account for the deposition mechanisms of gravitational settling, Brownian diffusion, turbophoresis, and turbulent diffusion. The submodel for the particle flux j is

$$j = -\left(\varepsilon_p + D_\mathrm{B}\right)\frac{\partial C}{\partial y} - iu_sC + V_tC, \tag{3.7}$$

where C is the particle concentration, y the coordinate normal to the surface, ε_p is the coefficient of turbulent particle diffusion, D_B is the coefficient of Brownian particle diffusion, V_t is the turbophoretic velocity, and u_s is the gravitational sedimentation velocity. The term i is the orientation factor where $i = 1$ is used for deposition onto a horizontal (floor) surface and $i = 0$ for vertical (wall) surfaces, and $i = -1$ for ceilings. The deposition velocity is defined such that $u_d = j/C_\infty$, where C_∞ is the concentration far from the wall. The submodel assumes that deposition occurs on smooth surfaces. Note that this model does not include any terms to describe entrainment of particles already deposited. This results in a conservative model that will over estimate the amount of salt deposited.

Implicit in the deposition velocity model, the surface temperature of the canister influences most physical properties that are employed by the submodels and is an explicit input to submodels for pit depth, crack growth, and calculation of surface RH. It should be noted that temperature can implicitly affect turbophoresis through the air density, viscosity, and gravitational sedimentation velocity. Within the gravitational sedimentation velocity, the temperature governs the mean-free-path term found within the Cunningham correlation coefficient. Description of such a complex relationship is outside of the scope of the present study. Additionally, the submodel assumed that temperature remains the same throughout the thickness of the canister wall, an important consideration for the crack growth submodel.

The deposition velocity model described by (3.7) was solved for deposition velocity u_d, which has units of velocity, and reported in Eq. 15 [10]. The solution shows that u_d is directly proportional to the friction velocity $u^\star$ that is defined in terms of shear stress τ_w as

$$u^\star = \sqrt{\frac{\tau_w}{\rho}}, \tag{3.8}$$

where ρ is the density of the fluid. The effect of varying $u^\star$ on the deposition velocity is plotted for the cases of deposition onto floors, walls, and ceilings in Fig. 3.5. Note that deposition velocity onto horizontal surfaces converges to a constant value as the friction velocity approaches zero, whereas the deposition velocity onto vertical surfaces and ceilings continuously decreases. The friction velocity is a local quantity that will vary depending with the radial location on the canister with respect to prevailing winds. In practice, detailed fluid dynamics models must be made to calculate friction velocity values that are truly representative of the site being investigated. Such detailed models have been generated by PNNL as discussed in Section 3.2.2.

3.4.2 Deposition Flux Model

Having described the sub-model for the speed of particles traveling towards the surface, the amount of salt deposited may now be calculated using the linear fowling model,

$$m_{t+\Delta t} = Cu_d\rho\ \Delta t + m_t, \tag{3.9}$$

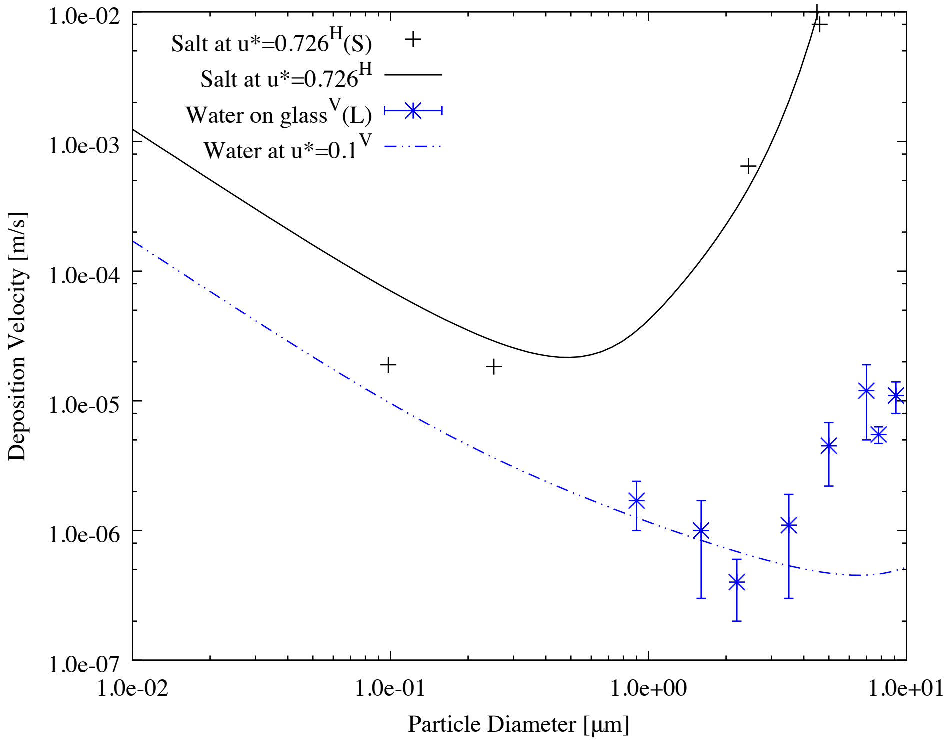

Figure 3.4: Comparison of various experimental results with deposition velocity predictions from the Piskunov [10] deposition velocity model for salt particles and water droplets. Experimental results are plotted with markers and is taken from: (L) Aqueous aerosol deposition onto vertical glass surface [11]; (S) Oxide particles (with density equivalent to salt) on horizontal metal surfaces [12]. Piskunov model results are plotted as lines. The orientation of the surface is noted with superscript H or V to indicate horizontally or vertically oriented surfaces, respectively.

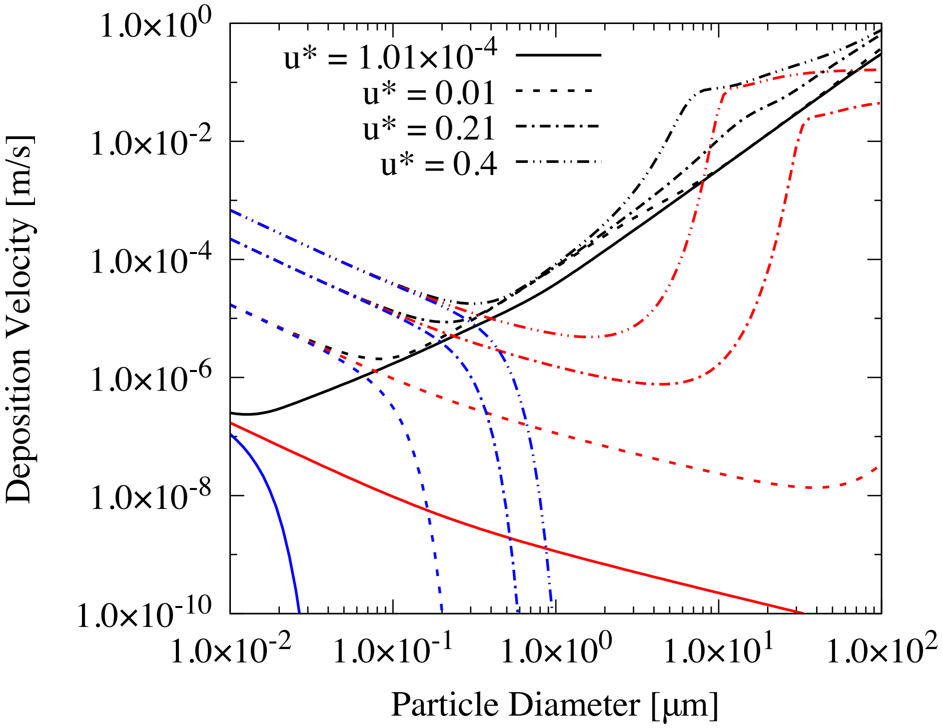

Figure 3.5: Deposition velocity plotted for various values of $u^\star$ for horizontal (black), walls (red), and ceilings (blue).

where m is the areal density of the deposited particles, ρ is the density of air, u_d is the deposition velocity, and Δt is the time step of the model. C is the particle mass concentration in the fluid $(\mathrm{kg}_{\mathrm{salt}}/\mathrm{kg}_{\mathrm{air}})$, defined as

$$C = C_{\%\mathrm{mass}} \frac{s}{\rho}, \tag{3.10}$$

where the source term s is the mass concentration of salt per unit volume of air. The mass distribution of particles as a function of their diameter $(C_{\%\mathrm{mass}})$ may be determined from experimental measurements or models of marine aerosol production (e.g. Fig. 3.10a). For this work, the normalized particle size distribution is described by a gamma distribution:

$$C_{\%\mathrm{mass}}(d) = \frac{d^{k_\gamma - 1} \exp\left(-\frac{d}{\theta_\gamma}\right)}{\Gamma\left(k_\gamma\right) \theta_\gamma^{k_\gamma}}, \tag{3.11}$$

where d is the particle diameter, while k_γ and θ_γ are fitting parameters, referred to as the shape and scale parameters, respectively. The mean of this distribution is $\bar{d} = k_\gamma \theta_\gamma$, and the standard deviation is $\sigma = \sqrt{k_\gamma \theta_\gamma^2}$. Now that a model for the total amount of salt deposited has been established, the next step is to use this information to determine the depth of pits formed on the surface of the metal. These pits will serve as nucleation sites for stress-driven cracks.

3.4.3 Parameterization of Deposition Velocity

In the case of the horizontal canister, the friction velocity $(u^\star)$ is extracted from the fluid dynamics calculations for the model of the horizontal canister located at a generic inland site assuming 15.55°C ambient air, at heat loads with a maximum of 24 kW and assuming turbulent flow. The model is further described in Section 3.2.2 and $u^\star$ is plotted in Fig. 3.6. However, in the case of the vertically oriented canisters, such information is not presently available. In lieu of detailed fluid dynamics models, the deposition velocity submodel provides a way to approximate the value of $u^\star$ by relating it to the experimentally accessible coefficient of friction C_f, defined as

$$C_f = \frac{\tau_w}{\frac{1}{2}\rho U_\infty^2}, \tag{3.12}$$

where U_∞ is the relative velocity of the fluid far from the cylinder. Substituting (3.12) into (3.8),

$$u^\star = \sqrt{\frac{1}{2} U_\infty^2 C_f}. \tag{3.13}$$

The value of C_f for flow around a smooth circular cylinder used in this work is taken from experimental work of Norberg and Sunden [84] for high-Reynolds number flows $\left(\mathrm{Re} = 1.09 \times 10^5 - 2.22 \times 10^5\right)$, and a lower bound at $\mathrm{Re} = 104$ is taken from Dimopoulos and Hanratty [85]. The Reynolds number is defined as $\mathrm{Re} = U_\infty D/\nu$, where ν is the kinematic viscosity of the fluid, and D is the diameter of the canister. For a typical coastal wind speed of $6\,\mathrm{m/s}$ at 25°C, $\mathrm{Re} \approx 1.17 \times 10^5$. The calculation of $u^\star$ is made by first interpolating the results between the two closest experimental values of Re and then applying (3.13), the results of which are plotted in Fig. 3.7. In the next section, the deposition velocity model will be incorporated into the model for salt accumulation.

To approximate the value of $u^\star$ for the case of the canister with vertical orientation and airflow from the bottom, along the length of the canister L, the estimate for $u^\star$ is defined in Eq. 20 of Ref. 28 for a flat plate. (as friction factor is usually applied to flow *inside* pipes),

$$u^\star = \sqrt{\nu \left(\frac{0.074}{\rho\nu}\right)\left(\frac{\rho U_\infty^2}{2}\right)\left(\frac{U_\infty L}{\nu}\right)^{-1/5}}, \tag{3.14}$$

where ν is kinematic viscosity, and airflow speed far from the surface of U_∞.

3.4.4 Parameterization of Salt Source Terms

There are three primary sources of salt deposition:

1. Background salt concentration primarily originating from the ocean
2. Local application of salt for deicing roadways
3. Cooling tower plumes

Each source will be considered separately and will be parameterized with the best available data. Each source can be specified separately in the model, including aerosol concentration and particle size distribution.

3.4.4.1 Background Salt Source

Estimates of environmental chloride salt source terms are based on annual averages provided by the U.S. EPA's CASTNET detectors [64]. The salt source term varies greatly at different sites with the maximum and minimum annual average measured values from 1985 to 2017 in the continental U.S. ranging from $4.988\,\mu\mathrm{g/m^3}$ at Indian River, FL to $0.012\,\mu\mathrm{g/m^3}$ in Pinedale, WY. Figure 3.8 uses the nearest CASTNET site data to generate a map of approximate salt concentration across the contiguous U.S. The annual distribution of chloride concentrations at an ISFSI (indicated by a red circle) are simply that of the nearest CASTNET site. The environmental salt source term at each ISFSI is parameterized with the values contained in Table 3.2. The CASTNET sites are sufficiently far from shorelines to not be useful to quantify the airborne concentration as the distance to the shoreline has a significant impact on the amount of salt deposition observed. For purposes of this analysis, the source terms for the generic coastal sites are assigned values as indicated:

Generic coast 1 Data collected from San Nicholas island is used [86].

Generic coastal 2 Values from EPA salt deposition study by Hindawi et al. [87] .

Generalizing from the data at other coastal sites in Table 3.2, we can infer that the standard deviation of the atmospheric chloride concentration is approximately one-third of the mean annual deposition amount. The sites without direct measurements therefore use one-third of the value of the mean deposition amount.

The distance to the coast Fig. 3.9 is a plot of annualized chloride deposition areal density versus distance from the shore at sites across the world. Although there is substantial scatter in the data that

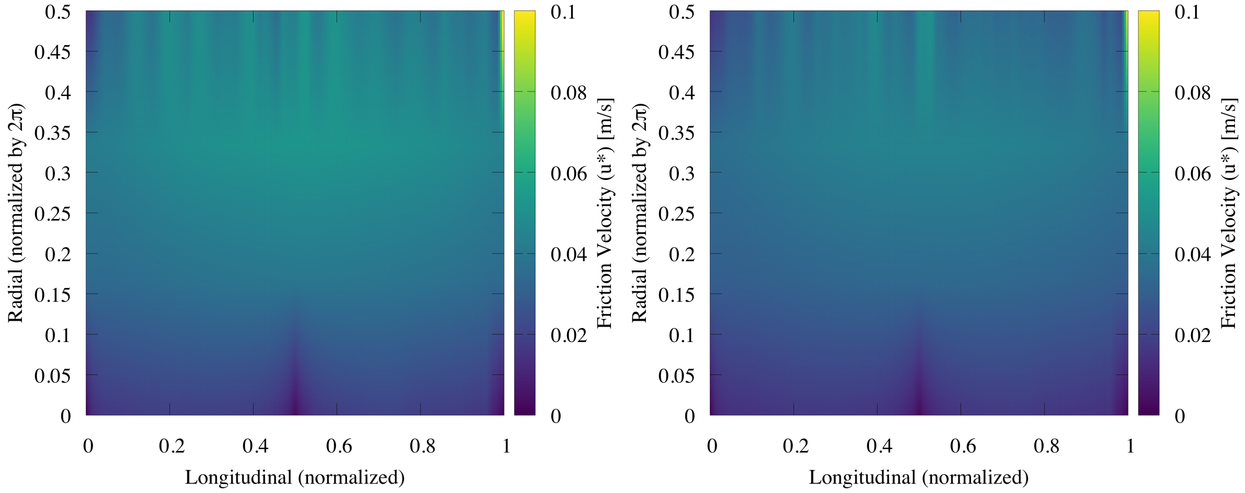

(a) 0 years (24 kW) (b) 7 years (15 kW)

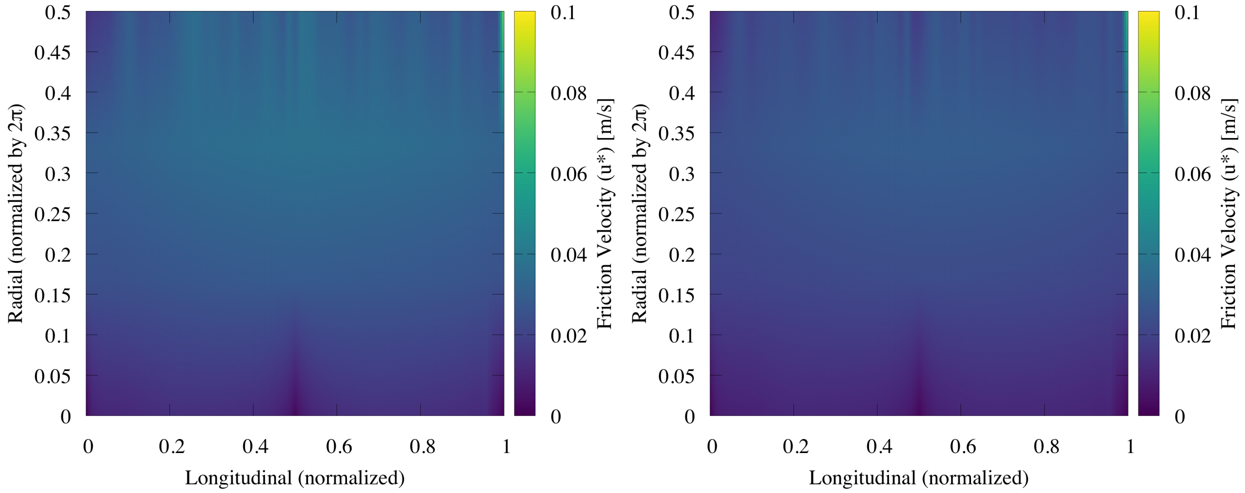

(c) 27 years (8 kW) (d) 92 years (4 kW)

Figure 3.6: Friction velocity calculated over the surface of a horizontal canister within the overpack distribution for various elapsed times (heat loads) assuming an ambient temperature of 15.555°C.

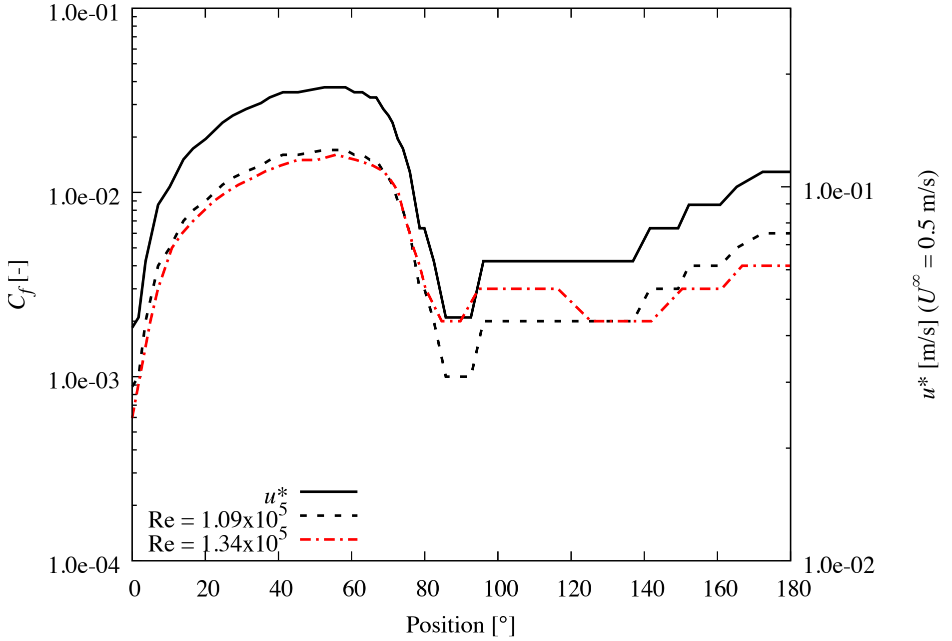

Figure 3.7: Plot of C_f with radial position about the pipe for two values of Re. The wind originates from 0°. The value of $u^\star$ is found using (3.13) assuming $U_\infty = 0.5\,\mathrm{m/s}$.

originates from the measurements being made at many sites with different atmospheric and marine conditions, there is a definite trend towards reduction of salt deposition with increasing distance from the shore. Thus, more reliable data is needed for many of the ISFSIs near the coast.

The size distributions of the particles being deposited is another important input to the deposition model. However, there is very little experimental information on salt particle size distributions. The distributions of Fig. 3.10a are manufactured to approximate experimental conditions representative of coastal [6] and inland [16] sites assuming the chloride source is sea salts. Note that the coastal site has a larger proportion of the total mass in large diameter particles than the inland site. The coastal site's particles were measured to have a mean diameter near $20\,\mu$m while the inland site had a mean near $2\,\mu$m. These distributions are reasonable seeing that the larger particles quickly settle out of the air column as it moves in from the shore.

The empirical particle size distributions of Fig. 3.10a (markers) were fitted using (3.11). Those distributions were obtained for conditions representative of those of coastal [14, Fig. 12] and inland sites [15, Table B-3] assuming the chloride source is sea salts. Note that in the present example the coastal site has a larger proportion of the total mass in larger diameter particles than the inland site. The coastal site's particles were measured to have a mean diameter near $20\,\mu$m while the inland site had a mean diameter near $2\,\mu$m. These distributions are in general agreement with other experimental measurements [6, 16] seeing that the larger particles quickly settle out of the air column as it moves in from the shore [3, 16].

However, there is very little experimental information on airborne salt PSDs. The distributions of Fig. 3.10a are manufactured to approximate experimental conditions representative of coastal [6] and inland [16] sites assuming the chloride source is sea salts. Note that the coastal site has a larger proportion of the total mass in large diameter particles than the inland site. The coastal site's

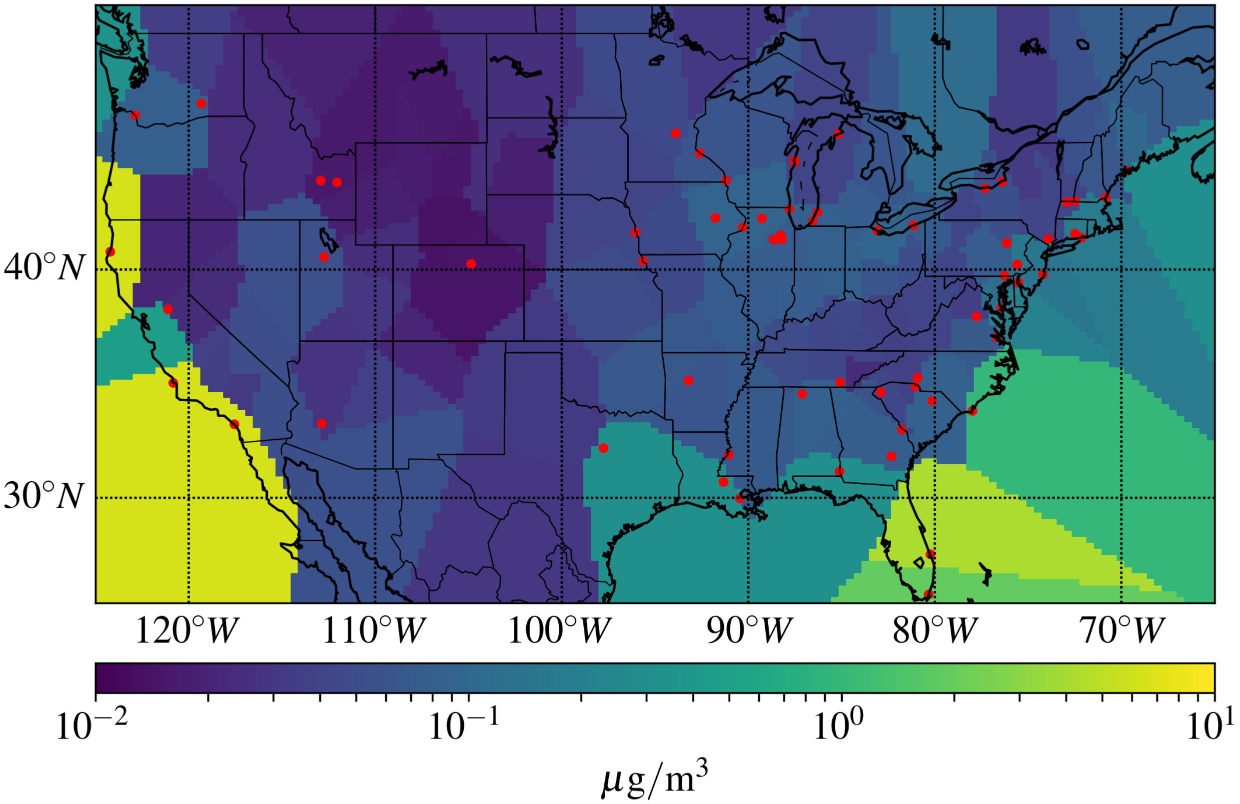

Figure 3.8: Map of the contiguous U.S. with colors indicating annualized mean atmospheric chloride concentration as measured by the EPA's CASTNET detector network. Locations of ISFSIs are marked with circles.

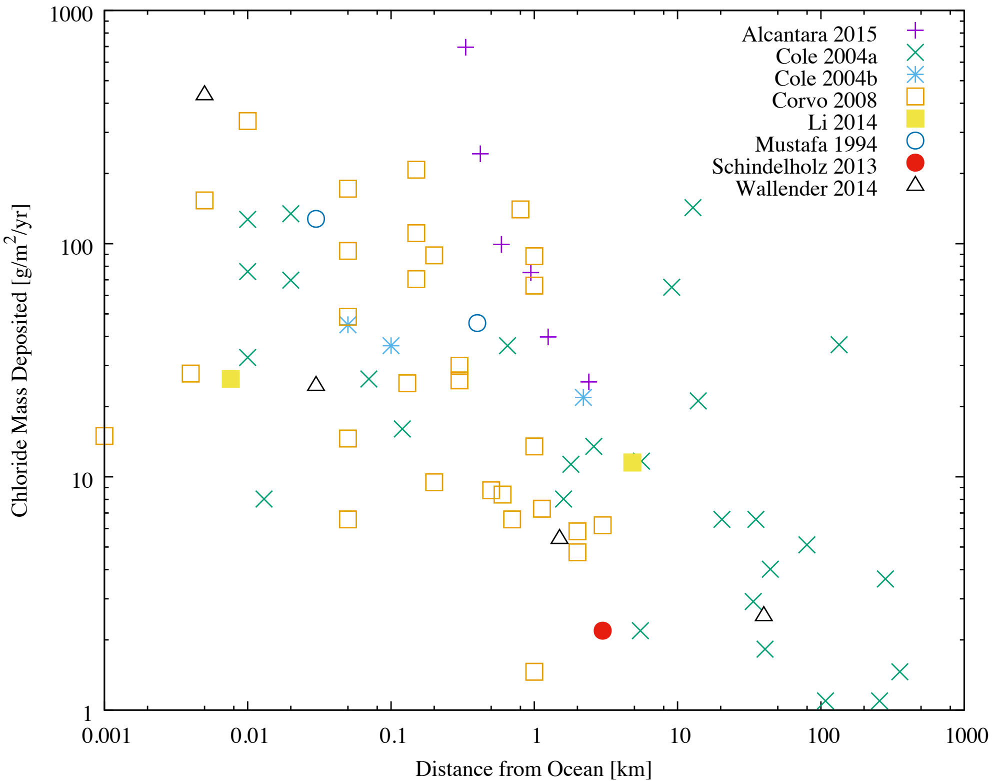

Figure 3.9: Plot of annualized chloride deposition areal density versus distance from the shore at sites across the world. The data clearly show a trend towards the exponential decay of salt deposition with distance from the shore. Data sources include: Alcántara 2015 [2], Cole 2004a [13], Cole 2004b [4], Li 2014 [6], Mustafa 1994 [7], Schindelholz 2013 [8], Wallender 2014 [9].

particles were measured to have a mean diameter near $20\,\mu$m while the inland site had a mean near $2\,\mu$m. These distributions are reasonable seeing that the larger particles quickly settle out of the air column as it moves in from the shore.

The parameterized distribution used in the model is derived from the maximum and minimum values of the parameters of the distributions in Table 3.1, with an arbitrary 15% added or subtracted from the maximum or minimum, respectively, to allow for additional uncertainty. For inland environments, the range of values for the k_γ parameters is chosen to be $2.133 - 4.505$, and the range of θ_γ parameter is $0.565 - 2.770\,\mu$m. For coastal environments, k_γ is in the range $2.289 - 4.694$, and θ_γ is in the range $6.695 - 14.188\,\mu$m. The distributions described are plotted in Fig. 3.10b.

Table 3.2: The mean and standard deviation of the annualized aerosol chloride concentration interpolated from the CASTNET detectors. Location is used to assign the PSD range is either Coastal (C) or Inland (I), and may be marked if in a region where Brackish water (B) is expected. All sites may have additional salt sources which are limited to either a cooling tower (C) or deicing (road) salt (R).

Site	State	Addl. Sources	Water	Longitude [°]	Latitude [°]	Mean Conc. [μg/m^3]	Std. Dev. Conc. [μg/m^3]
Arkansas Nuclear One	AR	CR	I	−93.2308	35.3106	0.0596	0.0129
Big Rock Pt.	MI	CR	I	−85.1955	45.3549	0.0396	0.0033
Braidwood	IL	CR	I	−88.2288	41.2443	0.0745	0.0099
Browns Ferry	AL	CR	I	−87.1151	34.7080	0.0806	0.0179
Brunswick	NC	CR	C	−78.0116	33.9570	0.9972	0.1838
Byron	IL	CR	I	−89.2823	42.0734	0.0902	0.0143
Calvert Cliffs	MD	CR	I/B	−76.4525	38.4319	0.2119	0.0704
Catawba	SC	CR	I	−81.0693	35.0516	0.0840	0.0322
Columbia	WA	CR	I	−119.337	46.4716	0.0792	0.0122
Comanche Peak	TX	CR	I	−97.7853	32.2983	0.3090	0.0965
Cook	MI	CR	I	−86.5659	41.9753	0.0807	0.0119
Cooper	NE	CR	I	−95.6458	40.3589	0.0465	0.0074
Davis Besse	OH	CR	I	−83.0895	41.5954	0.0952	0.0091
Diablo Canyon†	CA	CR	C	−120.851	35.2125	6.3300	2.1100
DOE Idaho Spent Fuel Facility	ID	R	I	−112.057	43.5087	0.0160	0.0019
DOE TMI-2 Storage	ID	R	I	−112.948	43.5702	0.0160	0.0019
Dresden	IL	CR	I	−88.2682	41.3888	0.0745	0.0099
Duane Arnold	IA	CR	I	−91.7832	42.0981	0.0902	0.0143
Farley	AL	CR	I	−85.1125	31.2230	0.3114	0.1173
Fitzpatrick	NY	CR	I	−76.3955	43.5173	0.0523	0.0107
Ft. Calhoun	NE	CR	I	−96.0768	41.5209	0.0465	0.0074
Ft. Saint Vrain	CO	CR	I	−104.873	40.2444	0.0143	0.0012
GE Morris (wet)	IL	CR	I	−88.2720	41.3835	0.0745	0.0099
Ginna	NY	CR	I	−77.3088	43.2776	0.0523	0.0107
Grand Gulf	MS	CR	I	−91.0476	32.0069	0.0695	0.0189
Haddam Neck	CT	CR	I	−72.4909	41.4820	0.1703	0.0484

Site	State	Addl. Sources	Water	Longitude [°]	Latitude [°]	Mean Conc. [μg/m^3]	Std. Dev. Conc. [μg/m^3]
Hatch	GA	CR	I	−82.3438	31.9329	0.0773	0.0270
Hope Creek	NJ	CR	I/B	−75.5375	39.4668	0.1518	0.0521
Humboldt Bay†	CA	R	C	−124.211	40.7420	6.3300	2.1100
Indian Point	NY	CR	I	−73.9526	41.2698	0.0429	0.0078
Kewaunee	WI	CR	I	−87.5373	44.3428	0.0396	0.0033
LaCrosse	WI	CR	I	−91.2316	43.5600	0.0597	0.0136
LaSalle	IL	CR	I	−88.6641	41.2448	0.0745	0.0099
Limerick	PA	CR	I	−75.5832	40.2264	0.1518	0.0521
Maine Yankee	ME	CR	C/B	−69.6931	43.9543	0.3000	0.0929
McGuire	NC	CR	I	−80.9517	35.4331	0.0840	0.0322
Millstone	CT	CR	C	−72.1684	41.3133	0.1703	0.0484
Monticello	MN	CR	I	−93.8919	45.3790	0.0453	0.0079
Nine Mile Pt.	NY	CR	I	−76.4074	43.5208	0.0523	0.0107
North Anna	VA	CR	I	−77.7944	38.0541	0.0364	0.0041
Oconee	SC	CR	I	−82.8936	34.7933	0.0434	0.0116
Oyster Creek	NJ	CR	C	−74.2076	39.8141	0.1518	0.0521
Palisades	MI	CR	I	−86.3145	42.3233	0.0807	0.0119
Palo Verde	AZ	C	I	−112.860	33.3892	0.0286	0.0053
Peach Bottom	PA	CR	I	−76.2687	39.7592	0.1257	0.0496
Perry	OH	CR	I	−81.1453	41.7955	0.0720	0.0113
Point Beach	WI	CR	I	−87.5367	44.2809	0.0396	0.0033
Praria Island	MN	CR	I	−92.6389	44.6199	0.0597	0.0136
Private Fuel Storage	UT	R	I	−112.744	40.5372	0.0546	0.0332
Quad Cities	IL	CR	I	−90.3073	41.7280	0.0902	0.0143
Rancho Seco	CA	CR	I	−121.122	38.3450	0.0233	0.0048
River Bend	LA	CR	I	−91.3333	30.7566	0.3090	0.0965
Robinson	SC	CR	I	−80.1568	34.4025	0.0840	0.0322
Salem	NJ	CR	C/B	−75.5375	39.4668	0.1518	0.0521
San Onofre†	CA	CR	C	−117.556	33.3702	6.3300	2.1100
Seabrook	NH	CR	C	−70.8508	42.8987	0.0652	0.0106
Sequoyah	TN	CR	I	−85.0919	35.2265	0.0432	0.0064
St. Lucie	FL		C	−80.2463	27.3486	4.2639	0.4292
Surry	VA	CR	I/B	−76.6977	37.1655	0.2119	0.0704
Susquehanna	PA	CR	I	−76.1460	41.0918	0.0523	0.0107
Trojan	OR	CR	I	−122.885	46.0416	0.0792	0.0122
Turkey Point	FL	C	C	−80.3312	25.4353	1.9239	0.2538
Vermont Yankee	VT	CR	I	−72.5132	42.7790	0.0400	0.0058
Vogtle	GA	CR	I	−81.7703	33.1407	0.0434	0.0116
Waterford	LA	CR	I/B	−90.4716	29.9955	0.0695	0.0189
Yankee Rowe	MA	CR	I	−72.9271	42.7270	0.0400	0.0058
Zion	IL	CR	I	−87.8013	42.4496	0.0902	0.0143

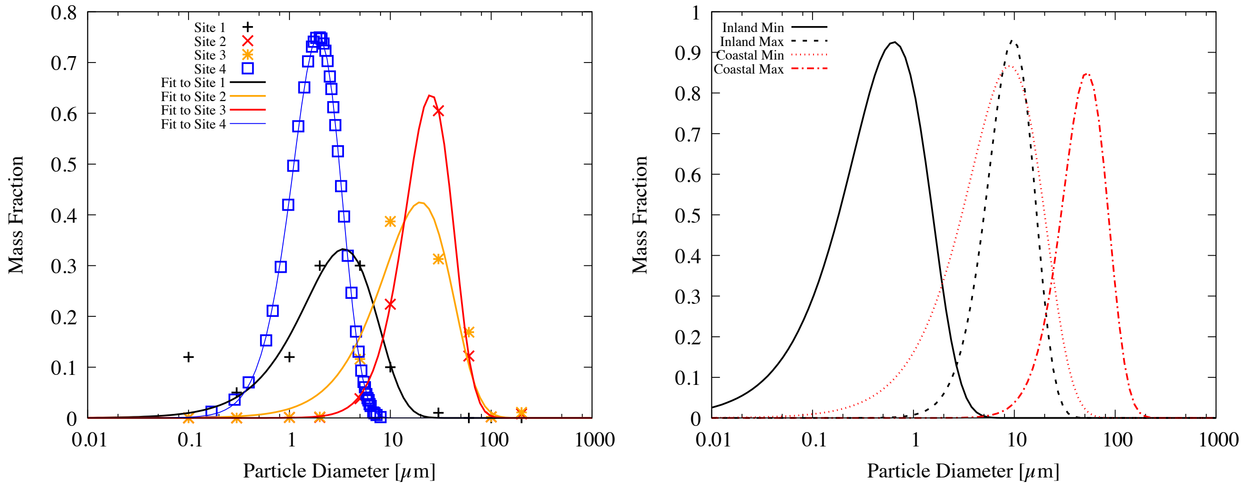

(a) Measured PSD (b) Extreme PSD

Figure 3.10: Measured (a) particle size distribution of salt particles in air for representative coastal and inland environments. Plot (b) shows the extreme values of the representative Coastal and Inland salt particle size distributions used to bound the uncertainty during sampling. Note that distribution heights are arbitrary as the magnitudes are scaled to match the variable atmospheric concentration. Data sources: [14–16].

3.4.4.2 Deicing Salt Source

The deicing salt source term is difficult to parameterize due to the site specificity of this source and limited data. The most comprehensive data is from a series of studies by the Illinois Department of Transportation Interstate-55 site near Lemont, IL from 1996–2002 [17, 88]. A predictive model calibrated with data from I-55 near Lemont, IL, predicts that deposition is undetectable at more than 2.5 km from the interstate highway [17]. This represents an extreme scenario: a wide high-traffic (121,400 vehicles/day) road in a cold climate. As ISFSIs are typically located at active or decommissioned nuclear generating stations, the presence of any road approaching the traffic density and size of I-55 will not pass so close to the ISFSI. Near to the ISFSI, much lower traffic roads will be present. Traffic volume has a substantial influence on the amount of salt deposited. The I-55 study does not discuss the effect on long-range atmospheric aerosol concentration. However, for completeness, the source will be considered as an upper-bound to generate conservative predictions for the time to crack penetration. The summary report by Williams and Stensland [17] reported average airborne concentrations measured during snow events during the time from 1996 to 2002 in Table 1 of that work. The atmospheric source concentrations were fit to a normal distribution having a mean of $1.71\,\mu\mathrm{g/m^3}$ and a standard deviation of $0.307\,\mu\mathrm{g/m^3}$. Particle size distribution data was also provided, but sparsely. For purposes of this work, a best fit to the gamma distribution (3.11) is determined to have a shape parameter of $k_\gamma = 2.197$, and a scale parameter of $\theta_\gamma = 104.248\,\mu$m and is plotted in Fig. 3.11.

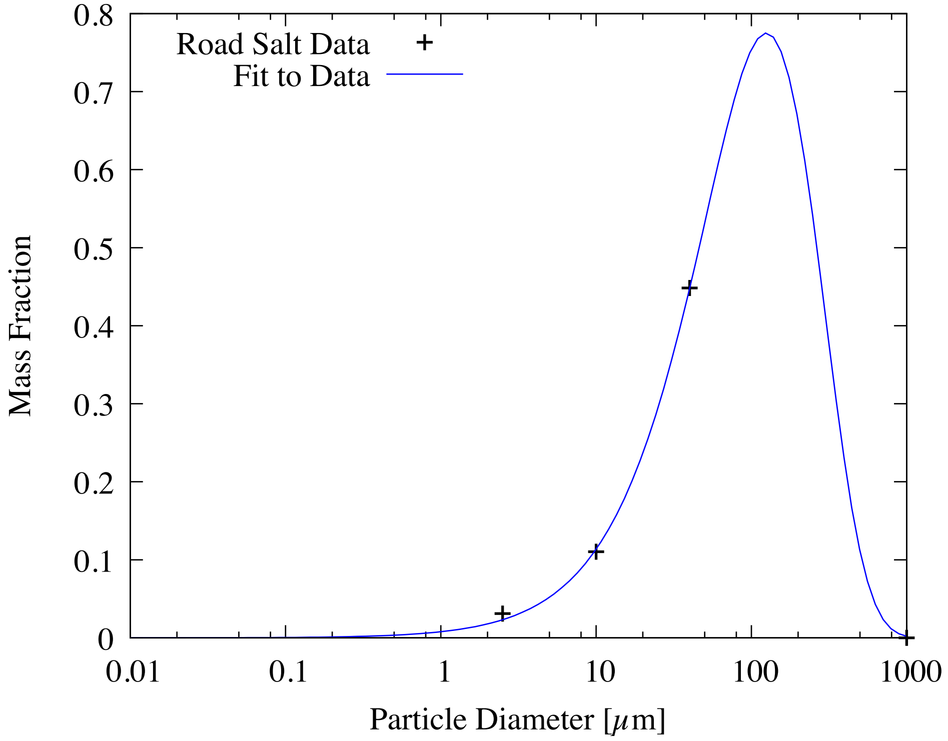

Figure 3.11: Particle size distributions of salt particles resulting from deicing of interstate I-55 near Lemont, IL. Marked data is drawn from Table 1 of Ref. 17.

Table 3.1: Fits to experimental and estimated distributions of salt particle size at various sites representing Coastal and Inland environments. The coefficients correspond to those in (3.11).

Site	Type	k_γ	θ_γ	Mean	Std. Dev.
Generic coastal I [14]	Coastal	4.2672	7.7392	33.0251	15.9871
Generic coastal II [15]	Coastal	2.5431	12.8978	32.8004	20.5683
Generic inland I [15]	Inland	2.3695	2.5185	5.9676	3.8768
Generic inland II [16]	Inland	4.0950	0.6273	2.5688	1.2694

3.4.4.3 Cooling Tower Salt Source

The cooling tower salt source is also site dependent and is difficult to generalize between sites. Many available studies on the deposition of salt from cooling tower plumes are performed at brackish or ocean water sources and represent extreme cases of salt deposition rather than more moderate loading expected at inland sites [66–68, 87].

The only experimental airborne salt concentration data available from cooling towers is from two 600 MW fossil units with two natural-draft cooling towers and up to multiple smaller mechanical draft helpers. This data is used to represent an extreme value of salt load as the cooling water is drawn from the ocean. For Indian Point the maximum aerosol salt concentration due to two natural draft cooling towers the NRC calculated $0.8\,\mu g/m^3$ [68]. However, for the case of the sea water cooled Turkey Point Site, the EPA found a maximum of $18.82\,\mu g/m^3$ at a distance of 0.43 km from the tower and a minimum of $12.43\,\mu g/m^3$ at 0.736 km from the tower [87]. This case represents an extreme one in that the cooling water is drawn directly from the sea. As it represents an extreme case, the Turkey Point atmospheric salt concentration values are used to establish the limits of the cooling tower salt source uncertainty.

Using the available studies, many of the studies provide measurements of the emitted particle size distribution and find it to contain much larger particles than from the sea salt or deicing salt source. The avaliable data for PSD and salt source is summarized in Table 3.3. The Chalk Point fossil generating plant [66], drawing from brackish waters of the Chesapeake Bay, has nearly the entire mass of salt particles between $300\,\mu$m and $500\,\mu$m in diameter. However, other measurements [67, 68] indicate much smaller particles with the most likely diameter falling being between $20\,\mu$m and $200\,\mu$m. The available PSD data are plotted in Fig. 3.12. The θ_γ value is fixed by the desire to keep the particle size distribution below $1000\,\mu$m. The shape parameter is assumed to vary from $k_\gamma = 2.198$ to 31.873, and the scale parameter θ_γ fixed at $11.511\,\mu$m. The value of θ_γ is set to the minimum value in order to make sure the particles stay under $1000\,\mu$m, consistent with experiment.

3.5 Pitting Submodel

Assumptions applied: 2, 4, 11, 13, 14, 18, 19, 26, 27

The evolution of the total amount of salt deposited on the metal surface was used as an input to

Table 3.3: Fits to experimental distributions of salt particle size at various sites. The coefficients correspond to those in (3.11). The origin of the airborne source terms are described in the text of Section 3.4.4.3.

Site	Shape (k_γ)	Scale (θ_γ)	Source [μg/m^3]	Reference
Generic coastal I	2.198	103.844	–	67
Generic coastal I	2.198	103.844	–	67
Generic coastal II	–	–	18.82	87
Generic coastal I	–	–	12.43	87
Generic inland I	2.377	46.971	0.800	68
Generic inland II	18.961	15.904	18.820	66
Generic inland II	28.975	12.790	12.430	66

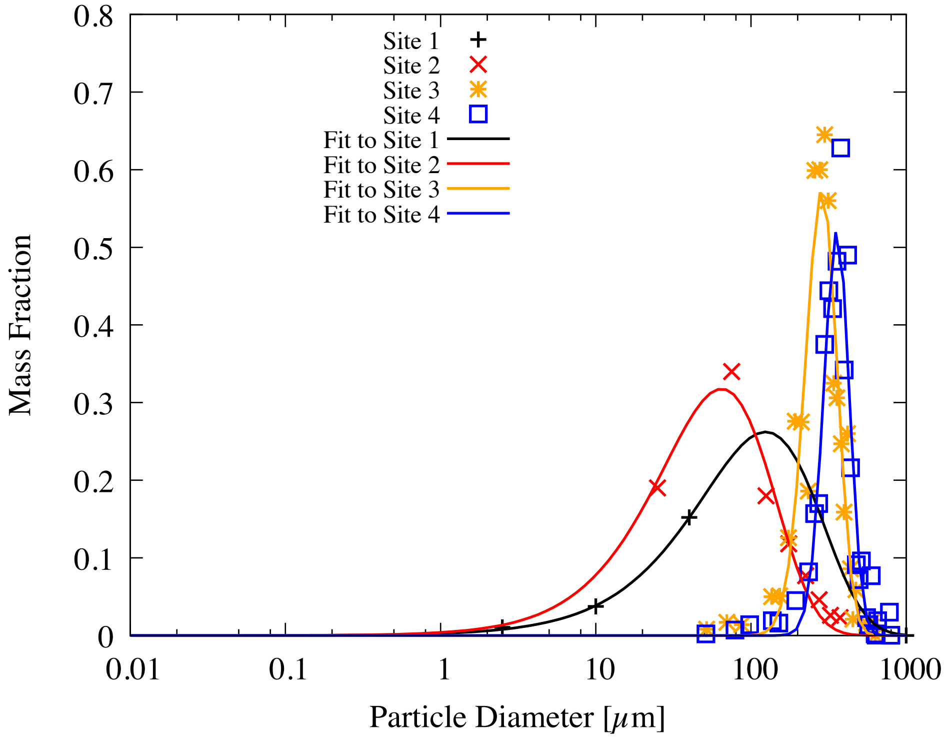

Figure 3.12: Particle size distributions of salt particles generated by natural draft cooling towers.

determine the depth of pits formed on the surface of the metal. This work uses the model of Chen et al. [49, 50] to find the maximum pit depth under given environmental conditions of temperature, salt deposition density, and RH calculated by the deposition, canister temperature, and weather models described in Section 3.2.1, 3.4, and 3.3.1. The implementation herein assumes that the pit depth is only calculated when the surface RH is greater than a threshold value of $\mathrm{R_{th}}$, that will be taken to be in the range from $15-30\,\%$ [60].

3.5.1 Description

The model for pit growth assumes a hemispherical pit, with equivalent radius r_a, that serves as the anode. Hemispherical pits have been observed to form in simulated marine environments on 316 stainless steel [72]. The anode is surrounded by a circular cathode of radius r_eq, both covered with a thin electrolyte (salt brine) layer of uniform thickness t_brine. The submodel determines the depth of the pit using surface temperature, RH, areal deposition density of salt (DD), and interfacial electrochemical kinetics. For any given pit, the anodic current demand must be met by a cathodic counter-current while the anodic current demand increases with pit size. Matching of the anodic current with the cathodic current enables the determination of the maximum pit depth for the given electrolyte conditions at any given time.

The potential at the pit edge (anode) is set to be the repassivation potential E_rp, as it should be for an active pit, while the potential E_L is the corrosion potential at the outer cathode edge. The maximum equivalent current density for the cathode i_eq is therefore

$$i_\mathrm{eq} = \frac{\int_{E_\mathrm{L}}^{E_\mathrm{rp}} \left(i_c(E) - i_p\right) \mathrm{d}E}{E_\mathrm{L} - E_\mathrm{rp}}, \tag{3.15}$$

where i_p is the passive current density at the outer cathode edge, E_L is the corrosion potential at the outer cathode edge, and E_rp is the (repassivation) potential at the anode (pit) edge. The integration is conducted over the cathodic current density function $i_c(E)$. The potential drop from the anode (pit) edge at r_a at potential E_rp to the outer cathode edge at potential r_eq at E_L is given by

$$\Delta E = E_\mathrm{L} - E_\mathrm{rp} = \frac{i_\mathrm{eq} r_\mathrm{eq}^2}{2\kappa t_\mathrm{brine}} \left[\ln\left(\frac{r_\mathrm{eq}}{r_\mathrm{a}}\right) - \frac{1}{2}\right], \tag{3.16}$$

where κ is the conductivity of the brine layer. Defining the cathodic current density as $I_\mathrm{c} = i_\mathrm{eq}\pi r_\mathrm{eq}^2$, solving for r_eq and substituting it into (3.16) under the limiting condition for maximum current such that E_L is equal to the corrosion potential E_corr, the maximum cathodic current is expressed as

$$\ln\left(I_c\right)_\mathrm{max} = \frac{4\pi\kappa t_\mathrm{brine}\Delta E}{\left(I_c\right)_\mathrm{max}} + \ln\left(\pi e r_\mathrm{a}^2 i_\mathrm{eq}\right), \tag{3.17}$$

where e is Euler's number. In this equation, i_eq is given by evaluating (3.15). This expression relates the maximum cathode current to the anode (pit) radius. Additional terms in the previous equation are found from either experiment or detailed models including quantities such as the brine layer thickness (t_brine) and the brine conductivity (κ).

In order to determine the maximum pit depth, the maximum anode current must also be determined. This value is called the pit stability product $I_\mathrm{a}/r_\mathrm{a}$ [89]. To match the anode current and cathode current for equilibrium, the anode current, expressed as $I_\mathrm{a} = (1\,\mathrm{A/m})r_\mathrm{a}$ is set equal to $(I_c)_\mathrm{max}$ from (3.17) from which the maximum value of r_a can be determined.

3.5.2 Parameterization

For many of the parameters in the pit depth model, it is difficult to define uncertainty bounds due to limited data; particularly at high temperatures. This section will discuss the rational for choosing the parameters and uncertainty bounds employed in the probabilistic analysis of sites. First, the Galvele parameter, or pit stability product, has a lower bound for the slope at $1\,\mathrm{A/m}$ [90]. The parameter is experimentally determined to have values between 1 and $3\,\mathrm{A/m}$ for stainless steels [91]. In this work, as in the original work of Chen et al., the most conservative value of $1\,\mathrm{A/m}$ is used.

The brine layer thickness t_{brine} in (3.17) is determined from detailed geochemical modeling of sea-salt deliquescence at different temperatures, and from measured densities for specific brines, with the thickness given in terms of the deposition density of chloride as plotted in Fig. 3.13b. Brine conductivity κ was also measured for selected brines at different temperatures; extrapolation between points allows estimation of brine conductivity at any temperature and RH, as shown in Fig. 3.13c. With the brine thickness, conductivity, and the cathodic current density, the maximum pit depth can be calculated for a given set of conditions. All other parameters needed for the pit initiation model are found in Table 4.1. This work, however, also utilizes analytical models for two additional quantities: repassivation potential E_{rp} and cathodic polarization $i_c(E)$.

The cathodic polarization curve is used to evaluate the integral of (3.15). It can be supplied by experimental data, but in practice the experimental data exhibits time dependent effects and fluctuations in nominally constant values such as E_{L}. As a consequence, this work represents $i_c(E)$ using a functional representation constructed from a measured Tafel slope b (reported in units of V/decade and determined from a fit to (3.18)) with a reference repassivation potential $\left(E_{\text{rp}}\right)_{\text{ref}}$ and reference repassivation current density $\left(i_{\text{rp}}\right)_{\text{ref}}$. These quantities are marked in Fig. 3.13a. These quantities were extracted from Alexander and Schindelholz [18] from experimental measurements reported at 25°C. As these experiments are based on NaCl brines, the data may not apply at lower RH where $\mathrm{MgCl_2}$ increases the $\mathrm{Cl^-}$ concentration in the brine. However, this work assumed that the cathodic polarization data was representative of a brine derived from sea-salt over the entire RH range and in the temperature range explored in this submodel. This data may also vary with temperature and $\mathrm{Cl^-}$ concentration, but no data at other temperatures was available and the experiments have found little dependence on concentration nor on brine layer thickness within the potential range used in this present study. Even though these data were collected for 304SS, due to the lack of data, it was assumed to be applicable to 304SS in the present model.

The cathodic polarization curve is constructed using the aforementioned values as a function of E as

$$i_c(E) = i_p 10^{\frac{E-E_{\text{L}}}{b}}, \tag{3.18}$$

where $\log i_p$[1] is calculated according to

$$\log i_p = \log\left(i_{\text{rp}}\right)_{\text{ref}} - \frac{\left(E_{\text{rp}}\right)_{\text{ref}} - E_{\text{L}}}{b}. \tag{3.19}$$

The analytical form of the integral in the numerator of (3.15), using the functional form of (3.18), is

$$\int_{E_{\text{L}}}^{E_{\text{rp}}} \left(i_c(E) - i_p\right) \mathrm{d}E = i_p\left[\frac{b}{\ln(10)}\left(1 - 10^{\frac{E_{\text{rp}}-E_{\text{L}}}{b}}\right) - \left(E_{\text{L}} - E_{\text{rp}}\right)\right]. \tag{3.20}$$

---

[1] The notation $\log x$ refers to the base 10 logarithm.

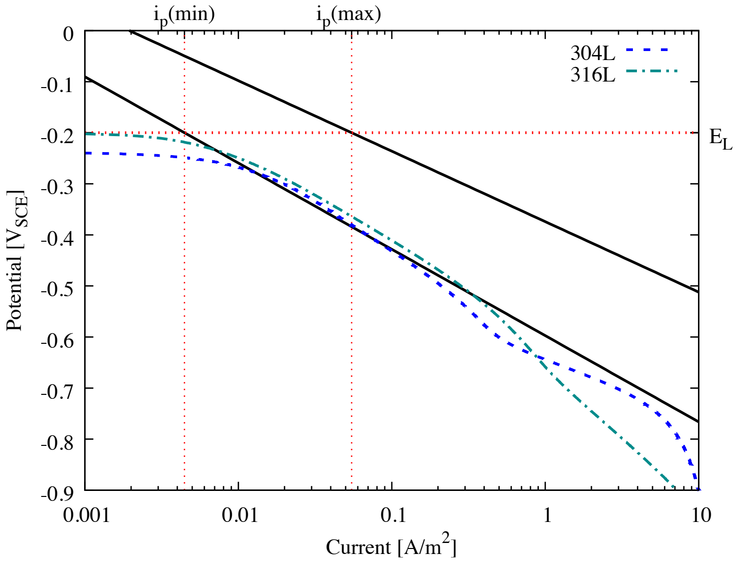

(a) Cathodic Polarization

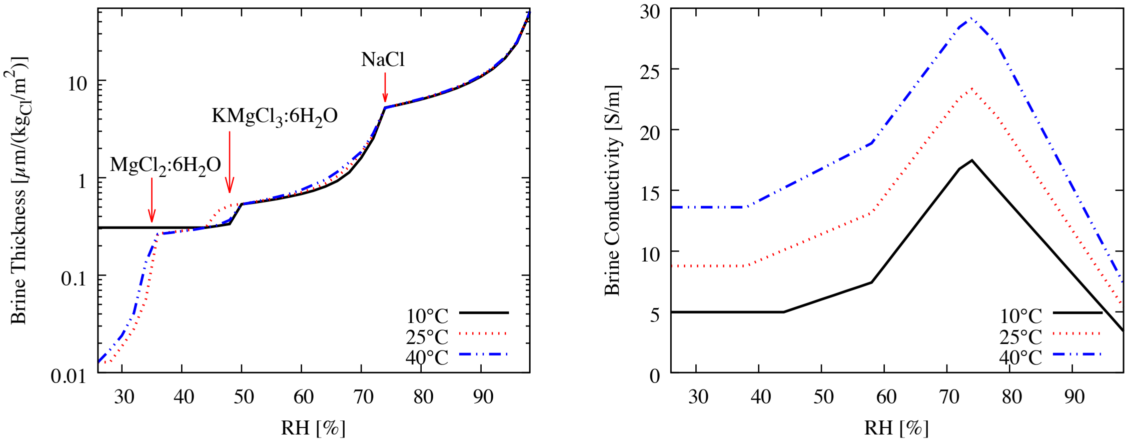

(b) Brine Thickness

(c) Cathodic Conductivity

Figure 3.13: The (a) cathodic polarization data at 25°C is derived from Ref. 18. The (b) brine thickness is plotted and the conditions at which Bischofite $(MgCl_2 : 6H_2O)$, Carnalite $(KMgCl_3 : 5H_2O)$, and NaCl precipitate are labeled for reference. (c) Cathodic conductivity are calculated assuming deliquescence of ASTM standard sea salt, as a function of RH from Ref. 19. Note that the brine thickness is scaled by salt deposition density.

The E_{rp} value is dependent on environmental temperature and species activity. The E_{rp} model is that developed by Anderko et al. [20] that was parameterized for 316L stainless steel up to 95°C. The model divides species into two classes depending on their effects on E_{rp}; these include inhibitory species (with coefficients denoted by I) such as H_2O and OH^-, and active species (with coefficients denoted by A) such as Cl^-. The inhibitory and active species are represented by the left and right-hand sides, respectively, of the equation:

$$\begin{gathered}1+\sum_{j}^{I}\exp\left\{-\frac{1}{\mathrm{R}}\left[\frac{\Delta g^{\neq}_{I,j}}{T_{\mathrm{ref}}}+\Delta h^{\neq}_{I,j}\left(\frac{1}{T}-\frac{1}{T_{\mathrm{ref}}}\right)\right]\right\}\theta_{I,j}\exp\left(\frac{\zeta_{I,j}FE_{\mathrm{rp}}}{\mathrm{R}T}\right)= \\ \sum_{j}^{A}\exp\left\{-\frac{1}{\mathrm{R}}\left[\frac{\Delta g^{\neq}_{A,j}}{T_{\mathrm{ref}}}+\Delta h^{\neq}_{A,j}\left(\frac{1}{T}-\frac{1}{T_{\mathrm{ref}}}\right)\right]\right\}\theta^{n_j}_{A,j}\exp\left(\frac{FE_{\mathrm{rp}}}{\mathrm{R}T}\right).\end{gathered} \tag{3.21}$$

$\Delta g^{\neq}_{A,j}$ and $h^{\neq}_{A,j}$ are the free energy and enthalpy of activation for the dissolution of oxide mediated by active species j. $\Delta g^{\neq}_{I,j}$ and $h^{\neq}_{I,j}$ are the free energy and enthalpy of activation for the formation of oxide mediated by inhibitive species j. $T_{\mathrm{ref}} = 298.15\,\mathrm{K}$ is the reference temperature for the free energy at which the equation was parameterized. F is the Faraday constant. $n_{A,j}$ is the reaction order for aggressive species, and $\zeta_{I,j}$ is the is electrochemical transfer coefficient for inhibitive species.

The sums are performed for all inhibitive and active species as specified in the sum. The θ term is the Langmuir adsorption isotherm for species j as a fraction of all species, defined as:

$$\theta_j = \frac{\exp\left(-\frac{\Delta G_{\mathrm{ads},j}}{\mathrm{R}T}\right)a_j^{\mathrm{bulk}}}{1+\sum_k \exp\left(-\frac{\Delta G_{\mathrm{ads},k}}{\mathrm{R}T}\right)a_k^{\mathrm{bulk}}}. \tag{3.22}$$

The a_j^{bulk} terms are the activities of the components in the brine layer away from the interface, while $\Delta G_{\mathrm{ads},j}$ is the energy of adsorption for species j. When performing the sum over inhibitive species in (3.21), there exists an exception where $\theta_{I,\mathrm{H_2O}} = 1$, regardless of water's activity. The implementation in the SCC model assumes that water activity is given by $a_{\mathrm{H_2O}} = \mathrm{RH}/100$. Hydroxide activity is taken to be the concentration of OH^- ions based on the calculated pH where $a_{\mathrm{OH^-}} = 10^{(\mathrm{pH}-14)}$. Values of E_{rp} generated by the model are shown in Fig. 3.14 for a range of RH values and temperature. It should be noted that Anderko et al. [20] did not specify a range of applicability of the model.

3.6 Crack Initiation Submodel

Assumptions applied: 11, 14, 16, 17, 18, 20, 21, 22, 23, 26

To determine when a pit transitions to a crack, the stress intensity factor K is calculated for an ideal crack of equivalent depth to the maximum pit depth using the approach described in Section 3.5.1. When the value of K at the maximum pit depth exceeds the threshold stress concentration factor K_{th} for SCC to occur, a crack is initiated. This is referred to as the Kondo Criterion [51]. The growth rate of the SCC crack is determined by the temperature and the calculated crack-tip stress intensity factor, defined as

$$K = \sigma Y\sqrt{\pi r_{\mathrm{a}}}, \tag{3.23}$$

Table 3.4: Parameters for the repassivation potential (E_{rp}) model from Anderko et al. [20] as parameterized for 316L stainless steel. The parameterization is valid over the range of Cl^- concentrations from 1×10^{-2} to 10.

	Inhibitive Species		Active Species	Units
Parameter	H_2O	OH^-	Cl^-	
$\Delta g^{\neq}\,(T_{\text{ref}})$	19.31	-3.96	-10.92	[kJ/mol]
$\Delta h^{\neq}$	0.00	0.00	0.04	[kJ/mol]
n	—	—	1.46	[−]
ξ	0.74	0.99	—	[−]
ΔG_{ads}	10.00	10.00	10.00	[kJ/mol]

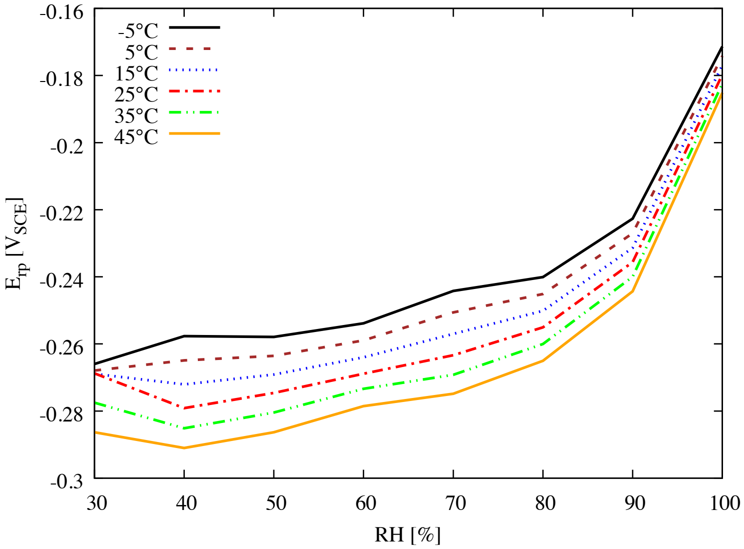

Figure 3.14: The repassivation potential, E_{rp}, is calculated using the model of Anderko et al. [20] as a function of temperature and RH. The activities of OH^- and Cl^- are assumed equivalent to concentrations drawn from tables calculated by Bryan et al. [19] for deliquescent sea salt brines.

where Y is the geometry factor, and σ is the residual stress at the current depth in the weld.

3.6.1 Parameterization

The pit to crack transition is governed by the value of K_{th} that is based on experiments with stainless steels that have demonstrated that the pit to crack transition occurs between 50 and 70 μm for stress corrosion cracking in steam turbine discs [48, 52]. This should only be taken as an approximate value as the actual transition depth will depend on many factors including the residual stress in the material. The preliminary report [1] assumed a yield stress of 238 MPa, and a pit to crack transition depth of 46 μm, so that the threshold stress intensity was estimated to be $K_{\text{th}} = 2.86\,\text{MPa}\sqrt{\text{m}}$. However, the value is subject to change depending on the factors such as the surface finish and the presence of any scratches or gouges from handling, manufacturing, or variation in material properties.

Due to the availability of measured residual stresses in a canister mock-up [22] and using the prior estimate of the pit-to-crack transition, the updated values for K_{th} are calculated using (3.23) with tensile surface stresses ranging from 41.31 to 222 MPa assuming a transition depth between 40 and 70 μm resulting in the range of $0.46 \leq K_{\text{th}} \leq 3.30\,\text{MPa}\sqrt{\text{m}}$.

3.7 Crack Growth Submodel

Assumptions applied: 11, 15, 16, 17, 18, 19, 20, 22, 23, 26, 27

3.7.1 Description

Upon reaching Kondo Criterion, a pit becomes a crack and its depth at future time steps is governed by the model discussed in this section. As the crack growth rate increases with depth and the pit growth rate decreases with depth, the crack propagation quickly outstrips the pit growth rate and any further contributions to crack depth from pit growth are not considered [92]. It should be noted here that, for instance, the data from the work conducted at CRIEPI is counter to this statement, in that it implied crack growth *decreased* with depth. The driving force for crack growth is the residual stresses present in the weld and nearby heat effected zone. The crack propagation model used in this work is expressed as:

$$\dot{x}_{\text{crack}} = \alpha \exp\left[-\frac{Q_r}{R}\left(\frac{1}{T} - \frac{1}{T_{\text{cg}}}\right)\right](K - K_{\text{th}})^{\beta}, \tag{3.24}$$

where $\dot{x}_{\text{crack}}$ is the crack growth rate, Q_r is the activation energy for crack propagation, R is the ideal gas constant, α is the crack growth rate at reference temperature T_{cg}, K_{th} is the threshold stress intensity factor for crack growth, K is the stress intensity factor at the current crack depth, and β is the stress intensity factor exponent. The temperature in the weld T is herein determined by the calculated weld surface temperature (Section 3.2.2) shifted by the ambient environmental temperature. In the parameterization used for this work, the parameters α and β are correlated so that any change in one influences the other. It is important to account for this during sampling of these parameters when conducting a sensitivity study.

Due to the use of linear elastic fracture mechanics, the crack can only propagate when $K > K_{\mathrm{th}}$. Therefore, only residual stresses that are tensile throughout the thickness of the canister wall can cause thru-wall crack growth. Moreover, as SCC cracks form perpendicular to the highest tensile stress, we implement only one weld residual stress (WRS) profile for each weld; the hoop stress for the radial (circumferential) welds, and the axial (longitudinal) stresses for the seam welds. The radial (circumferential) and longitudinal (seam) welds are labeled 1 & 2, and 3 & 4, respectively, as illustrated in Fig. 3.1.

For the application of the model, the activation energy Q_r is parameterized using experimental data for the crack growth rate at 80°C and the rate α at T_{cg}, as:

$$Q_r = \frac{-R}{\left(\frac{1}{353.15\,\mathrm{K}} - \frac{1}{T_{\mathrm{cg}}}\right)} \ln\left(\frac{\dot{x}_{80^\circ\mathrm{C}}}{\alpha\left(K - K_{\mathrm{th}}\right)^{\beta}}\right). \tag{3.25}$$

The crack growth model is parameterized by choosing a value of $50\,\mathrm{MPa}\sqrt{\mathrm{m}}$ for $(K - K_{\mathrm{th}})$ in (3.25) so as to capture the saturation value of $\dot{x}_{80^\circ\mathrm{C}}$ with increasing K. A plot of this relationship is provided in Fig. 3.15 to demonstrate that the increase in rate saturates with increasing K.

3.7.2 Parameterization

3.7.2.1 Crack Propagation

The parameterization for crack propagation rates was taken from Bryan and Enos [21]. Bryan and Enos collected literature reports of atmospheric corrosion of 304/304L stainless steels subjected to chloride ions originating from sea salt or one of its major components (i.e. $MgCl_2$ or NaCl). A wide variety of crack growth rates is observed. The origins of the differences may result from the use of different testing techniques or differences in the material. Sources of variability include a variety of surface treatments including: as-fabricated, annealed, welded, and sensitized. Additionally, some of the samples contained welds and those surfaces were subject to either polishing or grinding treatments. This data at least provides a range of values from which to infer a statistical distribution that will allow UQ techniques to determine how much impact this parameter has to the overall time to through-wall crack penetration.

The recommended value for crack growth rate at 80°C is given by a distribution where $\ln\left(\dot{x}_{80^\circ\mathrm{C}}\right) = \ln\mathcal{N}\left(-20.13553, 1.325\right)$, truncated at 0.022. The reference crack growth rate α at T_{cg} is assigned a distribution where $\alpha = \ln\mathcal{N}\left(-25.921, 1.57\right)$. The stress intensity factor exponent $\beta = \mathcal{N}\left(0.5, 0.2\right)$ was chosen to give a reasonable shape to the growth rate versus stress intensity factor relationship in the absence of sufficient experimental data. In this way, the calculated crack growth rate increases rapidly above K_{th}, but is always less than the saturated growth rate by assuming $K = 50\,\mathrm{MPa}\sqrt{\mathrm{m}}$ as plotted in Fig. 3.15. The preliminary report [1] found that α and β are correlated with a coefficient of $\rho = -0.47$. The calculation of correlated values of α and β

is conducted as follows, where we define the correlated β as β' and the correlated α as α'. Now

$$X_3 = \rho\alpha + \beta\sqrt{1-\rho^2}, \tag{3.26}$$

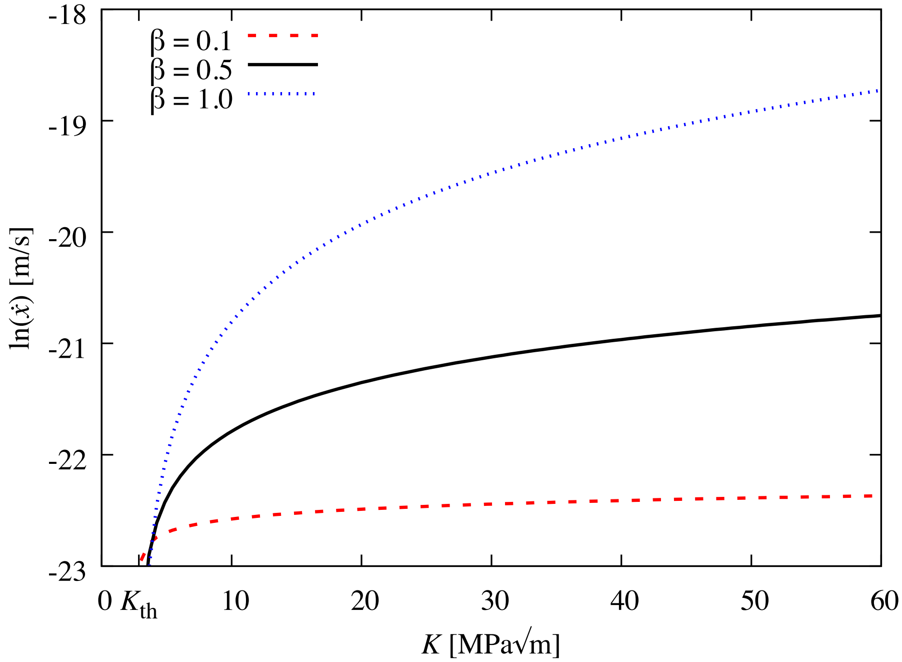

Figure 3.15: Plot of $\dot{x}$ versus stress intensity factor K using (3.24) using parameters from Table 4.1. The growth rate is practically saturated at $K = 50\,\mathrm{MPa}\sqrt{\mathrm{m}}$ with $\beta = 0.5$. Therefore, it is reasonable to use growth rates based on this value to calculate the activation energy.

where,

$$\beta' = \mu_\beta + \sigma_\beta X_3, \tag{3.27}$$

$$\alpha' = \mu_\alpha + \sigma_\alpha \alpha. \tag{3.28}$$

3.7.2.2 Weld Residual Stress

Consistent with the desire to make the sites vary only with environmental parameters is the adoption of the same residual stress through-thickness profile in the welds for each site. The WRS profile is taken from experimental measurements of a full-size 304L stainless steel mockup based on the TransNuclear NUHOMS 24P design for horizontal storage canisters [22].

The experimental data could not be used directly due to variations in weld thickness and the scatter in the ICHD (Incremental Center Hole Drilling) measurements. DHD (Deep Hole Drilling) is used to measure the strain through the thickness of the weld, but is not accurate near the surface. Instead, the ICHD technique is used for near surface measurements from 0.1 mm to 0.499 mm from the outer diameter. However, there is significant scatter in the reported values, so the value from ICHD measurements is averaged and taken to be both the inner and outer surface value. Deeper residual stress measurements are conducted using DHD from the outer surface and are reported at nonuniform increments from 0.8 mm to the some depth less than the wall thickness. Within $\sim$2 mm of the surfaces, the DHD results are reported in increments of 0.2 mm. Because the variable thicknesses of the welds were not provided in the report, the total weld thickness was taken to be

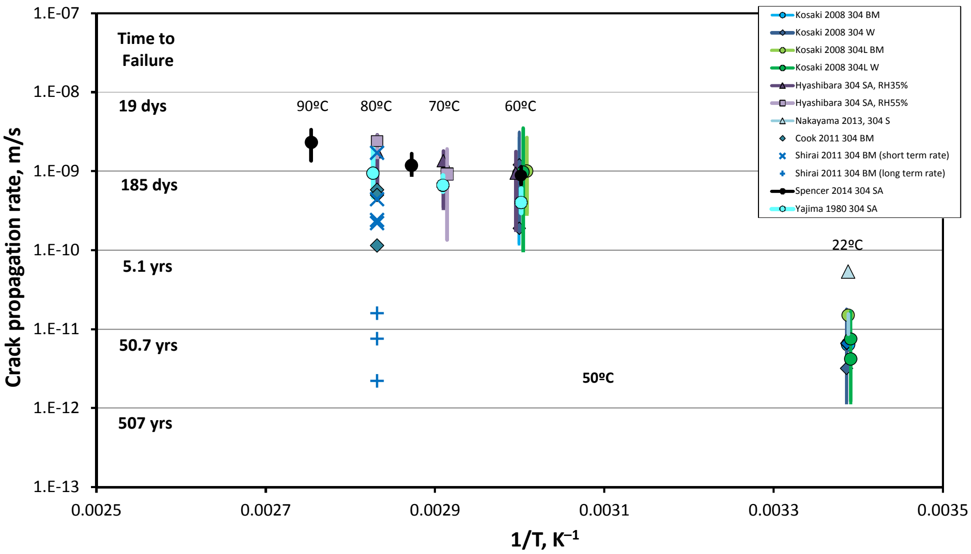

Figure 3.16: SCC propagation rates for atmospheric corrosion of 304 stainless steel. BM-–base metal; W—weld sample; SA—solution annealed; S—sensitized. Bars represent reported ranges (if more than one), while symbols represent average values. *Times to Failure* are for a 15.875 mm thickness, assuming continuous crack propagation over time. The figure is taken from Bryan and Enos [21].

the next 0.2 mm increment after DHD results were no longer reported. This may introduce some uncertainty in the weld profile; however, the code utilizes the normalized depth value to interpolate the value of WRS from the experimental data resulting in precise depth measurements being of reduced importance.

The experimental WRS measurements were captured within the welds' HAZ and along the WC. These values are used to set lower and upper bounds, respectively, for the WRS used in the SCC code. The WRS profiles within the code are plotted in Fig. 3.17.

3.8 Probabilistic Framework

As a result of the known uncertainties and data gaps described in Section 2.4, various model assumptions and simplifications must be made. The majority of assumptions are listed in Chap. 3 in context with the submodels to which they apply, so only more general assumptions will be discussed at this time. In order to conduct the probabilistic evaluation of the sites, a number of premises must be acknowledged:

- A distinction is made between parameters with aleatory and epistemic uncertainty
- Uncertainty in the input results from physical, chemical, material, and environmental properties, as well as submodel parameters
- Parameters have a probability distribution that is based on experimental data. If limited experimental data is available to generate a distribution, a uniform distribution is assumed.

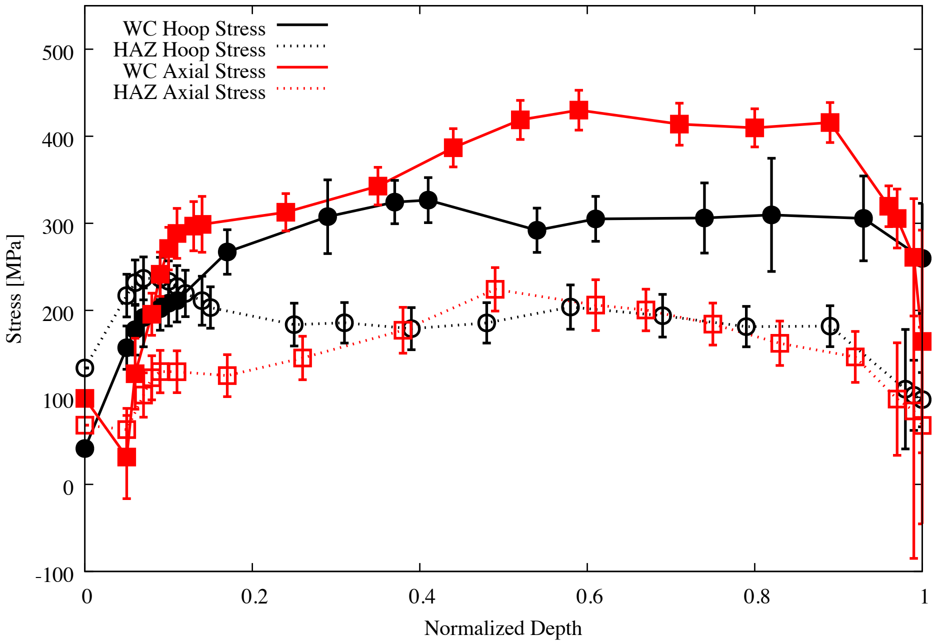

Figure 3.17: Residual stress profiles are presented for the WC and HAZ adapted from Ref. [22] for axial and hoop stresses present in the seam (longitudinal) and radial (circumferential) welds, respectively.

Bounds on the uncertainty distribution may also be generated by engineering considerations if insufficient experimental data is available.

- The most impactful parameters have been considered and are captured within one of the submodels present.

The performance of each site will be evaluated based on a Monte Carlo sampling of model parameters with the uncertainty and uncertainty classification (aleatory/epistemic) provided in Tab. 6.1. Probability distributions will be constructed by sampling all of the parameters with aleatory uncertainty for each sample of parameters classified as having epistemic uncertainty. For this report, 4000 aleatory samples are used to generate a cumulative distribution function (CDF) of elapsed time to an event of interest. The 4000 aleatory samples are made 2000 times, once for each epistemic sample. With 2000 independent CDFs, the post-processing script (`tools/post-process.py`) will calculate and then plot the confidence intervals, mean, and extreme values for each site and canister orientation. This information can be used to provide quantitative estimates of the risk of crack formation for any site.

In the next chapter, the code will be demonstrated in a deterministic setting, with parameters made constant in order to introduce the results generated by the model and elucidate the impact of the environment on a SCC-induced canister penetration.

4 Deterministic Testing

4.1 Deterministic Test Parameters

The holistic ASCC model described in Chap. 3 is exercised for a representative case study. The case study compares SCC performance with environmental conditions representative of a coastal location in close proximity to saltwater to one representative of an continental environment in close proximity to freshwater. At each location, horizontally and vertically oriented canisters are considered to be exposed to variable temperature and humidity conditions capturing the variation at the actual location. The aerosol chloride particles are assumed to originate from a combination of deicing salt from nearby roads, background atmospheric salt, and cooling tower plumes. These sources are intended for illustrative purposes only as sources such as deicing salt may not be continuously applied from mid-October to March as assumed herein. The objective of this example is to show the relative magnitudes of the salt sources and illustrate the impact that environment has on aerosol salt deposition, time to crack initiation, and time to wall penetration.

Table 4.1: Simulation parameters, geometry, and weather parameters used to generate representative inland and coastal cases presented in Section 4.2

	Generic coastal site	Generic inland site
Control Parameters		
Initial Decay Heat [kW]	24.000	24.000
Time [yr]	100.000	100.000
Time Step [dy]	0.500	0.500
Geometry Parameters		
Diameter [m]	0.305	0.305
Length [m]	1.000	1.000
Thickness [mm]	9.000	9.000
Weld #1 Radial Loc.	0.500	0.500
Weld #2 Radial Loc.	0.400	0.400

	Generic coastal site	Generic inland site
Environmental Parameters		
a_1	11.488	3.477
b_1	22.187	21.350
c_1	0.852	0.889
d_1	287.766	253.892
a_2	1.409	1.581
b_2	3.540	2.910
c_2	0.852	0.889
d_2	105.266	71.392
μ_1	16.490	10.650
σ_1	4.340	5.590
μ_2	16.010	8.800
σ_2	6.260	3.610
μ_3	1.720	1.440
σ_3	0.580	0.850
Deposition Model Parameters		
$d_{\text{min}}\,[\mu\text{m}]$	0.000	0.000
$d_{\text{max}}\,[\mu\text{m}]$	1000.000	1000.000
N_{bins}	200.000	200.000
$\rho_{\text{salt}}\,[\text{kg}/\text{m}^3]$	2165.000	2165.000
Crack Initiation Model Parameters		
$(i_{\text{rp}})_{\text{ref}}\,[\text{A}/\text{m}^2]$	0.102	0.102
$(E_{\text{rp}})_{\text{ref}}\,[\text{V}]$	-0.400	-0.400
$b\,[\text{V}/\text{decade}]$	-0.155	-0.155
$E_{\text{L}}\,[\text{V}]$	-0.200	-0.200
$\text{R}_{\text{th}}\,[\%]$	15.000	15.000
Galvele $[\text{A}/\text{m}]$	1.000	1.000
Crack Growth Model Parameters		
Y	1.000	1.000
$K_{\text{th}}\,[\text{MPa}\sqrt{\text{m}}]$	2.860	2.860

	Generic coastal site	Generic inland site
	Crack Growth Parameters	
$\ln(\alpha)$	-25.921	-25.921
β	0.500	0.500
$\alpha-\beta$ correlation	-0.470	-0.470
$\ln(\dot{x})_{80°\mathrm{C}}$	-20.136	-20.136
	Environmental Salt Source	
$s\,[\mu\mathrm{g/m}^3]$	0.200	6.333
k_γ	2.370	2.545
$\theta_\gamma\,[\mu\mathrm{m}]$	2.518	12.877
start day	1	1
end day	365	365
	Cooling Tower Salt Source	
$s\,[\mu\mathrm{g/m}^3]$	15.625	15.625
k_γ	31.873	31.873
$\theta_\gamma\,[\mu\mathrm{m}]$	11.511	11.511
start day	1	1
end day	365	365
	Deicing (road) Salt Source	
$s\,[\mu\mathrm{g/m}^3]$	1.71	1.71
k_γ	2.1969	2.1969
$\theta_\gamma\,[\mu\mathrm{m}]$	104.248	104.248
start day	320	320
end day	59	59

4.2 Deterministic Test Results

A number of environmental differences between the coastal and inland sites were considered to illustrate the effect geographic location has on the susceptibility to atmospheric stress corrosion cracking. The environmental parameters that differ included the weather (temperature, RH), the environmental atmospheric chloride concentration s, and the salt particle size distribution (k_γ and θ_γ). All parameter values used in the model for each geographic site are provided in Table 4.1. Figure 4.1 shows the weather at the (a) coastal (generic coastal site) and (b) inland (generic inland site) sites as calculated by the weather submodel of Section 3.3.1 by fitting measured weather data from representative inland and coastal sites, respectively.

A summary of the results, provided in Table 4.2 illustrate that even with similar total salt deposition (with all sources), there is a nearly 36% difference in the time until crack penetration between the two sites. This clearly illustrates the significant influence the environment has on all aspects of the model. Of secondary importance is the salt source concentration including one or more of: background Environmental (E), Cooling Tower (C), or Deicing Road Salt (R) sources. The geographic location had a substantial influence on the annual maximum deposition density (DD) from environmental (background) salt load, because of the large difference in atmospheric chloride concentration.

DD had little effect on the time to pit initiation. Indeed, this is to be expected since the time to pit initiation is controlled by the timing of deliquescence. As the two sites have similar relative humidity values and canister surface temperatures, it is unsurprising that the pits initiate closely in time. At each site, the pit initiation is the the same for all similarly oriented canisters.

The DD on a weld directly influenced the time to crack initiation without much consequence to the crack growth. The time to crack initiation is expected to be greatly affected by the brine layer thickness as it constitutes a direct input into the maximum pit size model (see Section 3.5.1), while the crack growth rate model is independent of the amount and nature of salt deposited. In all cases presented here, the canister surface temperature is high enough at the time of crack initiation that the crack penetrates the wall within a day of initiating. The large decrease in time to crack initiation with increasing DD also exposes a saturation effect with increasing DD; the reduction in time to crack initiation reaches a minimum, with the minimum value determined by the environmental conditions.

The DD to vertically oriented canisters (Figs. 4.2b and (d)) was smaller in magnitude than in the case of horizontal orientation (Figs. 4.2a and (c)) due to the effects of gravity reducing the deposition rate onto the vertical canisters. From this observation, it is clear that even in the absence of gravitational settling, turbulence (turbophoresis) results in some deposition onto vertical surfaces. In the case of vertical canisters, again it is observed that despite similar salt loadings, the inland canister forms a penetrating crack whereas the coastal site does not. This is likely due to the higher ambient temperatures reached by the inland site.

It must be noted that the maximum annual salt deposition values including all sources are rather large compared to measured experimental values, but this is largely due to the addition of cooling tower and deicing salt sources. A more favorable comparison can be made using only the environmental source at the coastal site and chloride deposition tests at a coastal site in Hawaii. The field experiments found an annual deposition amount of $26\,\mathrm{g/m^2/yr}$, and a test three miles inland resulted in $11\,\mathrm{g/m^2/yr}$ [6]. The maximum DD in the coastal horizontal case is reasonable in comparison to the aforementioned experiments considering the environmental source alone. The large deposition values reported for the deterministic case study point to the need for either better models (such as accounting for varying atmospheric concentration, intermittent cooling tower operation, or prevailing wind direction and speed) or more site-specific experimental data regarding aerosol concentration and particle size distributions.

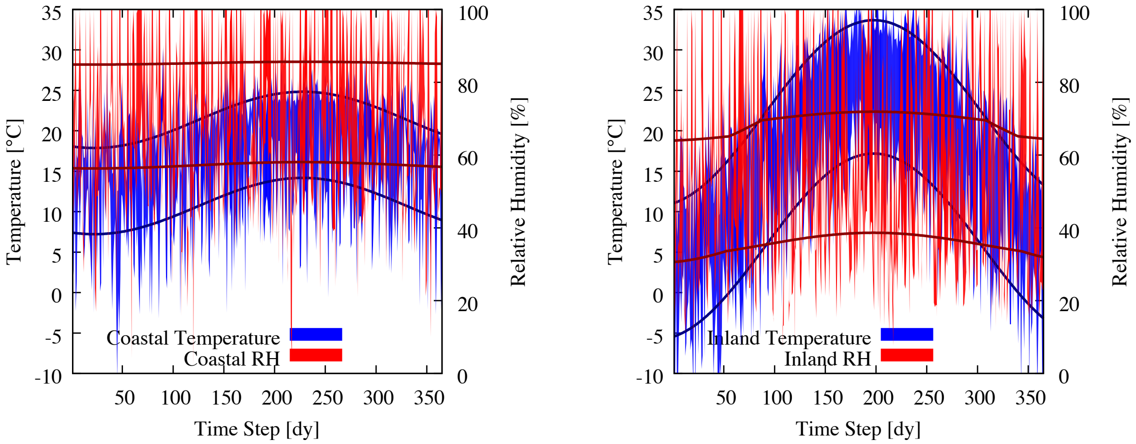

(a) Coastal Site (b) Inland Site

Figure 4.1: A year of simulated weather data is shown for the coastal and inland sites. The RH is shown in red and the temperature in blue with darker colored lines indicating the mean maximum and minimum values for both temperature and RH.

Table 4.2: Summary of deterministic results with times in years. The coastal and inland sites have weather and environmental chloride concentrations consistent with generic coastal and inland locations, respectively. Canister orientation is either Horizontal (H) or Vertical (V). Salt sources include one or more of: background Environmental (E), Cooling Tower (C), or Deicing Road Salt (R) sources. DD is the areal deposition density of the chloride ions.

Site	Orientation	Sources	DD[g/m^2]	Pit Initiation	Crack Initiation	Penetration Time
Coastal	H	E	12.0	6.156	40.189	40.192
	H	R	79.2	6.156	22.414	22.416
	H	C	1361.0	6.156	6.156	6.159
	H	ECR	1451.0	6.156	6.156	6.159
	V	ECR	3.9	10.003	–	–
Inland	H	E	0.002	3.948	–	–
	H	R	77.3	3.948	12.266	12.268
	H	C	1330.0	3.948	3.948	3.951
	H	ECR	1407.0	3.948	3.948	3.951
	V	ECR	3.9	24.096	85.038	85.041

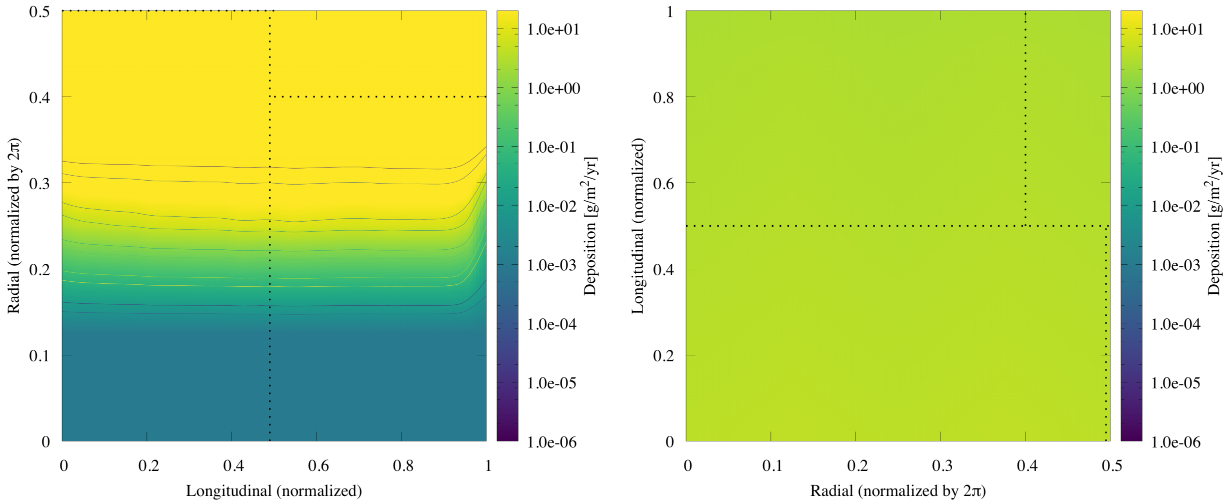

(a) Generic coastal site; Horizontal (b) Generic coastal site; Vertical

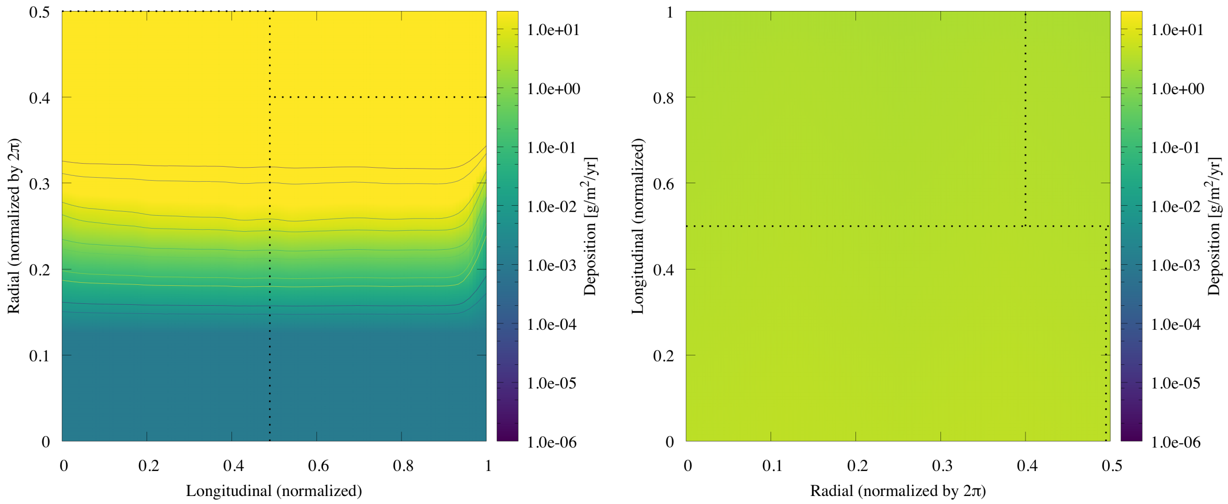

(c) Generic inland site; Horizontal (d) Generic inland site; Vertical

Figure 4.2: Salt deposition after the first year for horizontal and vertical canisters with parameters described in Table 4.1. Contour lines are present in half decade intervals. Broken lines indicate the position of the welds.

5 Global Parameter Sensitivity Study

A variety of approaches can be utilized for not only providing additional insights into the model but also identifying data gaps and data needs for the model parameterization and validation, and future improvements to this framework. Among those, the global sensitivity analysis allows for the identification and ranking of the input variables that have the most/least effect on output quantities from a model [63, 93, 94]. Within this context, Table 5.1 lists the sensitivity of the predicted time to crack initiation and time to thru-wall crack to (i) variations in environmental parameters, (ii) deposition parameters, (iii) pitting parameters, and (iv) crack growth parameters as determined using the Sobol' indices methodology [61, 93].

5.1 Sobol' Indices

The total variance of the response $\mathrm{Var}(T)$, e.g. time to thru-wall crack propagation, with n parameters can be expressed using the second-order Sobol' expansion:

$$\mathrm{Var}(T) = \sum_{i=1}^{n} D_i + \sum_{i=1}^{n} \sum_{j=1,j\neq i}^{n} D_{ij}, \tag{5.1}$$

the contribution of parameter i to the normalized total variance of the response, referred to as the *main effect* index, is

$$S_i = \frac{\mathrm{Var}\left[\mathbb{E}\left(T|x_i\right)\right]}{\mathrm{Var}(T)}. \tag{5.2}$$

In the preceding expression, $\mathbb{E}(T|x_i)$, is the expectation value of T given x_i. Note that $\sum_i^n S_i \leq 1$, as these are only the first-order terms and higher-order effects may also contribute to the total variance. Higher-order contributions to the variance are expressed using the *total effect* index that includes the effect of a single parameter and its interactions with every other parameter [93],

$$T_i = S_i + \sum_{j=1}^{n} S_{ij} = \frac{\mathrm{Var}[T] - \mathrm{Var}\left[E\left(T|x_{\sim i}\right)\right]}{\mathrm{Var}(T)}, \tag{5.3}$$

where S_{ij} is the total effect for the combined effect of parameters x_i and x_j, and $x_{\sim i}$ is the set of parameters not including parameter x_i. Sampling the space of possible variables is computationally intractable, so techniques must be employed to efficiently sample parameter space. To this end, we utilized Sandia National Laboratory's Dakota code [63] to perform a Latin HyperCube (LHC) sampling of parameter space.

Ranges for the parameters considered were chosen to include conditions at both coastal and inland sites including all salt sources and the complete range of particle size distributions discussed when parameterizing the submodels in Chapter 3. Ranges chosen for the parameters in the sensitivity study are listed in Table 5.1, where weather parameters are assumed to be those representing the generic coastal site.

5.2 Analysis

Calculation of the Sobol' indices allowed for the determination of what portion of the variance in the output can be attributed to the variance in each input used within the present atmospheric stress corrosion cracking model. Two sets of sensitivity indices for each input parameter to the SCC model were calculated for each output quantity: the main effect index, S, and the total effect index T. The *main effect* index corresponds to the fraction of the variance of a given output (pit initiation time, formation of a crack, or crack penetration) that can be explained by the variance of that given input variable taken in isolation. Conversely, the *total effect* index corresponds to the fraction of the variance of a given output that can be explained by the variance of a given input variable caused by interacting with the other input variables. The specific algorithm for global sensitivity analysis implemented in Dakota [63] has been used to identify and rank the input parameters most strongly impacting the response of the SCC model. Based on the number of input parameters considered in the model, the total number of realizations performed to achieve statistical convergence has been taken as 59,500 samples. A LHC sampling scheme has been chosen to generate those samples.

All samples resulted in a sustainable maximum pit depth (in other words, all samples led to environmental conditions leading to pitting), while 57,776 resulted in cracks initiating (in other words, 97.1 % of the samples led to at least a pit deep enough to satisfy the Kondo criterion), and 56,532 resulted in cracks that penetrated the wall in less than the chosen limit of 100 years (in other words, 95.0 % of the samples led to cracks propagating through the entire thickness of the canister). In the present analysis, the parameters were sampled from uniform distributions specified in Table 5.1. The results of the variance analysis conducted by Dakota yielded the Sobol' indices reported in Table 5.2. It should be noted that some of the effects are 0 and others are marked with a hyphen. The hyphens mark parameters that have no bearing on that quantity of interest. Zero values for the main effect are not exactly zero and instead indicate that the effect of varying that parameter's value, alone or coupled with others, does not have a significant impact on the model's response. That a parameter has a negligible or zero total effect is not an indication that the parameter cannot affect the outcome but, over the range it is allowed to vary, the parameter does not have a substantial effect. Consequently, the result of the sensitivity analysis is strongly dependent on the range of parameters chosen. Now, the results of the global sensitivity study will be discussed for each response.

5.2.0.1 Time to Pit Initiation

As indicated by the value of the main and total effect indices for time to pit initiation (i.e., time at which conditions are met to form a stable pit), it is clear that only two variables are truly important to governing this response. The top two parameters by main effect, account for 95 % of the variance, are:

1. Threshold RH ($\mathrm{R_{th}}$)

Table 5.1: Summary of parameters and their ranges explored in the parameter study. Parameters not listed in this table are kept constant and set to the values in Tab. 4.1. The sampling distributions include: uniform $\mathscr{U}$; normal $\mathscr{N}$; lognormal $\ln\mathscr{N}$.

Parameter	Distribution	Min.(Mean)	Max.(Std. Dev.)
	Deposition Model Parameters		
Radial Weld Loc. [–]	$\mathscr{U}$	0.000	0.500
$s\,[\mu\text{g}/\text{m}^3]$	$\mathscr{U}$	0.015	18.820
k_γ	$\mathscr{U}$	2.133	31.873
$\theta_\gamma\,[\mu\text{m}]$	$\mathscr{U}$	0.565	104.248
	Pit Depth Model Parameters		
$\left(i_{\text{rp}}\right)_{\text{ref}}\,[\text{A}/\text{m}^2]$	$\mathscr{U}$	0.068	1.540
$b\,[\text{V}/\text{decade}]$	$\mathscr{U}$	-0.169	-0.138
Galvele $[\text{A}/\text{m}]$	$\mathscr{U}$	1.000	3.000
	Crack Initiation Model Parameters		
$K_{\text{th}}\,[\text{MPa}/\sqrt{\text{m}}]$	$\mathscr{U}$	0.460	3.300
$\text{R}_{\text{th}}\,[\%]$	$\mathscr{U}$	15.000	30.000
	Crack Growth Parameters		
Rand. Axial WRS [–]	$\mathscr{U}$	0.000	1.000
Rand. Hoop WRS [–]	$\mathscr{U}$	0.000	1.000
$\ln(\alpha)$	$\ln\mathscr{N}$	-25.921	1.570
β	$\mathscr{N}$	0.500	0.200
$\ln\left(\dot{x}_{80^\circ\text{C}}\right)$	$\ln\mathscr{N}$	-20.136	1.325
$Y\,[-]$	$\mathscr{U}$	0.900	1.100

2. Radial weld location

The lack of sensitivity of pit initiation to electrochemical parameters such as b, the Galvele parameter, and $\left(i_{\text{rp}}\right)_{\text{ref}}$, implies that, over the range specified, the impact on the time to form stable pits does not vary significantly. Similarly with the salt deposition parameters. It appears than any non-trivial salt deposition is sufficient to cause pit initiation. The strong dependence on radial weld location is due to salt deposition being a strong function of canister surface orientation. Pits that form cracks (which evaluated in this test here) typically form in radial (seam) welds for the parameters selected here so the radial weld's radial position is significant. In other circumstances, where the tensile component of the WRS in the circumferential welds was greater, radial weld position may not be important as penetrating cracks would form in circumferential welds instead. However, the most impactful parameter is clearly R_{th}. This value is not known with much certainty and should be a priority for further work to reduce uncertainty of the ASCC model.

5.2.0.2 Time to Crack Initiation

Crack initiation occurs when the Kondo Criteria is met, where $K \geq K_{\text{th}}$, and is highly sensitive to a number of parameters, including, in decreasing order of sensitivity:

1. Atmospheric Salt Concentration (s)
2. Parameterization of chloride particle size distribution $\left(k_{\gamma}, \theta_{\gamma}\right)$
3. Critical Stress Intensity factor for crack formation (K_{th})
4. Radial weld location

The top four parameters account for 88 % of the variance. The salt source parameter s most strongly influencing the variation in time to crack initiation. Unfortuantley, this is one of the parameters that is known with little confidence, as the contribution from cooling towers and deicing salt application are variable and highly site-specific.

5.2.0.3 Time to Crack Penetration

This response of the model is related to the structural integrity of the canister. Upon examination of the Sobol' main effect indices, the crack growth prefactor $\ln(\alpha)$ (proportional to the crack growth rate under a specific set of reference conditions), the salt concentration s, and the surface temperature appear as the parameters impacting the most the variation in the time to crack penetration. A closer look at the *total effect* indices reveals the interacting effects of both the crack growth rate parameters ($\ln(\alpha)$, β, $\ln\left(\dot{x}_{80^\circ\text{C}}\right)$) and atmospheric salt concentration (s) on the variability to be expected on the time to thru-wall crack. Despite the fact that the crack growth model does not account for the effect of the chemical environment explicitly, such observation is expected since (i) salt deposition parameters have a substantial influence on the time to crack initiation and (ii) the proposed functional form for the crack growth rate model proposed in (3.24). Here again, it should be noted that the proposed crack growth rate model in (3.24) does not account for the effect of the chemical environment at the crack tip.

The large number of impactful parameters indicates that submodel parameterization needs to be improved through additional information gathered of environmental conditions at the site and in the crack growth related material properties.

The top five parameters by *main effect*, account for 74 % of the variance, are:

1. Critical Stress Intensity factor for crack formation (K_{th})
2. Atmospheric Salt Concentration (s)
3. Parameterization of chloride particle size distribution $\left(k_\gamma, \theta_\gamma\right)$
4. Radial weld location
5. Axial WRS weight

Unlike the prior responses examined, the penetration time has a number of parameters that contribute a similar degree to explaining the variance in the response. Having a small sum of *main effects* indicates that the model is highly non-linear. Also, having the *total effects* similar in magnitude indicates that reducing the uncertainty in any of those parameters would contribute significantly to reducing the uncertainty of the ASCC model.

The value of the global sensitivity analysis for non-linear models originates in the ability of these techniques to decouple the influence that the value of other parameters have on a given parameter. The insight gained by the global sensitivity study, rather than inspecting the impact of varying individual parameters in an isolated manner, is illustrated by comparing the *main* and *total effects* of the radial weld location parameter. This is apparent in Table 5.2 as the effect of varying the radial weld position alone (its *main effect*) has a weak effect on any of the responses. However, as indicated by the *total effect* index, the interaction between the weld position and other parameters form a significant part of the variation of each response.

Table 5.2: The Sobol' indices for the *main* and *total effects* are presented for the time to crack initiation and the time to thru-wall crack propagation as reported by Dakota. The effects are expressed as a percentage for readability. Note that the *main effects* may not sum to 100% and the *total effect* for any parameter must be greater than the main effect.

Parameters	Penetration		Crack Initiation		Pit Initiation	
	Main Effect	Total Effect	Main Effect	Total Effect	Main Effect	Total Effect
Galvele [A/m]	0.65	12.59	0.00	12.14	0.00	0.00
R_{th} [%]	0.00	4.40	0.00	0.00	47.30	56.00
i_{rp} [A/m^2]	0.00	3.78	0.00	3.64	0.00	0.00
b [V_{SCE}/decade]	0.00	0.63	0.00	0.00	0.00	0.00
Salt Source [μg/m^3]	9.75	41.54	21.88	63.17	0.00	0.66
Radial Weld Location [–]	1.31	33.36	0.00	27.94	38.17	49.99
θ_γ [μm]	3.90	31.47	11.59	49.81	0.37	4.61
k_γ	1.95	20.14	3.86	35.23	0.52	0.82
K_{th} [MPa$\sqrt{m}$]	1.95	46.57	1.29	36.44	–	–
Rand. Axial WRS	1.30	23.29	1.29	4.86	–	–
Rand. Hoop WRS	0.65	3.78	0.00	6.07	–	–
y	2.60	14.47	0.00	3.64	–	–
$\ln(\alpha)$	0.65	17.62	–	–	–	–
$\ln(\dot{x}_{80^\circ C})$	0.65	9.44	–	–	–	–
β	0.00	3.15	–	–	–	–
Totals [%]	23.356	266.220	38.620	242.950	86.142	111.982

6 Site Selection and Ranking

A key milestone of this project is to evaluate and rank the ISFSIs based on the probability of SCC forming a canister wall penetrating crack. For the interim report, preliminary results are obtained that illustrate the analysis that the newly developed capability can produce.

6.1 Probabilistic Evaluation of Sites

The ASCC modeling capability has been exercised in a probabilistic manner to quantify the risk of corrosion pits initiating, cracks forming, or cracks penetrating the canister wall. This results presented in this section do not constitute a conclusive analysis as the uncertainty in many of the parameters is large and many site-specific factors governing salt deposition are not properly accounted for. The parameters chosen for the preliminary analysis (not including weather parameters) are provided in Table 6.1. The probabilistic analysis is carried out according to the procedure specified in Sec. 3.8. The results of the probabilistic analysis show substantial uncertainty in the time to penetration because of the correspondingly large uncertainty in the model parameters.

For the interim analysis, the quantitative results in Table 6.2 clearly show some interesting behaviors for the few sites analyzed. The preliminary analysis strongly suggests that vertical canisters are more resistant to SCC than horizontal ones; however, the model is currently lacking data regarding airflow (thus $u^\star$) around the canister so the results must be taken as preliminary but suggestive. The CDFs generated by the post-processing tool of the modeling capability produced Figs. 6.1 and 6.2. The CDFs show the minimum and maximum CDF resulting from a single epistemic run, along with the mean and the 5th and 95th percentiles for the probability of crack penetration. The potential enhanced ASCC resistance of the vertical canisters (Figs.6.1d–6.1f or Figs. 6.2d–6.2f) is evidenced by the reduced mean CDF compared to the horizontal canisters at the same site. The vertical canisters also result in cases where pits, cracks, or penetrations do not form after 100 years.

Table 6.1: Model parameters for probabilistic site assessment. The sampling distributions includes: constant $\mathscr{C}$; uniform $\mathscr{U}$; normal $\mathscr{N}$; lognormal $\ln\mathscr{N}$. The type of uncertainty is classified as: none (constant) $\mathscr{C}$; aleatoric A; epistemic E. The mean column contains the mean value for parameters described by a lognormal ($\ln\mathscr{N}$) or normal ($\mathscr{N}$) distribution, or the value if the value is a constant parameter. The minimum and maximum columns contain the limits for parameters described with a uniform distribution ($\mathscr{U}$)

	Type	Distribution	Mean	Std. Dev.	Min	Max
Geometry Parameters						
Diameter [m]		$\mathscr{C}$	1.710			
Length [m]		$\mathscr{C}$	4.400			
t [mm]		$\mathscr{C}$	16.000			
Longitudinal Weld Resolution		$\mathscr{C}$	7			
Radial Weld Resolution		$\mathscr{C}$	5			
Initial Decay Heat [kW]		$\mathscr{C}$	24.000			
Simulation Time [yr]		$\mathscr{C}$	150			
Time-Step [dy]		$\mathscr{C}$	0.500			
Epistemic Sample Size		$\mathscr{C}$	1			
Aleatoric Sample Size		$\mathscr{C}$	1			
Weld #1 Radial Loc.	E	$\mathscr{U}$			0.000	0.500
Weld #2 Radial Loc.	E	$\mathscr{U}$			0.000	0.500
Deposition Model Parameters						
d_{min} [μm]		$\mathscr{C}$	0.000			
d_{max} [μm]		$\mathscr{C}$	1000.000			
N_{bins}		$\mathscr{C}$	200.000			
ρ_{salt} [kg/m^3]		$\mathscr{C}$	2165.000			
Environment Salt Source Term						
$s^{\dagger}$ (Site Dependent, see Table 3.2)	E	$\mathscr{N}$			0.015	6.000
k_{γ} (Inland)	E	$\mathscr{U}$			2.133	4.694
θ_{γ} [μm] (Inland)	E	$\mathscr{U}$			0.565	104.248
k_{γ} (Coastal)	E	$\mathscr{U}$			2.290	4.694
θ_{γ} [μm] (Coastal)	E	$\mathscr{U}$			6.695	14.188

	Type	Distribution	Mean	Std. Dev.	Min	Max
		Cooling Tower Source Term				
$s\,[\mu\mathrm{g/m}^3]$	E	$\mathscr{U}$			12.430	18.820
k_γ	E	$\mathscr{U}$			2.198	31.873
$\theta_\gamma\,[\mu\mathrm{m}]$		$\mathscr{C}$	11.511			
		Road Salt Source Term				
$s\,[\mu\mathrm{g/m}^3]$	E	$\mathscr{U}$	1.71	0.307		
k_γ		$\mathscr{C}$	2.197			
$\theta_\gamma\,[\mu\mathrm{m}]$	E	$\mathscr{N}$	104.248			
		Pt Depth Model Parameters				
$(i_{\mathrm{rp}})_{\mathrm{ref}}\,[\mathrm{A/m}^2]$	A	$\mathscr{U}$			0.068	1.540
$b\,[\mathrm{V/decade}]$	A	$\mathscr{U}$			-0.169	-0.138
$E_{\mathrm{L}}\,[\mathrm{V}]$		$\mathscr{C}$	-0.200			
$\mathrm{R}_{\mathrm{th}}\,[\%]$	A	$\mathscr{U}$			15.000	30.000
Pit Stability Product [A/m]	A	$\mathscr{U}$			1.000	3.000
		Crack Initiation & Growth Model Parameters				
Hoop Stress Weight	A	$\mathscr{U}$			0.000	1.000
Axial Stress Weight	A	$\mathscr{U}$			0.000	1.000
Y	E	$\mathscr{U}$			0.900	1.100
$K_{\mathrm{th}}\,[\mathrm{MPa}\sqrt{\mathrm{m}}]$	A	$\mathscr{U}$			0.460	3.300
$\ln(\alpha)$	A	$\ln\mathscr{N}$	-25.921	1.570		
β	A	$\mathscr{N}$	0.500	0.200		
$\alpha-\beta$ correlation		$\mathscr{C}$	-0.470			
$\ln(\dot{x})_{80^\circ\mathrm{C}}$	A	$\ln\mathscr{N}$	-20.136	1.325		

[†] The salt source uncertainty based on CASTNET data that will vary by site.

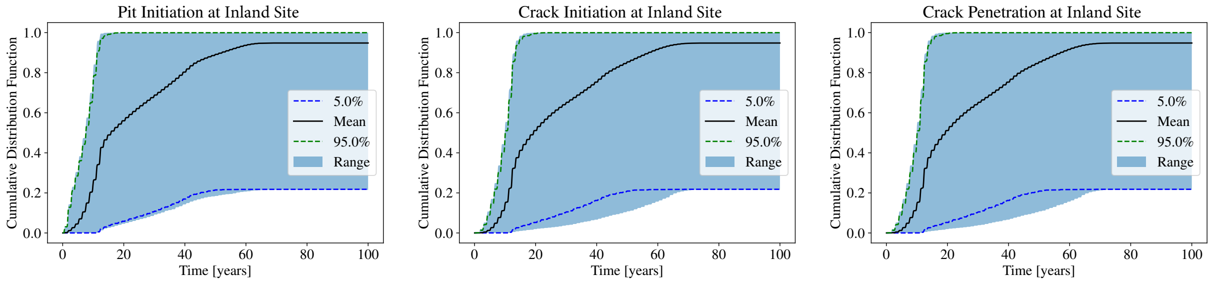

(a) Pit Initiation (H)

(b) Crack Initiation (H)

(c) Crack Penetration (H)

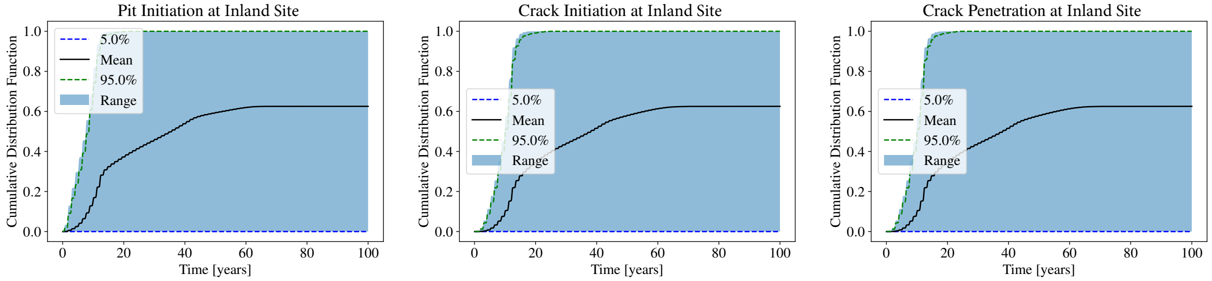

(d) Pit Initiation (V)

(e) Crack Initiation (V)

(f) Crack Penetration (V)

Figure 6.1: Cumulative distribution function (CDF) plots for horizontal (H) and vertical (V) canisters at a generic coastal ISFSI showing the mean, range, and the 5% and 95% confidence bounds for the three responses: (a/d) time to pit initiation, (b/e) time to crack initiation, and (c/f) time to crack penetration of canister wall.

Table 6.2: Summary crack penetration statistics for selected storage sites after 100 yrs. In addition to environmental sources, all sites may have additional salt sources which are limited to either a cooling tower (C) or deicing (road) salt (R).

Site	Orient	Addl. Sources	Mean	Percentile for failure		
				95 %	98 %	99 %
Inland	H	CR	0.948	1.000	1.000	1.000
Inland	V	CR	0.625	1.000	1.000	1.000
Coastal	H	C	0.998	1.000	1.000	1.000
Coastal	V	C	0.374	0.656	0.700	0.7315

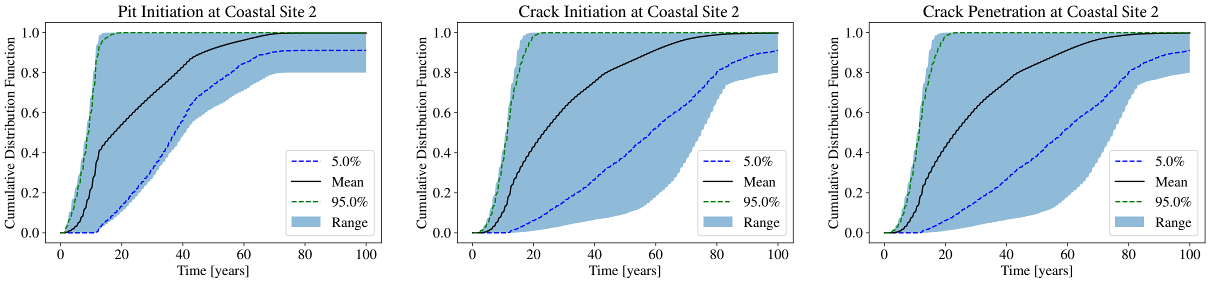

(a) Pit Initiation (H) (b) Crack Initiation (H) (c) Crack Penetration (H)

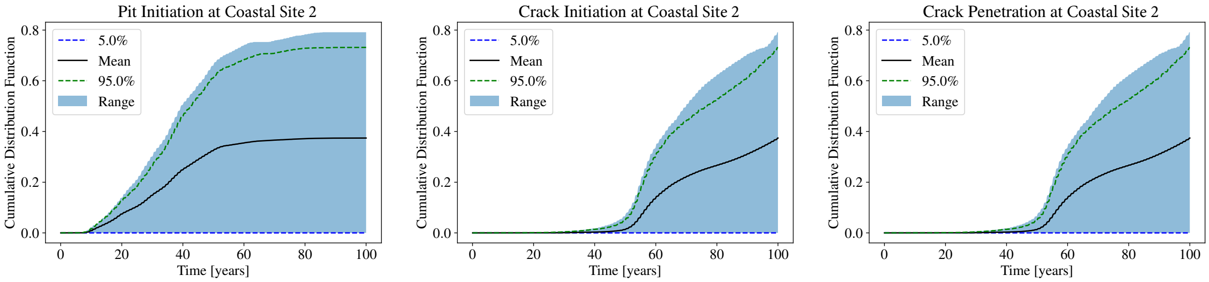

(d) Pit Initiation (V) (e) Crack Initiation (V) (f) Crack Penetration (V)

Figure 6.2: Cumulative distribution function (CDF) plots for horizontal (H) and vertical (V) canisters at a generic coastal ISFSI showing the mean, range, and the 5% and 95% confidence bounds for the three responses: (a/d) time to pit initiation, (b/e) time to crack initiation, and (c/f) time to crack penetration of canister wall.

7 Preliminary Guidance & Conclusions

This manuscript is an interim report describing the development, verification, and validation of a probabilistic atmospheric stress corrosion cracking modeling capability to asses the structural integrity of welded canisters for storage and transportation. This capability incorporates submodels for describing weather, salt deposition, electrochemical pitting, and residual stress driven crack propagation affecting weld lines. The origin of each submodel was presented and the technical basis for selecting realistic ranges for the submodel parameters was justified. The model was exercised in representative environments and service conditions for canisters stored at ISFSIs exposed to sea-salt aerosol particles.

The modeling capability developed accounts for variation in weather, the possibility of multiple aerosol salt sources, a detailed aerosol particle deposition model, and incorporates work sponsored by the SFWST program that provides detailed data on canister properties such as surface temperature, airflow, decay heat, and quantification of the WRS. The capability also provides a detailed deterministic pit depth model and WRS driven crack propagation model. The capability includes tools for executing large numbers of analysis runs on supercomputer infrastructure and processing the resulting data to generate probability distributions and summary statistics. Verification and validation has been conducted for each of the submodels to ensure that they are functionally consistent with the results of the pilot study and are able to be evaluated throughout the development process to ensure that each submodel functions properly.

This modeling capability is designed to reduce interim storage operational costs by identifying canister management data that is needed to develop risk-informed insights that can improve canister management. Methods and tools developed also consider how to use the results to assist in ranking major driving factors for ASCC for the extended storage of welded canisters. The methods and tools to be used to develop an optimized schedule for canister inspection and potential repairs for extended storage. For example, preliminary results indicate that the most immediate way to reduce risk of SCC is to ensure that welds are located on the lower half of the canister so as to reduce chloride deposition. Further investigations are warranted to provide definitive conclusions.

The interim results suggest that using the finding of Section 4.2, we can estimate an absolute lower bound for time until crack penetration by assuming large quantities of salt with the exact DD being irrelevant. This interim analysis has identified a distinct need to better understand the sources and amount of salt available in the atmosphere.

7.1 Data Needs

This work has identified a number of model parameters that are of critical importance to reducing the uncertainty in the ASCC model. A preliminary global sensitivity analysis conducted on this model results in important insights that could not be made from examining changes in individual parameters in isolation. The global sensitivity analysis identified the five most important parameters (ranked by the Sobol' total effect) governing the time to crack penetration include the following parameters that account for 74 % of the variance in the response:

1. Critical stress intensity factor for crack formation (K_{th})
2. Atmospheric salt concentration (s)
3. Parameterization of chloride particle size distribution $\left(k_\gamma, \theta_\gamma\right)$
4. Radial weld location
5. Axial WRS

These impactful parameters are recommended to be the focus of further data acquisition through experiments or existing literature. The condition for crack initiation, K_{th}, must be better predicted as it is a critical parameter for both initiation and thru-wall growth of cracks. K_{th} may remain highly uncertain as it may be governed by factors such as surface conditions, heat treatment, and the presence of impurities in the microstructure. Quantification and effect of those factors on the uncertainty (or reduction of) in K_{th}would be greatly beneficial. Even if it proves difficult to reduce the parameter's epistemic uncertainty, it is valuable to know that care must be used when selecting the range of values that this parameter could reasonably take. The present atmospheric stress corrosion cracking model as described in this manuscript has no mechanism for crack arrest once initiated. Therefore, it can be argued that the most important quantity is actually the time to crack initiation. The inevitable penetration of the canister can be halted if the canister surface is remediated before crack initiation. From this perspective the aerosol sea-salt concentration (s) (or more accurately: chloride concentration) becomes the dominant factor. Unfortunately, this quantity is difficult to predict as it can vary widely over the course of a year, or even a day, and can be affected by not only the proximity to the ocean [6, 16], conditions at the ocean surface, wind direction, and topography [3, 27], and also the presence of structures and vegetation, and removal by rain or entrainment [13]. The global sensitivity study results suggest that some of the more difficult parameters to measure (e.g., electrochemical ones such as Tafel slope b and the pit stability product, and mechanical ones such as weld residual stress, do not need to be known with more accuracy than currently available. This assumes that the uncertainty in those parameters are well characterized by the ranges specified in Table 5.1. However, as indicated by the preliminary global sensitivity study, reducing uncertainty in the chloride source concentration including a better accounting of road salt, cooling towers, and distance from the shore would improve the prediction of the current model. In addition, better accounting for the direction of prevailing winds from the shore, nearby roads, and cooling towers will help determine the total amount of salt that the canister is exposed to. Due to the known effects of local topography, structure, and plant life, there is a distinct need for more site specific measurements of source terms and particle size distributions, particularly near the ocean where atmospheric salt content is exceptionally high.

7.2 Follow-up work for next fiscal year

- Complete Monte Carlo data gathering for all remaining ISFSI sites;

- Perform site-ranking;
- Proposed optimized inspection per site category;
- Improve pitting model with more physical description of pit initiation and pit growth;
- Improved characterization of site-specific atmospheric conditions notably salt concentration and aerosol particle size distribution;
- Expand the analyses to other SS types beyond just 304;
- Explore much lower decay heats including zero decay heat;
- Relax assumptions of uniform distributions with better estimate distributions for some input parameters.

References

[1] R. Dingreville, C. J. Sallaberry, C. R. Bryan, C. Stockman, H. Adkins, and M. Sutton. Uncertainty quantification methodologies development for storage and transportation of used nuclear fuel: Pilot study on stress corrosion cracking of canister welds. OUO/ECI SAND2014-19467, Sandia National Laboraotires, Albuquerque, NM, November 2014.

[2] J. Alcántara, B. Chico, I. Díaz, D. de la Fuente, and M. Morcillo. Airborne chloride deposit and its effect on marine atmospheric corrosion of mild steel. *Corrosion Science*, 97:74–88, Aug 2015.

[3] I. S. Cole, W. D. Ganther, D. A. Paterson, G. A. King, S. A. Furman, and D. Lau. Holistic model for atmospheric corrosion: Part 2 – experimental measurement of deposition of marine salts in a number of long range studies. *Corrosion Engineering, Science and Technology*, 38 (4):259–266, Dec 2003.

[4] I. S. Cole, D. Lau, and D. A. Paterson. Holistic model for atmospheric corrosion part 6 – from wet aerosol to salt deposit. *Corrosion Engineering, Science and Technology*, 39(3):209–218, Sep 2004.

[5] F. Corvo, T. Perez, L. R. Dzib, Y. Martin, A. Castañeda, E. Gonzalez, and J. Perez. Outdoor–indoor corrosion of metals in tropical coastal atmospheres. *Corrosion Science*, 50(1):220–230, Jan 2008.

[6] Shengxi Li and L. H. Hihara. Aerosol salt particle deposition on metals exposed to marine environments: A study related to marine atmospheric corrosion. *Journal of The Electrochemical Society*, 161(5):C268–C275, April 2014.

[7] M. A. Mustafa and K. M. Yusof. Atmospheric chloride penetration into concrete in semitropical marine environment. *Cement and Concrete Research*, 24(4):661–670, 1994.

[8] E. Schindelholz, R.G. Kelly, I.S. Cole, W.D. Ganther, and T.H. Muster. Comparability and accuracy of time of wetness sensing methods relevant for atmospheric corrosion. *Corrosion Science*, 67:233–241, Feb 2013.

[9] I. Odnevall Wallinder, X. Zhang, S. Goidanich, N. Le Bozec, G. Herting, and C. Leygraf. Corrosion and runoff rates of Cu and three Cu-alloys in marine environments with increasing chloride deposition rate. *Science of The Total Environment*, 472:681–694, Feb 2014.

[10] V. N. Piskunov. Parameterization of aerosol dry deposition velocities onto smooth and rough surfaces. *Journal of Aerosol Science*, 40(8):664 – 679, 2009.

[11] A. C. K. Lai and W. W. Nazaroff. Supermicron particle deposition from turbulent chamber flow onto smooth and rough vertical surfaces. *Atmospheric Environment*, 39(27):4893–4900, Sep 2005.

[12] G. A. Sehmel. Particle eddy diffusivities and deposition velocities for isothermal flow and smooth surfaces. *Journal of Aerosol Science*, 4(2):125–138, Mar 1973.

[13] I. S. Cole and D. A. Paterson. Holistic model for atmospheric corrosion part 5 – factors controlling deposition of salt aerosol on candles, plates and buildings. *Corrosion Engineering, Science and Technology*, 39(2):125–130, Jun 2004.

[14] M. Wataru, H. Kato, S. Kudo, N. Oshima, K. Wada, and H. Narutaki. Measurement of atmospheric sea salt concentration in the dry storage facility of the spent nuclear fuel. In *International Conference on Nuclear Engineering*, volume Volume 1: Plant Operations, Maintenance and Life Cycle; Component Reliability and Materials Issues; Codes, Standards, Licensing and Regulatory Issues; Fuel Cycle and High Level Waste Management, pages 857–863. ASME, ASME, 2014.

[15] K. Fuhr, J. Broussard, and G. White. Suceptibility assesment criteria for cholirde-induced stress corrosion cracking (CISCC) of welded stainless steel canisters for dry cask storage systems. Technical Report 3002005371, EPRI, Palo Alto, CA, 2015.

[16] G. F. Rossknecht, W. P. Elliott, and F. L. Ramsey. The size distribution and inland penetration of sea-salt particles. *Journal of Applied Meteorology*, 12(5):825–830, Aug 1973.

[17] A. L. Williams and G. J. Stensland. Atmosphertic dispersion study of deicing salt applied to roads: Part II final report. Physical Research Report 149, Illinois Department of Transportation, Atmospheric Environment Section, Champaign, IL, January 2006.

[18] C. L. Alexander and E. J. Schindelholz. Cathodic kinetics on stainless steel in concentrated NaCl. *in preparation*, 2018.

[19] C. R. Bryan, E. J. Schindelholz, and C. Alexander. Physical and chemical properties of sea-salt deliquescent brines as a function of relative humidity. *submitted*, 2018.

[20] A. Anderko, N. Sridhar, and D. S. Dunn. A general model for the repassivation potential as a function of multiple aqueous solution species. *Corrosion Science*, 46(7):1583–1612, Jul 2004.

[21] C. R. Bryan and D. Enos. Summary of available data for estimating chloride-induced SCC crack growth rates for 304/316 stainless steel. Technical Report SAND2016-2992R, Sandia National Laboratories, Albuquerque, NM, March 2016.

[22] D. G. Enos and C. R. Bryan. Final report: Characterization of canister mockup weld residual stresses. Technical Report SAND2016-12375R, Sandia National Laboratories, United States, November 2016.

[23] R. M. Kain. Marine atmospheric stress corrosion cracking of austenitic stainless steels. *Materials Performance*, 29(12):60, 1990.

[24] P. R. Roberge, R. D. Klassen, and P. W. Haberecht. Atmospheric corrosivity modeling – A review. *Materials & Design*, 23(3):321–330, 2002.

[25] I. S. Cole, T. H. Muster, N. S. Azmat, M. S. Venkatraman, and A. Cook. Multiscale modelling of the corrosion of metals under atmospheric corrosion. *Electrochimica Acta*, 56(4):1856–1865, Jan 2011.

[26] D. R. Gunasegaram, M. S. Venkatraman, and I. S. Cole. Towards multiscale modelling of localised corrosion. *International Materials Reviews*, 59(2):84–114, 2014.

[27] L. Feng, H. Shen, Y. Zhu, H. Gao, and X. Yao. Insight into generation and evolution of sea-salt aerosols from field measurements in diversified marine and coastal atmospheres. *Scientific Reports*, 7:41260, Jan 2017.

[28] Alvin C. K. Lai and William W. Nazaroff. Modeling indoor particle deposition from turbulent flow onto smooth surfaces. *Journal of Aerosol Science*, 31(4):463–476, Apr 2000.

[29] M. R. Sippola and W. W. Nazaroff. Experiments measuring particle deposition from fully developed turbulent flow in ventilation ducts. *Aerosol Science and Technology*, 38(9):914–925, Sep 2004.

[30] B. Zhao and J. Wu. Modeling particle deposition from fully developed turbulent flow in ventilation duct. *Atmospheric Environment*, 40(3):457–466, Jan 2006.

[31] Tareq Hussein, Aleš Hruška, Pavla Dohányosová, Lucie Džumbová, Jiří Hemerka, Markku Kulmala, and Jiří Smolík. Deposition rates on smooth surfaces and coagulation of aerosol particles inside a test chamber. *Atmospheric Environment*, 43(4):905–914, Feb 2009.

[32] M. Janik-Czachor. An assessment of the processes leading to pit nucleation on iron. *Journal of the Electrochemical Society*, 128(12):513C–519C, 1981.

[33] J. R. Galvele. Pitting corrosion. *Treatise on Materials Science and Technology*, 23:1–57, 1983.

[34] L. F. Lin, C. Y. Chao, and D. D. Macdonald. A point defect model for anodic passive films: I. Film growth kinetics. *Journal of The Electrochemical Society*, 128(6):1187–1194, 1981.

[35] L. F. Lin, C. Y. Chao, and D. D. Macdonald. A point defect model for anodic passive films: II. Chemical breakdown and pit initiation. *Journal of The Electrochemical Society*, 128(6): 1194–1198, 1981.

[36] T. P. Hoar, D. C. Mears, and G. P. Rothwell. The relationships between anodic passivity, brightening and pitting. *Corrosion Science*, 5(4):279–289, 1965.

[37] K. E. Heusler and L. Fischer. Kinetics of pit initiation at passive iron. *Materials and Corrosion*, 27(8):551–556, 1976.

[38] A. A. Seys, M. J. Brabers, and A. A. Van Haute. Analysis of the influence of hydrogen on pitting corrosion and stress corrosion of austenitic stainless steel in chloride environment. *Corrosion*, 30(2):47–52, 1974.

[39] D. D. Macdonald and G. R. Engelhardt. Predictive modeling of corrosion. In Richardson J A, editor, *Shreir's Corrosion*, volume 2, pages 1630–1679. Elsevier, Amsterdam, 4 edition, 2010.

[40] B. Baroux. Kinetics of pit generation for stainless steels. In *Materials Science Forum*, volume 8, pages 91–104. Trans Tech Publ, 1986.

[41] A. Valor, F. Caleyo, L. Alfonso, D. Rivas, and J. M. Hallen. Stochastic modeling of pitting corrosion: a new model for initiation and growth of multiple corrosion pits. *Corrosion Science*, 49(2):559–579, 2007.

[42] J. L. Alamilla and E. Sosa. Stochastic modelling of corrosion damage propagation in active sites from field inspection data. *Corrosion Science*, 50(7):1811–1819, 2008.

[43] X.-Y. Zhang, S.-X. Li, R. Liang, and R. Akid. Effect of corrosion pits on fatigue life and crack initiation. In *13th International Conference on Fracture*, volume 1, pages 1667–1675, Red Hook, NY, 2013. International Conference on Fracture, Curran Associates, Inc.

[44] G. S. Frankel and N. Sridhar. Understanding localized corrosion. *Materials Today*, 11(10): 38–44, Oct 2008.

[45] G. Engelhardt, M. Urquidi-Macdonald, and D. D. Macdonald. A simplified method for estimating corrosion cavity growth rates. *Corrosion Science*, 39(3):419–441, 1997.

[46] G. Engelhardt and D. D. Macdonald. Unification of the deterministic and statistical approaches for predicting localized corrosion damage. I. Theoretical foundation. *Corrosion Science*, 46 (11):2755–2780, 2004.

[47] G. Engelhardt, D. D. Macdonald, Y. Zhang, and B. Dooley. Deterministic prediction of corrosion damage in low pressure steam turbines. *Power Plant Chemistry*, 6(6):647–661, 2004.

[48] A. Turnbull, L.N. McCartney, and S. Zhou. A model to predict the evolution of pitting corrosion and the pit-to-crack transition incorporating statistically distributed input parameters. *Corrosion Science*, 48(8):2084–2105, Aug 2006.

[49] Z. Y. Chen, F. Cui, and R. G. Kelly. Calculations of cathodic current delivery capacity and stability of crevice corrosion under atmospheric environments. *Journal of The Electrochemical Society*, 155(7):C360–C368, May 2008.

[50] Z. Y. Chen and R. G. Kelly. Computational modeling of bounding conditions for pit size on stainless steel in atmospheric environments. *Journal of The Electrochemical Society*, 157(2): C69, 2010.

[51] Y. Kondo. Prediction of fatigue crack initiation life based on pit growth. *CORROSION*, 45(1): 7–11, Jan 1989.

[52] A. Turnbull and S. Zhou. Pit to crack transition in stress corrosion cracking of a steam turbine disc steel. *Corrosion Science*, 46(5):1239–1264, May 2004.

[53] A. Turnbull. Corrosion pitting and environmentally assisted small crack growth. *Proceedings of the Royal Society A: Mathematical, Physical and Engineering Sciences*, 470(2169):20140254–20140254, 2014.

[54] D. De Meo, L. Russo, E. Oterkus, D. Gunasegaram, and I. Cole. Peridynamics for predicting pit-to-crack transition. *58th AIAA/ASCE/AHS/ASC Structures, Structural Dynamics, and Materials Conference*, 2017.

[55] P. Dong and F. W. Brust. Welding residual stresses and effects on fracture in pressure vessel and piping components: a millennium review and beyond. *Journal of Pressure Vessel Technology*, 122(3):329–338, 2000.

[56] B. Y. Fang, A. Atrens, J. Q. Wang, E.-H. Han, Z. Y. Zhu, and W. Ke. Review of stress corrosion cracking of pipeline steels in “low” and “high” pH solutions. *Journal of Materials Science*, 38 (1):127–132, 2003.

[57] F. W. Brust, D.-J. Shim, G. Wilkowski, and D. Rudland. PWSCC crack growth modeling approaches. In *ASME 2011 Pressure Vessels and Piping Conference*, pages 139–145. American Society of Mechanical Engineers, 2011.

[58] T. L. Anderson. *Fracture mechanics: fundamentals and applications*. CRC press, 2017.

[59] M. R. Hill, M. N. Tran, and J. E. Broussard. Validation approaches for weld residual stress simulation. In *ASME 2014 Pressure Vessels and Piping Conference*, pages V06BT06A068–V06BT06A068. American Society of Mechanical Engineers, 2014.

[60] M. Mayuzumi, J. Tani, and T. Arai. Chloride induced stress corrosion cracking of candidate canister materials for dry storage of spent fuel. *Nuclear Engineering and Design*, 238(5): 1227–1232, May 2008.

[61] I. M. Sobol’. Global sensitivity indices for nonlinear mathematical models and their monte carlo estimates. *Mathematics and Computers in Simulation*, 55(1-3):271–280, Feb 2001.

[62] A. Saltelli, M. Ratto, T. Andres, F. Campolongo, J. Cariboni, D. Gatelli, M. Saisana, and S. Tarantola. *Global Sensitivity Analysis. The Primer*, chapter 4, pages 53–107. John Wiley & Sons, Ltd, Chichester, West Sussex, England, January 2008.

[63] B. M. Adams, K. R. Dalbey, M. S. Eldred, D. M. Gay, L. P. Swiler, W. J. Bohnhoff, J. P. Eddy, and K. Haskell. DAKOTA, a multilevel parallel object-oriented framework for design optimization, parameter estimation, uncertainty quantification, and sensitivity analysis. Technical Report SAND2014-4633, Sandia National Laboratories, Albuquerque, NM, 2014.

[64] U.S. Environmental Protection Agency Clean Air Markets Division. Clean air status and trends network (CASTNET).

[65] E. A. Davis. Environmental assesment of chalk point cooling tower drift and vapor emissions. Technical Report JHU PPSP-CPCTP-28, The Johns Hopkins Applied Physics Laboratory, Laurel, Maryland, March 1979.

[66] M. L. Moon. Environmental impact of salt drift from a natural draft cooling tower. *Johns Hopkins APL Technical Digest*, 1(2):120–128, April-June 1980.

[67] W. J. Pardue. Official exhibit PEF606-00-BD01: Crystal river salt drift study, permit number PSD-FL-007, annual report for 1993–1994 (KBN engineering). Exhibit NRC ADAMS Accession No. ML12325A105, Florida Power Corporation, St. Petersburg, FL, May 1995.

[68] NRC. Indian Point unit No. 3, final environmental statement on the preferred closed cycle cooling. Draft Environmental Statement NUREG-0574, U.S. Nuclear Regulatory Commission, August 1977.

[69] S. R. Suffield, J. A. Fort, H. E. Adkins, J. M. Cuta, B. A. Collins, and E. R. Siciliano. Thermal modeling of NUHOMS HSM-15 and HSM-1 storage modules at calvert cliffs nuclear power station ISFSI. Technical Report PNNL-21788, Pacific Northwest National Laboratory, Richland, Washington, 10 2012.

[70] J. M. Cuta and H. E. Adkins. Preliminary thermal modeling of HI-STORM 100 storage modules at diablo caynon power plant ISFSI. Technical Report FCRD-UFD-2014-000505, U.S. Department of Energy, Used Fuel Disposition Campaign, Washington, DC, April 2014.

[71] I. C. Gauld, S. M. Bowman, and J. E. Horwedel. ORIGEN-ARP: Automatic rapid processing for spent fuel depletion, decay, and source term analysis. Technical Report ORNL/TM-2005/39, Oak Ridge National Laboratory, Oak Ridge, Tennessee, 2009.

[72] W. Lv, C. Pan, W. Su, Z. Wang, S. Liu, and C. Wang. Atmospheric corrosion mechanism of 316 stainless steel in simulated marine atmosphere. *Corrosion Engineering, Science and Technology*, 51(3):155–162, 2016.

[73] J. Kusnick, M. Benson, and S. Lyons. Finite element analysis of weld residual stresses in austenitic stainless steel dry cask storage system canisters. Technical letter report, U.S. Nuclear Regulatory Commission, December 2013.

[74] D. G. Enos, C. R. Bryan, and K. M. Norman. Data report on corrosion testing of stainless steel SNF storage canisters. Technical Report SAND2013-8314P, Sandia National Laboraotires, Albuquerque, NM, September 2013.

[75] J. C. Farmer, R. D. McCright, J. S. Huang, A. Roy, K. Wilfinger, R. Hopper, F. Wang, P. Bedrossian, J. Estill, and J. Horn. Development of integrated mechanistically-based degradation-mode models for performance assessment of high-level waste containers. Technical Report UCRL-ID-130811 Rev. 1, Lawrence Livermore National Laboratory, Livermore, CA, June 1999.

[76] NRC. Identification and prioritization of the technical information needs affecting potential regulation of extended storage and transportation of spent nuclear fuel. Technical Report Draft report for comment ML120580143, U.S. Nuclear Regulatory Commission, Washington, D.C., 2012.

[77] G. Nakayama and Y. Sakakibara. Prediction model for atmospheric stress corrosion cracking of stainless steel. *ECS Transactions*, 50(31):303–311, May 2013. ISSN 1938-5862. doi: 10.1149/05031.0303ecst.

[78] H. S. Khatak, J. B. Gnanamoorthy, and P. Rodriguez. Studies on the influence of metallurgical variables on the stress corrosion behavior of aisi 304 stainless steel in sodium chloride solution using the fracture mechanics approach. *Metallurgical and Materials Transactions A*, 27(5): 1313–1325, May 1996. ISSN 1543-1940. doi: 10.1007/bf02649868.

[79] R. Parrott and H. Pitts. Chloride stress corrosion cracking in austenitic stainless steel: Assessing susceptibility and structural integrity. Technical Report RR902, U.K. Health and Safety Executive, Harpur Hill, Buxton, Derbyshire, 2011.

[80] J. M. Creer, T. E. Michener, M. A. McKinnon, J. E. Tanner, E. R. Gilbert, and R. L. Goodman. The TN-24P PWR spent fuel storage cask: Testing and analyses. Technical Report EPRI NP-5128/PNL-6054, Pacific Northwest National Laboratory, Richland, Washington, 1987.

[81] M. A. McKinnon, J. W. Doman, J. E. Tanner, R. J. Guenther, J. M. Creer, and C. E. King. BWR spent fuel storage cask performance test. Volume I: Cask handling experience and decay heat, heat transfer, and shielding data. Volume II: Pre- and post-test decay heat, heat transfer, and shielding analyses. Technical Report PNL-5577, Pacific Northwest National Laboratory, Richland, WA, 1986.

[82] M A McKinnon, T E Michener, M F Jensen, and G R Goodman. Testing and analyses of the TN-24P PWR spent-fuel dry storage cask loaded with consolidated fuel. Technical Report EPRI NP 6191/PNL-6631, Idaho National Engineering Laboratory and Pacific Northwest Laboratory and EG&G Idaho, Idaho Falls, ID and Richland, WA, 1989.

[83] D. R. Rector, R. A. McCann, U. P. Jenquin, C. M. Heeb, J. M. Creer, and C. L. Wheeler. CASTOR-1C spent fuel storage cask decay heat, heat transfer, and shielding analyses. Technical Report PNL-5974, Pacific Northwest Laboratory, Richland, WA, 1986.

[84] C. Norberg and B. Sunden. Turbulence and reynolds number effects on the flow and fluid forces on a single cylinder in cross flow. *Journal of Fluids and Structures*, 1(3):337–357, Jul 1987.

[85] H. G. Dimopoulos and T. J. Hanratty. Velocity gradients at the wall for flow around a cylinder for reynolds numbers between 60 and 360. *Journal of Fluid Mechanics*, 33(02):303, Aug 1968.

[86] A. Eldering, P. A. Solomon, L. G. Salmon, T. Fall, and G. R. Cass. Hydrochloric acid: A regional perspective on concentrations and formation in the atmosphere of southern california. *Atmospheric Environment. Part A. General Topics*, 25(10):2091–2102, Jan 1991.

[87] I. J. Hindawi, L. C. Raniere, and J. A. Rea. Ecological effects of aerosol drift from a saltwater cooling system. Technical Report EPA-600/3-76-078, U.S. Department of Environmental Protection, Terrestrial Ecology Branch, Corvallis, Oregon, July 1976.

[88] A. L. Williams, G. J Stensland, C. R. Peters, and J. Osborne. Atmospheric dispersion study of deicing salt applied to roads: First progress report. Contract Report 2000-05, Illinois State Water Survey, Atmospheric Environment Section, Champaign, IL, April 2000.

[89] J. R. Galvele. Transport processes in passivity breakdown – II. full hydrolosis of the metal ions. *Corrosion Science*, 21(8):551–579, 1981.

[90] M. T. Woldemedhin, J. Srinivasan, and R. G. Kelly. Effects of environmental factors on key kinetic parameters relevant to pitting corrosion. *Journal of Solid State Electrochemistry*, 19 (12):3449–3461, Mar 2015.

[91] M. H. Moayed and R. C. Newman. The relationship between pit chemistry and pit geometry near the critical pitting temperature. *Journal of The Electrochemical Society*, 153(8):B330, 2006.

[92] S. Shoji, N. Ohnaka, Y. Furutani, and T. Saito. Effects of relative humidity on atmospheric stress corrosion cracking of stainless steels. *Corrosion Eningeering*, 35(10):559–565, 1986.

[93] Toshimitsu Homma and Andrea Saltelli. Importance measures in global sensitivity analysis of nonlinear models. *Reliability Engineering & System Safety*, 52(1):1–17, Apr 1996.

[94] A. Saltelli, P. Annoni, I. Azzini, F. Campolongo, M. Ratto, and S. Tarantola. Variance based sensitivity analysis of model output. design and estimator for the total sensitivity index. *Computer Physics Communications*, 181(2):259–270, Feb 2010.

[95] W. Wagner and A. Pruß. The IAPWS formulation 1995 for the thermodynamic properties of ordinary water substance for general and scientific use. *Journal of Physical and Chemical Reference Data*, 31(2):387–535, Jun 2002.

Appendix A Code Description

The code has a number of modes and built in features to make applying it more straightforward and analysis simplified. The major features are:

Complete documentation of all functions and modules via Doxygen that is available in the `Documentation` folder or through the links `Documentation HTML` or `Documentation PDF`, for HTML or PDF forms of documentation.

Dakota interface with a Dakota input file that will perform a sensitivity study that is available in `scc/unit_test_files/sensitivity_study/`

A.1 Conducting a Probabilistic Analysis via Monte Carlo Sampling

A.1.1 Pre-processing

The `tool/launch-scc.py` script has been developed to aid in launching a large number of analysis runs in an efficient manner on large supercomupters. The purpose of the code is to execute one (or more) epistemic runs on a single compute node and run a large number of aleatoric sampling runs on each node. The script calculate the time needed to perform the calculation based on the user specified `--time_per_realization` option that should be set to the number of seconds to complete a single aleatory sampling run.

```
    usage: launch-scc.py [-h] -s {d,g,r,e,c,u,m,s,l} -e EPISTEMIC [-n N] -a
                     ALEATORIC [-c CORES] [-r RAND] -l LOCATION -o {v,h}
                     [-q {batch,short}] [-t RUNTIME] [-w WCID]
                     [--time_per_realization TIME_PER_REALIZATION] [-v]
```

```
Launches multiple SCC code instances on one or more nodes on various computer
systems

optional arguments:
  -h, --help            show this help message and exit
  -s {d,g,r,e,c,u,m,s,l}
                        Computer system: 'd'=direct run, 'c'=chama, 'g'=ghost,
                        'u'=uno, 'r'= serrano, 'e'=eclipse,
                        's'=skybridge,'m'=my mac,'l'=s1006792
  -e EPISTEMIC, --epistemic EPISTEMIC
```

```
                        number of epistemic instances
  -n N, --n N           number of epistemic instances for each execution of
                        scc code (optional) [default 1]
  -a ALEATORIC, --aleatoric ALEATORIC
                        number of aleatoric instances per epistemic instance
  -c CORES, --cores CORES
                        number of cores to use (optional)
  -r RAND, --rand RAND  Random number generator seed [default 0: if <= 0, then
                        clock is used to pick new seed]
  -l LOCATION, --location LOCATION
                        Name of ISFSI site [i.e. 'ComanchePeak']
  -o {v,h}, --orientation {v,h}
                        Orientation of canisters at ISFSI site (h or v)
  -q {batch,short}, --queue {batch,short}
                        Queue to employ (optional, default batch)
  -t RUNTIME, --runtime RUNTIME
                        Run Time (optional, default 48:00:00)
  -w WCID, --wcid WCID  WCID for use on Sandia Clusters(optional)
  --time_per_realization TIME_PER_REALIZATION
                        Time for a single aleatoric instance to complete [s],
                        this is a system dependent value so it should be reset
                        for each system the SCC code is used with.
  -v, --verb            Use verbose output? May generate HUGE files
```

A.1.2 Post-processing

The folder `scc/tools/` folder contains tools need to launch analysis jobs and post-process the results.

A.2 Required Inputs

The SCC code uses three different kind of input file to parameterize the execute the model. The first is a global parameter file that sets parameters that apply to all sites and controls the model execution; second is the site-dependent parameters that includes weather and salt deposition parameters; third are the databases that contain experimental or calculated data related to the properties of the brine solution, canister temperature, and weld residual stress.

The structure of the input files is very straight-forward. The code expects FORTRAN *namelist* style input. Begin all global parameter input using the template `SCC_Parameters.nml`, and the site-specific parameters should be entered based on one of the files provided in `All_Sites_Data/`.

A.2.1 Input Parameter Types

The SCC code has a number of different input types that will be referred to in the following discussion of inputs to the code. As the code is written in FORTRAN, the language's limitations must be respected in providing data. The types of inputs expected (and their short-hand notation) include:

Logical (L) A boolean logical True/False variable. In FORTRAN-style, this may be written as: `.true.` or `.false.`; 1 or 0; `T` or `F`.

String (S) A sequence of characters (without spaces) that must be quoted.

Integer (I) An integer.

Float (F) A double precision floating point number. This may be given in the form of `0.00`, `0.00e0`, or `0.00d0` (preferred).

Uncertain (U) Data that represents either a constant or can be represented by a statistical distribution. Distributions include: Constant ($\mathscr{C}$), Uniform ($\mathscr{U}$), log normal (ln$\mathscr{N}$), and normal ($\mathscr{N}$) distributions. Each uncertain variable is classified having either aleatoric or epistemic uncertainty.

The code expects each value (L,S,I,F) or set of values to be identified by a comment line and the value on the following line. In the case of the U variable type, the code expects the input to be provided on two lines; the first line identifying the type of distribution, and the second providing the necessary inputs. The distribution type can take the values 0, 1, 2, or 3, corresponding to a constant value, uniform ($\mathscr{U}$), normal ($\mathscr{N}$), or a log normal (ln$\mathscr{N}$) distribution. The U variable type is entered in one of the following 2-line forms: For a $\mathscr{C}$ (constant) value (type 0):

```
var%TYPE_FLAG = 0, ! comment
var%VALUE = X,
```

Provide with a single floating point value. For a $\mathscr{U}$ distribution (type 1):

```
var%TYPE_FLAG = 1,
var%EPISTEMIC_FLAG = T/F,
var%MINIMUM = X,
var%MAXIMUM = X,
```

The `TYPE_FLAG` is a boolean variable that identifies the U variable `var` as either having epistemic (T) or aleatoric (F) uncertainty. The values `minimum` and `MAXIMUM` are floating point values that specify the limits of the distribution. For a $\mathscr{N}$ distribution (type 2):

```
var%TYPE_FLAG = 2,
var%EPISTEMIC_FLAG = T/F,
var%MEAN = X,
var%STANDARD_DEV = X,
var%TRUNCATION = X,
```

The `FLAG` is a boolean variable that identifies the U variable `var` as either having epistemic (T) or aleatoric (F) uncertainty. The values `MEAN` and `STANDARD_DEVIATION` are floating point values that specify the mean and standard deviation of the $\mathscr{N}$ distribution. `TRUNCATION` specifies the smallest non-zero value used to generate a value in the distribution. Use this to prevent the generation of extreme outlying statistical samples. For a $\ln\mathscr{N}$ distribution (type 3):

```
var%TYPE_FLAG = 3,
var%EPISTEMIC_FLAG = T/F,
var%MEAN = X,
var%STANDARD_DEV = X,
var%TRUNCATION = X,
```

The `FLAG` is a boolean variable that identifies the U variable `var` as either having epistemic (T) or aleatoric (F) uncertainty. The values `MEAN` and `STANDARD_DEVIATION` are floating point values that specify the mean and standard deviation of the $\ln\mathscr{N}$ distribution. Note that these values are expected to be the natural logarithm of the actual values. `TRUNCATION` specifies the smallest non-zero value used to generate a value in the distribution (not the natural logarithm of the value). Use this to prevent the generation of extreme outlying statistical samples.

A.2.2 Global Parameters

The parameters required in the global input file `SCC_Parameters.nml` are listed below with a description of the parameters and their type identification as listed in Section A.2.1. Because a variable is listed as a U, it does not mean that the parameter must be treated as uncertain. U parameters can be set constant by declaring them of type 0.

Namelist: `CONTROL` contains parameters to control the model

`silent` **(L)** [T/F] If silent is false, a limited amount of information is printed to the screen during model execution and other information is saved to files within the generated `Output/` directory. The screen will report the current time step during execution. Additional files output are described in Section A.3. Information output includes annual summaries of maximum pit and crack depth, and salt deposition densities.

`debug` **(L)** [T/F] Prints a large amount of information to the screen for debugging purposes. Data reported includes detailed records of the convergence of root-finding algorithms and daily values of weather, pit, and maximum crack depth. It is recommended to use this option only for very short simulation time periods to aid in debugging due to the large amount of data reported.

`dakota_output` **(L)** [T/F] Enable code to output file for Dakota to read for use in performing sensitivity studies.

`dump_interval` **(I)** [dy] Frequency with which to output deposition and pit depth data.

`simulation_name` **(S)**

`epistemic_samples` **(I)** $[-]$ Number of epistemic samples to generate, where uncertain variables marked as having epistemic uncertainty will be resampled after each model execution.

`aleatory_samples` **(I)** [−] Number of aleatoric samples to generate, with each sample constituting a unique sampling of variables marked as having aleatoric uncertainty. The requested number of samples are executed for each epistemic sample requested.

`random_seed_value` **(I)** [−] This allows for the specification of the random seed used to initialize the weather and uncertain parameter sampling. This parameter is intended for use in testing or calibration where identical weather parameters and samples are needed each time the code is run. A value of 0 will ensure that a unique seed (based on the system clock time) is used to generate random samples.

`stat_bins` **(I)** [−] Number of bins to use in the calculation of the CDF generated in post-processing after the requested number of aleatoric runs have been completed.

`longitudinal_weld_resolution` **(I)** [−] Number of increments for each longitudinal weld that extends for half of the canister length.

`radial_weld_resolution` **(I)** [−] Number of increments for each radial weld that extends half-way around the canister (weld is symmetric about the the circumference).

`epistemic_start` **(I)** [−] (Default: 1) Number to label first epistemic evaluation. This is useful for restarting an incomplete analysis, which occurs if the value is ≥ 1. A value of ≤ 0 ensures that the evaluations are started from the first epistemic and aleatoric instance (i.e. from scratch).

Namelist: `CANISTER` contains parameters for canister geometry and modeled time

`weld_1_location` **(U)** [−] Weld #1 normalized radial location, where 0 is the underside of canister (for horizontal canisters) and 0.5 indicates the weld is located at the top of the canister.

`weld_2_location` **(U)** [−] Weld #2 normalized radial location, where 0 is the underside of canister (for horizontal canisters) and 0.5 indicates the weld is located at the top of the canister.

`initial_decay_heat` **(U)** [kW] Initial decay heat given off by canister.

`simulation_time` **(U)** [years] Time for which to run the model for each epistemic and aleatoric iteration.

`time_step` **(U)** [days] Currently fixed at one day.

`canister_diameter` **(U)** [m] Outer diameter of canister.

`canister_length` **(U)** [m] Length of canister in longitudinal direction.

`canister_thickness` **(U)** [m] Thickness of canister walls.

Namelist: `CRACK` contains parameters used in the crack growth model

`random_hoop` **(U)** [−] Determines the degree to which hoop WRS represents the WC residual stress. A weight of 0 selects the residual stress in the HAZ and 1 selects the residual stress at the WC. Intermediate values are linearly interpolated.

`random_axial` **(U)** [−] Determines the degree to which the axial WRS represents the WC residual stress. A weight of 0 selects the residual stress in the HAZ and 1 selects the residual stress at the WC. Intermediate values are linearly interpolated.

`geom_factor` **(U)** $[-]$ The geometric factor (aspect ratio) Y in (3.23).

`K_th` **(U)** $[\mathrm{MPa}/\sqrt{\mathrm{m}}]$ Threshold stress intensity factor for crack growth.

`crack_growth_rate_80C` **(U)** $[\ln \mathrm{m/s}]$ Natural logarithm of the rate of crack growth at **80°C** at a reference temperature of 80°C.

`beta` **(U)** $[-]$ Stress-intensity factor exponent for crack growth.

`alpha` **(U)** $[\mathrm{m/s}]$ Crack growth prefactor.

`alpha_beta_correlation` **(U)** $[-]$ Correlation between crack growth parameters.

`T_ref_crack_growth` **(U)** [°C] Ambient environmental temperature at which canister temperature tables were calculated (currently 15.555°C). Should be set as a constant (type 0).

Namelist: `CORROSION` Contains parameters needed for the maximum pit depth model.

`threshold_RH` **(U)** [%] The minimum RH required to initiate pit growth

`i_rp_ref` **(U)** $[\mathrm{A/m^2}]$ Value of passive current density corresponding to given Tafel slope, E_L, and reference E_{rp} values.

`E_rp_ref` **(U)** $[\mathrm{V_{SCE}}]$ Value of repassivation potential corresponding to given Tafel slope, E_L, and reference i_{rp} value.

`tafel` **(U)** $[\mathrm{V_{SCE}}/\mathrm{decade}]$ The Tafel slope corresponding to the given E_L, and reference i_{rp} and E_{rp} values.

`E_L` **(U)** $[\mathrm{V_{SCE}}]$ Value of corrosion potential corresponding to given Tafel slope and reference i_{rp} and E_{rp} values.

`E_rp_min` **(U)** $[\mathrm{V_{SCE}}]$ Minimum possible value of E_{rp} for use in root-finding algorithms.

`galvele` **(U)** [A/m] Pit stability product for corrosion.

`particle_density` **(U)** $[\mathrm{kg/m^3}]$ Density of airborne salt particles. Defaults to the density of NaCl at $2160\,\mathrm{kg/m^3}$.

Namelist: `INPUT` `site_file_name` **(S)** (Default: `Sites.txt`)

`sites_folder` **(S)** (Default: `All_Sites_Data`)

Namelist: `DATABASES` `axial_file_name` **(2D)** (Default: `axial_stress.dat`) Stores the experimental data for the axial residual stress near the welds in MPa. The data is stored by normalized depth from the outer diameter of the canister (rows) and the value of stress in the HAZ or WC (columns). The stress values are extracted from Ref. [22], subject to the simplifications discussed in Section 3.7.2.

`hoop_file_name` **(2D)** (Default: `hoop_stress.dat`) Stores the experimental data for the hoop residual stress near the welds in MPa. The data is stored by normalized depth from the outer diameter of the canister (rows) and the value of stress in the HAZ or WC (columns). The stress values are extracted from Ref. [22], subject to the simplifications discussed in Section 3.7.2.

`steam_file_name` **(3D)** (Default: `Vertical_Temp.dat`) Temperature map in degrees Celcius for the vertical canister. The data is stored by normalized length along the longitudinal axis (rows), the radial position from 0 at 0 deg to 0.5 at 180 deg (columns), with the 3^{rd} dimension being the time (in years) from the reference decay heat load (in this case 24 kW). The temperature values were extracted from Ref. [70].

`press_file_name` **(2D)** (Default: `PsatvsT.dat`) The saturation pressure is needed for calculations involving RH. The database provides Saturation Pressure in MPa as a function of temperature in degrees Celsius. At temperatures below zero, the saturation pressure is referenced to being over ice, not liquid water. The database is derived from the functional forms of Ref. [95].

`volume_file_name` **(1D)** (Default: `VolvsPsat.dat`) Provides the volume density of liquid water in m^3/kg as a function of pressure in MPa. At temperatures below zero, the saturation pressure is referenced to being over ice, not liquid water. The database is derived from the functional forms of Ref. 95.

`horizontal_file_name` **(3D)** (Default: `Horizontal_Temp.dat`) Temperature map in degrees Celsius for the horizontal canister. The data is stored by normalized length along the longitudinal axis (rows), the radial position from 0 at the underside of the canister to 0.5 at the top surface (columns), with the 3^{rd} dimension being the time (in years) from the reference decay heat load (in this case 24 kW). The temperature values were extracted from Ref. 69.

`vertical_file_name` **(3D)** (Default: `Vertical_Temp.dat`) Temperature map in degrees Celsius for the vertical canister. The data is stored by normalized length along the longitudinal axis (rows), the radial position from 0 at the underside of the canister to 0.5 at the top surface (columns), with the 3^{rd} dimension being the time (in years) from the reference decay heat load (in this case 30.17 kW). The temperature values were extracted from Ref. 70.

`decay_heat_horizontal_file_name` **(1D)** (Default: `Decay_Heat_Horizontal.dat`) Decay heat (kW) versus time (in years) for the horizontal canister that was used to generate the horizontal temperature map in the `Horizontal_Temp.dat` file.

`decay_heat_vertical_file_name` **(1D)** (Default: `Decay_Heat_Vertical.dat`) Decay heat (kW) versus time (in years) for the vertical canister that was used to generate the vertical temperature map in the `Vertical_Temp.dat` file.

`horizontal_Cf_file_name` **(2D)** (Default: `Cf_Horizontal.dat`)

`horizontal_ustar_file_name` **(2D)** (Default: `Horizontal_ustar.dat`) If present, the $u^\star$ file will be used for horizontal canisters.

`vertical_ustar_file_name` **(2D)** (Default: `Vertical_ustar.dat`) If present, the $u^\star$ file will be used for vertical canisters, otherwise flat plate friction is assumed.

`cond_file_name` **(2D)** (Default: `Canthodic_conductivity.dat`) Provides the conductivity of the brine solution in units of S/m. The data is given in terms of RH [%] (rows), and temperature in degrees Celsius (columns). The database is extracted from the results reported in Ref. [19].

`brine_thickness_file_name` **(2D)** (Default: `Brine_Thickness.dat`) Provides the thickness of the Brine layer in meters as a function of the density in $\mathrm{kg/m^2}$. The data is stored by RH [%] (rows), and temperature in degrees Celsius (columns). The database is extracted from the results reported in Ref. [19].

`air_dens_file_name` **(1D)** (Default: `AirDensvsT.dat`) Provides the density of air as a function of temperature $\mathrm{kg/m^3}$.

`brine_ph_file_name` **(2D)** (Default: `Brine_pH.dat`) Provides pH of the brine layer as a function of RH and temperature. The data is stored by RH [%] (rows), and temperature in degrees Celsius (columns). The database is extracted from the results reported in Ref. [19].

`cl_concentration_file_name` **(2D)** (Default: `Brine_Cl_concentration.dat`) Provides the chloride ion molar concentration in the brine layer. The data is stored by RH [%] (rows), and temperature in degrees Celsius (columns). The database is extracted from the results reported in Ref. [19].

Namelist: `OUTPUT` `error_report_file_name` **(S)** (Default: `Outputs/ERROR_REPORT.txt`) Use to record errors, warnings, and notes.

`output_directory` **(S)** (Default: `Outputs`) This directory determines the file location prefix for the remaining output files listed below:

`results_file_name` **(S)** (Default: `results_summary.out`)

`site_statistics_file_name` **(S)** (Default: `site_statistics.dat`)

`pits_out_file_name` **(S)** (Default: `pits.dat`) Output file for pit data.

`cracks_out_file_name` **(S)** (Default: `cracks.dat`) Output file for crack data.

`weather_out_file_name` **(S)** (Default: `weather.dat`) Reports the daily weather generated for a given site including the maximum and minimum temperature [°C], RH [%], and dewpoint [°C].

`time_record_file_name` **(S)** (Default: `first_event_record.dat`) A file reporting the first time of pit initiation, the first crack initiation, and the first penetration of the canister for each epistemic and aleatoric instance. These times are independent, meaning that they do not necessarily refer to the same pit. The data is unsorted. This file is intended for use in post-processing to extract statistics. Time is reported in days, where a -1 value means the event did not occur.

`twc_summary_file_name` **(S)** (Default: `first_twc.dat`) Lists the location (coordinates, and weld), pit initiation time, crack initiation time, penetration time, and elapsed time for crack growth for the first crack that penetrates the wall in each aleatoric evaluation for all epistemic evalutions. Time is given in days, the weld number in which the crack is located, the normalized canister surface coordinates, and the crack's final depth is reported in mm.

A.2.3 Site-dependent Parameters

The parameters required each site parameter file, found within the `All_Sites_Data/` directory, are listed below with a description of the parameters and their type identification as listed in

Section A.2.1. Because a variable is listed as a U, it does not mean that the parameter must be treated as uncertain. U parameters can be set constant by declaring them of type 0.

Namelist: `MAXTEMP` Max Temperature Reference parameters are used in (3.1):

`a` **(F)** y scale

`b` **(F)** y shift

`c` **(F)** x scale

`d` **(F)** x shift

Namelist: `MAXTEMPSTD` Maximum Temperature Standard Deviation parameters are used in (3.2):

`a` **(F)** y scale

`b` **(F)** y shift

`c` **(F)** x scale

`d` **(F)** x shift

Namelist: `MINTEMP` Minimum Temperature Fitting from Max Temperature parameters are used in (3.4):

`mean` **(F)** mean

`standard_dev` **(F)** standard deviation

Namelist: `MAXDEW` Max Dew Point Fitting from Max Temperature parameters are used in (3.5):

`mean` **(F)** mean

`standard_dev`**(F)** standard deviation

Namelist: `MINDEW` Minimum Dew Point Fitting from Max Dew Point] Parameters are used in (3.6):

`mean` **(F)** mean of the logarithm tranformed

`standard_dev` **(F)** standard deviation of the logarithm transformed

Namelist: `PSD` particle size distribution namelist

`d_min` **(F)** $0\,\mu$m Minimum airborne salt particle size

`d_max` **(F)** $1000\,\mu$m Maximum airborne salt particle size

`nbins` **(I)** $200\,[-]$ Number of bins to use for discretization of particle size distribution.

Namelist: `ORIENT` Specifies the orientation fo the canister

`horizontal` **(L)** (Default: T) Specifies if the canister is in a horizontal orientation. The parameter is True if the canister is in the horizontal orientation.

Namelist: `WIND` Specifies the far-field air flow rate within the canister overpack `wind_velocity` **(U)** U_∞ [m/s] If the horizontal or vertical $u^\star$ tables are not being used, the velocity is needed to estimate the surface friction velocity using the C_f tables.

Namelist: `NSOURCE` Number of salt sources namelist

`nsources` **(I)** $[-]$ Number of independent sources of airborne salt particles (no limit).

Namelist: `SOURCE_PARAMS` Particle Size Distribution Parameters parameters are used in (3.11), and the deposition model described in Section 3.5. The namelist contains arrays of length `nsources` to specifying the particle size distribution and source concentration for each independent source.

`gamma_magnitude(i)` **(U)** c_γ $[-]$ scale parameter for gamma distribution.

`gamma_shape(i)` **(U)** k_γ $[-]$ shape parameter for gamma distribution.

`gamma_scale(i)` **(U)** θ_γ [μm] theta scale parameter for gamma distribution.

`source(i)` **(U)** s [kg/m^3] Atmospheric concentration of salt particles.

`start_day(i)` **(I)** [dy] Number of day in year where the salt source begins to apply. Default is to apply all year. Default can be applied by entering 0 or not entering the item.

`end_day(i)` **(I)** [dy] Number of day in year where the salt source ceases to apply. Default is to apply all year. Default can be applied by entering 0 or not entering the item. Note that the date range can wrap around the end of the year so that `start_day` > `end_day`.

A.2.4 Database Parameters

The databases are a type of input used by the submodels that are independent of site. The databases are designed to store one, two, and three dimensional data. The databases are intended to store data that is derived from experiments or calculations that do not need to be recalculated during model execution. The databases were developed for a number of reasons including: the need to store properties that are not amenable to representation by analytical expressions; the need to store data in such a manner that it may be easily changed if new experimental or calculated data becomes available; and to allow for application of the code to different corrosive environments or materials systems.

The values in each database are represented by 1 to 3 dimensional data. The number of dimensions is supplied in the line following the informational header (usually containing a citation for the data source). For one-dimensional data, the number of entries Y is supplied on the next line, followed by Y rows containing two columns. The first column is the value of the independent variable, and the second is the value of the dependent variable.

For two-dimensional data, after the informational header, the next line contains the number of rows expected in the database Y, followed on the next line by the number of columns X. The following line holds the Y space-separated values for each row in the database. The next line holds the values of the X space-separated values of the columns in the database. The 2D database then requires the data in Y rows with X columns of values.

For three-dimensional data, after the informational header, the next line contains the number of rows expected in the database Y, followed on the next line by the number of columns X, followed on the next line by number of data sets Z. The following line holds the Y space-separated values for each row in the database. The next line holds the values of the X space-separated values of the columns in the database. The following line holds the Z space-separated values of each dataset. The 3D database requires $Z \times Y$ rows with X columns. The first Y rows contain the values at the first Z value, and so on, until all Z datasets are entered.

For four-dimensional data, after the informational header, the next line contains the number of rows expected in the database Y, followed on the next line by the number of columns X, followed on the next line by number of data sets Z, and followed on the next line by the number of groups W. The following line holds the Y space-separated values for each row in the database. The next line holds the values of the X space-separated values of the columns in the database. The following line holds the Z space-separated values of each dataset. The following line holds the W space-separated values of each dataset. The 4D database requires $Z \times Y$ rows with X columns. The first Y rows contain the values at the first Z value, and so on, until all Z datasets are entered for the first W value. The process is repeated for each W value.

Repeat the lowest values if no interpolation is intended, otherwise, interpolation will be assumed.

A summary of the required headers is given in Table A.1. The data may be provided in non-uniform increments. Linear interpolation will be employed to calculate data points between the given values. Replacing the databases does not require recompiling the code, only replacing the text file in the code's `Databases/` directory. The name of the database cannot be changed without recompiling the code as the filenames are set by the `hard_coded_file_names` module. The database's dimensionality must also remain unchanged.

Databases values are supplied to the calling routine after checking that the requested values are contained within the database.

A.3 Output from SCC Code

The output produced by the SCC codes varies depending the settings of the `debug` and `silent` simulation parameters located in the `SCC_Parameters.txt` input file. If `silent` is false, a limited amount of information is printed to the screen during model execution and other information is saved to files within the generated `Output/` directory of the current working directory. The screen will report the current time step during execution. Additional files output include annual summaries of maximum pit and crack depth, and salt deposition densities. If `debug` is true, the code prints a large amount of information to the screen for debugging purposes. Data reported includes detailed records of the convergence of root-finding algorithms and daily values of weather, pit, and maximum crack depth. It is recommended to use this option only for very short simulation time periods to aid in debugging due to the large amount of data reported.

A list of all possible output files are provided below. If a given file is only produced when `silent` is false (or `debug` is true) then it will be marked with a V indicating verbose output mode.

`epistemic_X_aleatory_Y.txt` This file echoes the current values of all global and site-specific parameters and is labeled with the iteration number of the epistemic and aleatory loops.

`results_summary.out` provides the total time taken, the job's name, date, and number of sites, epistemic, and aleatoric runs. The file also reports a time per realization for use in planning additional runs.

Table A.1: Description of header information required for 1, 2, 3 and 4 dimensional databases. With 3 comment lines, the number of lines before the actual data is given varies: 6 header lines are required for 1D data, 9 lines for 2D data, and 11 lines for 3D data, and 13 for 4D data.

Line#	1D	Description	2D	Description	3D	Description	4D	Description
1	N		N		N		N	Total Comment Lines
2	ln 1	Comment	ln 1	Comment	ln 1	Comment	Comment	Comment line #1
3	ln 2	Comment	ln 2	Comment	ln 2	...	ln 2	...
4	ln 3	Comment	ln 3	Comment	ln 3	Comment	ln 3	Comment line #N
5	1		2		3		4	Number of Dimensions
6	y		y		y		y	Number of Rows
7			x		x		x	Number of Columns
8			y-values	Values for Rows	z	Number of Sets	z	Number of Sets
9			x-values	Values for Columns	y-values	Values for Rows	w	Number of Groups
10				x-values	x-values	Values for Columns	y-values	Values for Rows
11				z-values	z-values	Values for Sets	x-values	Values for Columns
12							z-values	Values for Sets
13							w-values	Values for Groups

`weather.dat` Reports the daily weather generated for a given site including the maximum and minimum temperature [°C], RH [%], and dewpoint [°C].

`pits.dat` lists all pits that have *not* become cracks, including their initiation time and maximum depth [μm].

`cracks.dat` lists the depth [mm] and location of all active cracks that have *not* penetrated the canister wall.

`penetrating_cracks_summary.dat` will output data on all penetrating cracks for each aleatoric and epistemic evaluation. Time is reported in days, A null result will be returned if no penetration occurs.

`first_event_record.dat` A file reporting the first time of pit initiation, the first crack initiation, and the first penetration of the canister for each epistemic and aleatoric instance. These times are independent, meaning that they do not necessarily refer to the same pit. The data is unsorted. This file is intended for use in post-processing to extract statistics. Time is reported in days, where a -1 value means the event did not occur.

`first_twc.dat` Lists the location (coordinates, and weld), pit initiation time, crack initiation time, penetration time, and elapsed time for crack growth for the first crack that penetrates the wall in each aleatoric evaluation for all epistemic evalutions. Time is given in days, the weld number in which the crack is located, the normalized canister surface coordinates, and the crack's final depth is reported in mm.

`all_cracks_status.dat` Reports total number of cracks that formed in the canister. The file also reports the pit and crack initiation time [days], time to penetration [days], location [normalized coordinates], and weld number.

`interval_X_all_pits.dat` (V) Annually records the number of pits and the number that have not turned into cracks. For each surface site the location [normalized coordinates], weld number, pit initiation time [days], and maximum depth of each pit [μm] is written.

`interval_X_weld_Y.dat` (V) Annually records the location [normalized coordinates], salt deposition density [kg/m^3], pit initiation time [days], and maximum depth of the pit [μm] at each surface site.

`site_statistics_pit_init.dat` This file contains the CDF of the time to pit initiation resulting from completing the requested number of aleatory instances. This file is output for each epistemic instance of the model.

`site_statistics_crack_init.dat` This file contains the CDF of the time to crack initiation resulting from completing the requested number of aleatory instances. This file is output for each epistemic instance of the model.

`site_statistics_pit_init.dat` This file contains the CDF of the time until a crack first penetrates the wall after completing the requested number of aleatory instances. This file is output for each epistemic instance of the model.

A.4 Post-processing

```
    usage: post_process.py [-h] [-s SITEFILE] [-o OUTDIR] [-k PICKLE] [--pct PCT]
                           [--plotpct PLOTPCT] [-t TIMES] [-d SEARCHDIR]
                           [-f FIRST_TWC] [-p] [-po]

Post-processes one or more sites to generate CDF plots and instances on one or
more nodes on various computer systems

optional arguments:
  -h, --help            show this help message and exit
  -s SITEFILE, --sitefile SITEFILE
                        Location of file listing ISFSI sites
  -o OUTDIR, --outdir OUTDIR
                        Directory to hold CDF plots
  -k PICKLE, --pickle PICKLE
                        path to pickle file for ISFSI data
  --pct PCT             Value or tuple of percentile values to compite
                        [default: (1,2,5,95,98,99)]
  --plotpct PLOTPCT     tuple of max/min percentile values to display on plot
                        [default: (5.,95.)]
  -t TIMES, --times TIMES
                        tuple of years to report in summary file [default:
                        (25.,50.,75.,100.)]
  -d SEARCHDIR, --searchdir SEARCHDIR
```

```
                        path to start search
  -f FIRST_TWC, --first_twc FIRST_TWC
                        Name of file containing list of penetrating cracks
                        (default: first_twc.dat)
  -p, --plot            Generate plots? (HPCs may not have graphics
                        capabilities)[default: False]
  -po, --plotonly       Generate plots from pickel file without search for
                        datafiles? [default: False]
```

A.5 Errors & Warnings

An error means the code stops, while a warning does not stop code execution, but makes the user aware of unexpected behavior.
Errors:

```
========================================================================
                                ERROR
 <routine/table name>
------------------------------------------------------------------------
 <message>
  Parmeter Value:   <offending value>
  Limit Value   :   <limit value>
========================================================================
```

Warnings:

```
========================================================================
                               WARNING
 <routine/table name>
------------------------------------------------------------------------
 <message>
  Parmeter Value:   <offending value>
  Limit Value   :   <limit value>
========================================================================
```

Notes:

```
========================================================================
                                NOTE
 <routine_name>
------------------------------------------------------------------------
 <message>
========================================================================
```

Default value warning:

```
================================================================================
                    DEFAULT VALUE ASSIGNMENT WARNING
 <variable_name>
--------------------------------------------------------------------------------
 <message>
 Existing Value: <default value>
 New Value     : <current value>
================================================================================
```

A.5.1 Possible Warnings

Warnings will be suppressed if the parameter value `Silent == .true.`.

- `i_c_max value does not converge` test
- `i_c_max is set to zero, solution diverging` test
- `i_c_max convergence outside of tolerance`
- `r_anode convergence outside of tolerance`
- `r_anode greater than wall thickness, pit has penetrated wall`
- `Index exceeds Maximum Value of array, using linear extrapolation` test
- `Erp convergence outside of tolerance`
- `Value greater than Maximum value of array, using linear extrapolation` occurs when using the function
- `get_lower_index`. This function is only used to calculate offset time for initial decay heat.
- `Restarting Simulation from: (param: epistemic, limit: aleatoric)` The code's restart capability is engaged. This message displays the index of the next epistemic and aleatoric instance to continue the simulation until the originally requested number of evaluations is complete.

A.5.2 Possible Errors

- `i_c_max greater than maximum search limit`
- `i_c_max less than minimum search limit`
- `r_anode less than minimum search limit`
- `Erp greater than minimum search limit`
- `Erp greater than maximum search limit`
- `Index exceeds Maximum Value of array! (set extrapolate==True to bypass)`

- `Initial value of Decay Heat requested is greater than that available in table!`
- `Something's wrong, the requested decay heat is not found at Toffset` This is a check made to ensure that the calculated offset time actually corresponds to the desired initial decay heat in the `Decay_Heat_Horizontal.dat` or `Decay_Heat_Vertical.dat` databases.
- `Index exceeds Maximum Value of array! (set extrapolate==True to bypass)`
- `Value below that of minimum array value! (set extrapolate==True to bypass)`
- `Reynolds number smaller than minimum value in table, check value of wind_velocity weather parameter`
- `Reynolds number exceeded maximum value in table, check value of wind_velocity weather parameter`
- `File containing list of first TWC for each aleatory/epistemic run must exist!`

Appendix B Code Verification

Within the source code directory, the there exist a number of FORTRAN95 executables that are suffixed with `.tool` that should be executed to perform unit testing and validation. The available test cover each submodel and ancillary functions such as input and output ones.

- `chemistry.test`: tests the `chemistry` module that perform the calculation of the Anderko et al. [20] model for the E_{rp}value and compares it with the original paper. Output summary in `unit_test_files/ChemistryTest/ChemistryTestResults.out`
- `chen-kelly.test`: Tests the `chen_kelly` module's functions that calculate the maximum pit depth according to the model described in Refs. 49, 50. A summary of the output and comparison with figures and results from the original paper are found in `unit_test_files/CK/`
- `crack_growth.test`: Test the `crack_growth` module's functions that perform a test for the time of for crack growth under specific conditions. These results reproduce the values in the preliminary report (Ref. 1), with a summary of the output found in `unit_test_files/CrackGrowth/CGtest_results.txt`
- `deposition_rate.test`: This with a summary of the output found in `unit_test_files/DepositionRate/` also contains GNUPLOT scripts to plot the deposition velocity and compare it with the original paper it was implemented from, along with a script to plot the DD on the welds. Compare the results of `unit_test_files/DepositionRate/TestReport.dat` with those of `unit_test_files/DepositionRate/TestReport.ref.dat` to check the output of other ancillary functions provided by the module.
- `deterministic.test`: This test perform a series of deterministic calculations of the ASCC code at sites with fictitious fixed conditions that can be used to verify that the fully probabilistic model will function properly. Example sites are included in the `unit_test_files/DeterminsticTest/All_Sites_Data` folder and the results, for comparison, are provided in the `unit_test_files/DeterministicTest/Outputs_ref/` folder. Note that this test uses its own separate `Site.dat` file and `SCC_Parameters.nml` (input parameters file). With the separate source and input parameters files, this test is also intended to be used to test the code during development or quickly preform various “what-if” scenarios.
- `table_dump.test`: This tests will write the tables in the database to the folder `unit_test_files/plots/` where scripts exit to plot many of the tables. This test is used to

ensure that the code is reading the database tables as intended. This test is primarily intended to ensure that any new or revised databases are correctly read by the code by verifying that the tables are written with the intended coordinates assigned to the intended columns/rows.

- `random_seed.test`:
- `statistics.test`: This test is used to test the `statistics` module that calculates the CDF of the aleatoric runs. The test outputs a manufactured distribution and compares with the analytical solution that may be plotted with the included script. The distributions and plotting script are located in the `unit_test_files/StatisticsTest/` folder.
- `weather.test`: The test is intended to validate the functions in the `weather` module used to calculate RH, dewpoint, saturation pressure, and absolute humidity from the module's functions and database tables. A summary of the results are provided in `unit_test_files/WeatherTest/summary.txt`.

Appendix C Example SCC Output Files

C.1 Annual deposition record for a single weld

Output only if `silent = F`.

```
   Site ID          Radial    Longitudinal     DD [kg/m^2]   Pit Init Time  Max Depth [um]
         8            0.40            0.50       1.846E+00              -1           0.000
         9            0.40            0.58       1.875E+00              -1           0.000
        10            0.40            0.67       1.904E+00              -1           0.000
        11            0.40            0.75       1.999E+00              -1           0.000
        12            0.40            0.83       2.145E+00              -1           0.000
        13            0.40            0.92       2.311E+00            4482         232.860
        14            0.40            1.00       2.481E+00            1458         145.617
```

C.2 `first_twc.dat`

```
#Epis     Aleat     Pit Init.     Crack      Elapse       Weld     #        Longit.
    Radial Depth[mm]
    1         1          1458       1458       1459          1     2       1.000000
        0.400000   16.0000
```

C.3 `pits.dat`

```
 !   ID Weld#           Long    Radial Depth[um]
! Pits that are not cracks / total possi     2 /   24
      3     1       0.166667  0.500000        -1      0.00
      4     1       0.250000  0.500000        -1      0.00
      5     1       0.333333  0.500000        -1      0.00
      6     1       0.416667  0.500000        -1      0.00
      7     1       0.500000  0.500000        -1      0.00
      8     2       0.500000  0.400000        -1      0.00
      9     2       0.583333  0.400000        -1      0.00
     10     2       0.666667  0.400000        -1      0.00
     15     3       0.000000  0.000000        -1      0.00
     16     3       0.000000  0.125000        -1      0.00
     17     3       0.000000  0.250000      3571      3.21
     20     4       0.500000  0.000000        -1      0.00
     21     4       0.500000  0.125000        -1      0.00
     22     4       0.500000  0.250000     25924      3.95
     23     4       0.500000  0.375000        -1      0.00
     24     4       0.500000  0.500000        -1      0.00
```

C.4 `cracks.dat`

```
         IDPit I Init. Time Weld#   TWC T      Long    Radial Depth[mm]
   ! Number of cracks this realization:     8
```

```
     1      4482       4482     1       4483       0.000000  0.500000   16.0000
     2     18152      18152     1      18154       0.083333  0.500000   16.0000
    11     30573      30573     2      30574       0.750000  0.400000   16.0000
    12     14734      14734     2      14736       0.833333  0.400000   16.0000
    13      4482       4482     2       4483       0.916667  0.400000   16.0000
    14      1458       1458     2       1459       1.000000  0.400000   16.0000
    18      4055      23931     3      23932       0.000000  0.375000   16.0000
    19      4482      22709     3      22710       0.000000  0.500000   16.0000
```

C.5 `penetrating_cracks_summary.dat`

```
ID     Pit Init TInit. Time Weld#   TWC Time      Long    Radial Depth[mm]
             ! Number of thru-wall cracks this realization:     8
     1      4482       4482     1       4483       0.000000  0.500000   16.0000
     2     18152      18152     1      18154       0.083333  0.500000   16.0000
    11     30573      30573     2      30574       0.750000  0.400000   16.0000
    12     14734      14734     2      14736       0.833333  0.400000   16.0000
    13      4482       4482     2       4483       0.916667  0.400000   16.0000
    14      1458       1458     2       1459       1.000000  0.400000   16.0000
    18      4055      23931     3      23932       0.000000  0.375000   16.0000
    19      4482      22709     3      22710       0.000000  0.500000   16.0000
```

Appendix D Example SCC Input Files

D.1 Simulation Parameters

```
! SCC_Parameters File
!
! HOW TO READ THIS FILE:
!
! TYPE is an integer 0, 1, 2, or 3 which tells the type of parameter
!
! Each parameter has a given name denoted by NAME
!
! 0 = CONSTANT   expect a single numerical value
!               -
! 1 = UNIFORM    expect a T/F flag and two numerical values, in order of MIN MAX
! 2 = NORMAL     expect a T/F flag and three values in order of MEAN STANDARD_DEV TRUNCATION
! 3 = LOGNORMAL  same as NORMAL
!
! The T/F flag denotes if this is an epestemic or aleatoric parameter. T = Epestemic F = Aleatoric
!
! EXCEPTION: The parameters in the 'control' namelist are of type logical, character, or integer.
!            They do not follow this convention!
!
!!!!!!!!!!!!!!!!!!!!!!!!!!!!!!!!!!!!!!!!!!!!!!!!!!!!!!!!!!!!!!!!!!
!              The 'mode' namelist is optional.
!.................................................................
!  It will only be required if wanting to use the
!  'publication mode' for the case of the pipe
!!!!!!!!!!!!!!!!!!!!!!!!!!!!!!!!!!!!!!!!!!!!!!!!!!!!!!!!!!!!!!!!!!
&pub
publication = F,
/
!!!!!!!!!!!!!!!!!!!!!!!!!!!!!!!!!!!!!!!!!!!!!!!!!!!!!!!!!!!!!!!!!!
!    Simulation Control Parameters
!!!!!!!!!!!!!!!!!!!!!!!!!!!!!!!!!!!!!!!!!!!!!!!!!!!!!!!!!!!!!!!!!!
&control
! Silent | True if the program will not output anything (MUST BE LOGICAL)
silent = F,
! Debug  | True if the program will output degbugging information (in ./Debug) (MUST BE LOGICAL)
debug = F,
! Dakota mode | if True the program will produce output file for dakota based on second command line argument (MUST BE LOGICAL)
dakota_output = F,
! Dump Deposition Interval [days] | interval in days to dump (if silent == .false. or debug = .true.)
dump_interval = 365,
! Simulation Name | used in the summary file (MUST BE STRING)
simulation_name = "Probabilistic_Test",
! Epistemic Sample Size | Number of Epistemic Samples (MUST BE INTEGER)
epistemic_samples = 1,
! Aleatoric Sample Size | Number of Aleatoric Samples (MUST BE INTEGER)
```

```
aleatory_samples = 5,
! Longitudinal Weld Resolution | Descritization size for longitudinal welds
longitudinal_weld_resolution = 7,
! Radial Weld Resolution | Descritization size for radial welds
radial_weld_resolution = 5,
! Random Seed | Value used to seed the RNG (MUST BE INTEGER)
random_seed_value = 132462,
! # Bins for output statistics (10 day bins)
stat_bins = 3650,
!> \var number of first epistemic run (to number them consistently, even when launching multple instances of code (defaults to 1)), always start from scratch if <=0
epistemic_start=1,
/
!!!!!!!!!!!!!!!!!!!!!!!!!!!!!!!!!!!!!!!!!!!!!!!!!!!!!!!!!!!!!!!!!!
! simulation model parameters (all of the uncertain variable type)
!!!!!!!!!!!!!!!!!!!!!!!!!!!!!!!!!!!!!!!!!!!!!!!!!!!!!!!!!!!!!!!!!!
!-----------------------------------------------------------------
!Geometry and Canister parameters
!-----------------------------------------------------------------
&canister
! Initial Decay Heat | [kW]
initial_decay_heat%type_flag = 0,
initial_decay_heat%value = 24.0d0,
! Simulation time | [years]
simulation_time%type_flag = 0,
simulation_time%value = 100.0d0,
! Time step in days | Size of one time step | WARNING: must be 1 day (for now)
time_step%type_flag = 0,
time_step%value = 1.0d0,
! Canister Diameter | [m]
canister_diameter%type_flag = 0,
canister_diameter%value = 1.71d0,
! Canister Length | [m]
canister_length%type_flag = 0,
canister_length%value = 4.40d0,
! Canister Thickness | [m]
canister_thickness%type_flag = 0,
canister_thickness%value = 1.60d-2,
! weld_loc_1 | Weld #1 Radial Location [0 < theta < 0.5]
weld_1_location%type_flag = 1,
weld_1_location%epistemic_flag = T,
weld_1_location%minimum = 0.0d0,
weld_1_location%maximum = 0.5d0,
! weld_loc_2 | Weld #2 Radial Location [0 < theta < 0.5]
weld_2_location%type_flag = 1,
weld_2_location%epistemic_flag = T,
weld_2_location%minimum = 0.0d0,
weld_2_location%maximum = 0.5d0,
/
!-----------------------------------------------------------------
! Parameters for Crack Growth Model
!-----------------------------------------------------------------
&crack
! Random Hoop Weight |
random_hoop%type_flag = 1,
random_hoop%epistemic_flag = F,
random_hoop%minimum = 0.0d0,
random_hoop%maximum = 1.0d0,
! Random Axial Weight |
random_axial%type_flag = 1,
random_axial%epistemic_flag = F,
random_axial%minimum = 0.0d0,
random_axial%maximum = 1.0d0,
! Geometric Factor |
geom_factor%type_flag=1,
geom_factor%epistemic_flag = F,
geom_factor%minimum = 0.9d0,
geom_factor%maximum = 1.1d0,
```

```
! K_th | [MPa/sqrt(m)] Threshold stress intensity at T_th=80.0 and d=initial crack depth
K_th%type_flag = 1,
K_th%epistemic_flag = F,
K_th%minimum = 0.46d0,
K_th%maximum = 3.30d0,
! Crack Growth Rate @ 80C |  Rate for Crack Growth at 80 degrees Cp (may be log of value if constant)
crack_growth_rate_80C%type_flag = 3,
crack_growth_rate_80C%epistemic_flag = F,
crack_growth_rate_80C%mean = -20.13553
crack_growth_rate_80C%standard_dev = 1.325d0
crack_growth_rate_80C%truncation = 0.022d0,
! Beta_cg | Beta parameter for crack growth (may be log of value if constant)
beta%type_flag = 2,
beta%epistemic_flag = F,
beta%mean = 0.5d0,
beta%standard_dev = 0.2d0,
beta%truncation = 0.022d0,
! Alpha_cg | Alpha parameter for crack growth (may be log of value if constant)
alpha%type_flag = 3,
alpha%epistemic_flag = F,
alpha%mean = -25.921d0,
alpha%standard_dev = 1.570d0,
alpha%truncation = 0.022,
! Alpha_Beta_Correlation (must be constant)
alpha_beta_correlation%type_flag = 0,
alpha_beta_correlation%value = -0.47d0,
! T_ref_crack_growth [deg C]
T_ref_crack_growth%type_flag = 0,
T_ref_crack_growth%value = 15.5555d0,
/
! -----------------------------------------------------------------
!  Parameters for pit depth/corrosion model
! -----------------------------------------------------------------
&corrosion
! Threashold RH | Relative humidity below which no pits form [%]
threshold_rh%type_flag = 1,
threshold_rh%epistemic_flag = F,
threshold_rh%minimum = 15.0d0,
threshold_rh%maximum = 30.0d0,
! i_rp_ref | Reference Repassivation Current Density [A/m^2]
i_rp_ref%type_flag = 1,
i_rp_ref%epistemic_flag = F,
i_rp_ref%minimum = 0.068d0,
i_rp_ref%maximum = 1.540d0,
! E_rp_ref | Potential at the pit (anode) [V_SCE]
E_rp_ref%type_flag = 0,
E_rp_ref%value = -0.4d0,
! Tafel | Tafel Slope per decade of current [V_SCE/decade]
tafel%type_flag = 1,
tafel%epistemic_flag = F,
tafel%minimum = -0.169d0,
tafel%maximum = -0.138d0,
! E_L | Corrosion Potential at cathode edge [V_SCE]
E_L%type_flag = 0,
E_L%value = -0.2d0,
! E_rp_min | Potential at the pit (anode) [V_SCE]
E_rp_min%type_flag = 0,
E_rp_min%value = -2.0d0,
! Galvele | Galvele hemispherical pit stability product [A/m]
galvele%type_flag = 1,
galvele%epistemic_flag = F,
galvele%minimum = 1.0d0,
galvele%maximum = 3.0d0,
! rho_particle | Density of airbourne salt particle [kg/m^3],
particle_density%type_flag = 0,
particle_density%value = 2165.0d0,
/
```

```
!!!!!!!!!!!!!!!!!!!!!!!!!!!!!!!!!!!!!!!!!!!!!!!!!!
! File Names to be used for this simulation
!!!!!!!!!!!!!!!!!!!!!!!!!!!!!!!!!!!!!!!!!!!!!!!!!!
!------------------------------------------------------------------
!           INPUT FILE NAMES
!------------------------------------------------------------------
&input
!> \brief Location of the file with the site names
site_file_name="Sites.dat",
!> \brief Where the sites data is located (not a parameter so it can be overwrtiten by tests )
sites_folder="All_Sites_Data",
/
!------------------------------------------------------------------
!                        DATABASE FILE NAMES
!..................................................................
!    If a database file name is not included, the file will not
!    be read!
!------------------------------------------------------------------
&databases
!> \brief Location of the axial stress table (read into ‘axial_stress_table‘)
axial_file_name="Databases/axial_stress.dat",
!> \brief Location of the hoop stress table (read into ‘hoop_stress_table‘)
hoop_file_name="Databases/hoop_stress.dat",
!> \brief Location of the relative humidity table (read into ‘steam_table‘)
steam_file_name="Databases/Steam.dat",
!> \brief Location of the inverse density as a funciton of pressure table (read into ‘psat_temp_table‘)
press_file_name="Databases/PsatvsT.dat",
!> \brief Location of the saturated vapor pressure as a funciton of temperature table (read into ‘air_dens_table‘)
volume_file_name="Databases/VolvsPsat.dat",
!> \brief Location of the temp data for horizontal canisters (read into ‘horizontal_temp_table‘)
horizontal_file_name="Databases/Horizontal_Temp.dat",
!> \brief Location of the temp data for vertical canisters (read into ‘vertical_temp_table‘)
vertical_file_name="Databases/Vertical_Temp.dat",
!> \brief Location of the decay heat data for horizontal canisters (read into ‘decay_heat_vertical‘)
decay_heat_horizontal_file_name="Databases/Decay_Heat_Horizontal.dat",
!> \brief Location of the decay heat data for vertical canisters (read into ‘decay_heat_vertical‘)
decay_heat_vertical_file_name="Databases/Decay_Heat_Vertical.dat",
!> \brief Location of the C_f data for horizontal canisters (read into ‘horizontal_cf_table‘)
!horizontal_Cf_file_name="Databases/Cf_horizontal.dat",
!> \brief If present, the u* file will be used for horizontal canisters
horizontal_ustar_file_name="Databases/Horizontal_Ustar.dat",
!> \brief If present, the u* file will be used for vertical canisters, otherwise, flat plate friction is assumed
! vertical_ustar_file_name="Databases/vertical_ustar.dat",
!> \brief Location of the cathodic conductivity density table (read into ‘cathodic_conductivity_table‘)
cond_file_name="Databases/Cathodic_conductivity.dat",
!> \brief Location of the Brine Thickness table (read into ‘brine_table‘)
brine_thickness_file_name="Databases/Brine_Thickness.dat",
!> \brief Location of the dry Air Density table (read into ‘air_dens_table‘)
air_dens_file_name="Databases/AirDensvsT.dat",
!> \brief Location of the Brine pH table (read into ‘brine_ph_table‘)
brine_pH_file_name="Databases/Brine_pH.dat",
!> \brief Location of the Brine Cl- concentration table (read into ‘cl_concentration_table‘)
Cl_concentration_file_name="Databases/Brine_Cl_concentration.dat",
/
!------------------------------------------------------------------
!           OUTPUT FILE NAMES
!------------------------------------------------------------------
&output
!> \var Used to catalog errors
```

```
error_report_file_name="Outputs/ERROR_REPORT.txt",
!> \var Outputs directory (not a paramter so it can be reset by tests)
output_directory="Outputs",
!!
!! output_directory determines the prefix for the following files:
!!
!> \var Results of the simulation
results_file_name="results_summary.out",
!> \var Summary Statistics
site_statistics_file_name="site_statistics.dat",
!> \var Output file for the pit data
pits_out_file_name="pits.dat",
!> \var Output file for the crack data
cracks_out_file_name="cracks.dat",
!> \var Output file for the crack summary data
cracks_summary_out_file_name="penetrating_crack_summary.dat",
!> \var Output file for the weather data
weather_out_file_name="weather.dat",
!> \var First event record file for each epistemic loop, determines separately, the first
    pit initiation, crack initiation, and penetration times.
time_record_file_name="first_event_record.dat",
!> \var Data for first pit/crack to penetrate wall (not necessarily the first pit or crack
    to initiate)
twc_summary_file_name="first_twc.dat",
/
!!!!!!!!!!!!!!!!!!!!!!!!!!!!!!!!!!!!!!!!!!!!!!!!!!
!            END OF SCC PARAMETERS FILE
!!!!!!!!!!!!!!!!!!!!!!!!!!!!!!!!!!!!!!!!!!!!!!!!!!
```

APPENDIX E

FCT DOCUMENT COVER SHEET[1]

Name/Title of Deliverable/Milestone/Revision No. Status Report: Uncertainty Quantification of Environmentally Assisted Stress Corrosion Cracking in Used Fuel Canisters / M3SF-19SN010201047

Work Package Title and Number SCC and Dry Storage Investigations - SNL – SF-19SN01020104

Work Package WBS Number 1.08.01.02.01

Responsible Work Package Manager Charles R. Bryan / Charles R Bryan 3/22/2019
(Name/Signature) Date Submitted

Quality Rigor Level for Deliverable/Milestone[2]	☒ QRL-3	☐ QRL-2	☐ QRL-1 Nuclear Data	☐ Lab/Participant QA Program (no additional FCT QA requirements)

This deliverable was prepared in accordance with Sandia National Laboratories
(Participant/National Laboratory Name)

QA program which meets the requirements of

☒ DOE Order 414.1 ☐ NQA-1-2000 ☒ Other: FCT QAPD

This Deliverable was subjected to:

☒ Technical Review	☐ Peer Review
Technical Review (TR)	**Peer Review (PR)**
Review Documentation Provided	**Review Documentation Provided**
☐ Signed TR Report or,	☐ Signed PR Report or,
☐ Signed TR Concurrence Sheet or,	☐ Signed PR Concurrence Sheet or,
☒ Signature of TR Reviewer(s) below	☐ Signature of PR Reviewer(s) below

Name and Signature of Reviewers

John Kessler

NOTE 1: *Appendix E should be filled out and submitted with the deliverable. Or, if the PICS:NE system permits, completely enter all applicable information in the PICS:NE Deliverable Form. The requirement is to ensure that all applicable information is entered either in the PICS:NE system or by using the FCT Document Cover Sheet.*

NOTE 2: *In some cases there may be a milestone where an item is being fabricated, maintenance is being performed on a facility, or a document is being issued through a formal document control process where it specifically calls out a formal review of the document. In these cases, documentation (e.g., inspection report, maintenance request, work planning package documentation or the documented review of the issued document through the document control process) of the completion of the activity, along with the Document Cover Sheet, is sufficient to demonstrate achieving the milestone. If QRL 1, 2, or 3 is not assigned, then the Lab / Participant QA Program (no additional FCT QA requirements) box must be checked, and the work is understood to be performed and any deliverable developed in conformance with the respective National Laboratory / Participant, DOE or NNSA-approved QA Program.*